To the Graduate Council:

I am submitting herewith a dissertation written by Young Ryong Choi entitled "Studies of the Mechanism of Electron Beam Induced Deposition (EBID)." I have examined the final electronic copy of this dissertation for form and content and recommended that it be accepted in partial fulfillment of the requirements for the degree of Doctor of Philosophy, with a major in Materials Science and Engineering.

David C Joy
Major Professor

We have read this dissertation
and recommend its acceptance:

Philip D. Rack

Joseph E. Spruiell

Anthony J. Pedraza

Accepted for the council:

Linda Painter
Interim Dean of Graduate Studies

(Original signatures are on file with official student record)

Studies of the Mechanism of Electron Beam Induced Deposition (EBID)

A Dissertation Presented for the Doctor of Philosophy Degree

The University of Tennessee, Knoxville

Young Ryong Choi

December, 2006

DEDICATION

To my parents Moon Seok Choe and Dong Suk Ryu who have supported me all the way since the beginning of my life and to my wife Yeong Ju Cho, two sons Rigeon and Quegeon for their support and love.

ACKNOWLEDGEMENTS

I particularly wish to pay my deepest respect to my academic professor, Dr. David C. Joy. He was not only a great scientist filled with great ideas and enthusiasm but also a great man filled with beautiful and positive soul. He inspired my research interest in the world of electron microscopy, always encourages his students as much as he can and always showed us positive attitude.

I really thank to Dr. Philip D. Rack for his positive encouraging advice with enthusiasm and his group members, J. D. Fowlkes, S. J. Randolph, Seung-Ik Jun, Yupeng Deng, and Daryl A. Smith for their support in research. It was my pleasure to study with my group members, Jihoon Kim, Wei Li, Yinghong Lin, Satyavani Bari, Sachin Deo, Kiran Jaladhi, Medhi Bolorizadeh and wonderful secretary Jennifer Trollinger. I want to thank my committee members Professor Joseph E. Spruiell and Professor Anthony J. Pedraza for their instructions for my benefit.

ABSTRACT

The controlled deposition of metals resulting from the passage of an ion beam through an atmosphere of a suitable precursor gas is a well-established procedure for micro scale materials manipulation. While the ion beam technique is rapid and reliable it has the disadvantage that the beam itself can ablate and contaminate the target with Gallium or other materials, and the fact that ion optics are less widely accessible than electron optical columns. We have therefore been investigating the theory and practice of depositing metal using an electron beam and variety of precursor gases. The aim of this work is to develop techniques that can be applied to the repair of the optical, ultra-violet (UV) and extreme ultra-violet (EUV) masks used in high performance photo-lithography. This thesis is concentrated on electron beam induced deposition (EBID) performed in a commercial Scanning Electron Microscope (SEM). For EBID experiments, we have developed a gas injection system for the specimen chamber of a standard SEM which is able to control the pressure and the delivery flow rate of gas for experiment. Studies of factors that control the properties of the deposition - such as the electron-gas interactions, the effects of gas pressure, and the temperature of the substrate – have been made and

experiments to determine the fundamental mechanisms of EBID - such as which types of electrons are responsible for the initial interaction event with the precursor – have been carried out and analyzed and systematically studied to determine the optimum conditions for the practical application of the EBID approach. Finally the practical applications of the EBID have been applied to repair of masks.

TABLE OF CONTENTS

CHAPTER 1 INTRODUCTION **1**

CHAPTER 2 LITERATURE REVIEW **5**

2.1 Historical Background of Electron Beam Induced Deposition (EBID) **5**
2.2 Comparison of Focused Ion Beam (FIB) and EBID **6**
2.3 Related Factors Affecting EBID Process **7**
2.3.1 Depositing Materials 7
2.3.2 Electron-Gas and Electron-Solid Interaction 8
2.3.3 Temperature Dependence of the EBID 13
2.3.4 Pressure Dependence of the EBID 14
2.4 The EBID Spatial Resolution **14**

CHAPTER 3 THEORETICAL BACKGROUND **16**

3.1 Particle Beams **16**
3.2 Basic Mechanism of EBID **21**
3.3 Interaction Between Electrons and Solid Matter **24**
3.4 Growth Rate of EBID **28**
3.5 Spatial Resolution of the Deposit **29**
3.5.1 The Role of Secondary Electron (SE) 29
3.6 Influence of Beam Energy **33**
3.7 Temperature Effect on EBID **36**
3.8 Thickness Determining Factors **37**

CHAPTER 4 EXPERIMENTAL EQUIPMENT AND PROCEDURES **39**

4.1 Experimental Procedures for EBID **39**
4.1.1 Scanning Electron Microscope (SEM) 39
4.1.2 Gas Injection System 42
4.2 Precursors Gases **42**
4.2.1. Tungsten hexa-carbonyl: $W(CO)_6$ 44

4.2.2 Tungsten hexa-fluoride: WF_6 45
4.3 Experimental Procedure **45**
4.3.1 Deposition with Tungsten hexa-carbonyl ($W(CO)_6$) 45
4.3.2 Deposition with Tungsten hexafluoride (WF_6) 46
4.4 Experiments for Pressure Effect **47**
4.5 Temperature Dependence **51**
4.6 Effect of Scan Mode of SEM **51**

CHAPTER 5 RESULTS AND DISCUSSION **55**

5.1 Characterization of $W(CO)_6$ Deposits **55**
5.2 Calibrating Layer Thickness **56**
5.3 Growth Rate of Deposits **62**
5.4 Role of Secondary Electrons (SE) **72**
5.5 Biasing Effect on Box mode Deposition and Etching **76**
5.6 Pressure Effect **81**
5.7 Effect of Scan Speed of SEM **99**

CHAPTER 6 PRACTICAL APPLICATIONS **103**

6.1 Mask Repair **103**
6.1.1 A Brief Explanation of Mask Repair 103
6.2 Repair of Binary and EUV ML Mask **107**
6.2.1 Repair of Binary Mask Substrate 115

CHAPTER 7 CONCLUSION **120**

REFRENCES **123**

VITA **131**

LIST OF TABLES

2.1	Physical properties of EBID/IBID precursors (S-solid, L-liquid, G-gas)	**9**
2.2	The chemical formulae and corresponding names for EBID/IBID precursor	**11**
3.1	Particle wavelengths at various particle energies E_0 (eV).	**17**

LIST OF FIGURES

3.1	Numerical aperture angle of inverted cone.	18
3.2	Illustration of EBID process.	23
3.3	Signals generated from electron and solid interaction.	26
3.4	The typical EBID interaction electron-target-precursor interaction scheme.	27
3.5	The role of secondary electrons (SE) at different growth moments: (a) in the beginning, (b) after a tip structure has grown.	31
3.6	A typical curve showing the evolution of the cone diameter.	32
3.7	Direct visualization of the electron volume in polymethylemethacrylate.	35
4.1	Fabrication and etching facilities. (a) Hitachi S 4300/N SE (b) Hitachi S-3500N scanning electron microscope (SEM) for the EBID experiment attached with SE, BSE, and X-ray detectors.	40
4.2	Chamber environment of S-4300 SE/N measured by Residual Gas Analyzer (RGA).	41
4.3	Gas injection system. (a) for 3-dimensional manipulation (b) Gas injection system attached to the Hitachi S-4300 SE/N.	43
4.4	Deposition with WF_6. (a) Tilted image of deposition with WF_6 for 10 sec to 60 sec. (Beam energy: 1 Kev, Current: 20 pA, Magification: 45 K) (b) Very fine line of tungsten deposited by high speed scan.	48
4.5	The system set up for deposition with different pressure with TEOS and WF_6 precursor gas.	50
4.6	Peltier cold stage connected to the sample holder of SEM for control of temperature of the substrate.	52
4.7	Deposition of tungsten lines with different scan modes (TV2, TV1, SLOW2, SLOW1).	54
5.1	Tungsten deposition with increasing time: (a) 2.5μm x 2.5μm tungsten box deposition using $W(CO)_6$ precursor. (b) EDS spectra of deposits of Fig. 4.4 (a).	57
5.2	Measurement of tungsten with $W(CO)_6$ precursor: (a) scanned area for the Auger analysis, (b) Auger spectra from the PHI 680.	58
5.3	Calculation of thickness by X-ray peak ratio: (a) X-ray analysis after $W(CO)_6$ deposition with beam energy of 10 KeV for 5 minutes of germanium, (b) Ge/W peak ratio versus tungsten thickness from	60

simulation.
5.4 Deposition with WF_6 : (a) with spot mode for 10-60 sec.(beam energy 1 keV, specimen current 3pA), (b) with line mode for 30-120 sec. with 30 sec. increment (beam energy 1 keV, specimen current 3pA), (c) comparison of growth rate with spot and line mode. 63
5.5 Image of tungsten clusters. (a) High angle annular dark field image of tungsten clusters using Hitachi HD2000 at 200KeV. (b) Inverted contrast bright field STEM image of tungsten line at 200KeV. 66
5.6 High angle annular dark field image of a deposited tungsten line on carbon substrate, showing the line profile. 68
5.7 Growth at fixed energy (10Kev) and current (2nA) vs time. 70
5.8 Thickness vs deposition time ($W(CO)_6$, at 10Pa with 2nA). 71
5.9 Impact ionization data for hydrocarbons. 74
5.10 Biased by 25 volts positive and negative grew for 2min with 1 KeV. 75
5.11 Simulation of trajectory of SE and BSE under positive 180 volt of potential applied on 1x1cm^2 box in SEM with two different emission energies. 77
5.12 Biased by three different biases in box mode. (a) 4x4μm^2 box etching with -180 volt, no bias, and +180 volts with 5KeV for 1minute. (b) Depth profile measured with AFM of upper three. (c) AFM of bottom three. 79
5.13 Biased by three different biases in box mode. (a) 4x4μm^2 box deposition with -180 volt, no bias, and +180 volts with 5KeV for 30minutes. (b) Depth profile measured with AFM of upper three. 80
5.14 Growth with TEOS Precursor gas with the pressure of
(a) $1x10^{-6}$Pa (b) $3x10^{-6}$ Pa (c) $8x10^{-6}$Pa 82
5.15 Growth with WF_6 precursor gas with the pressure of
(a) $1x10^{-6}$Pa (b) $3x10^{-6}$ Pa (c) $8x10^{-6}$Pa. 83
5.16 Heights of nano pillar deposits of (a) SiOx and (b) W 84
5.17 Width of nano pillar deposits of (a) SiOx and (b) W 85
5.18 Growth rates of nano pillar deposits : (a) SiOx and (b) W by calculation 86
5.19 Monte-Carlo simulation of interaction volume with the beam energy of 20KeV for bulk substrate. (a) SiO_2, (b) Tungsten. 88
5.20 Monte-Carlo Simulations of the effective interaction volumes in the pillars with 20 keV beam energy: (a). 400nm in diameter and 350nm in 92

diameter for SiO_2 fibers. (b). 250nm, 170nm, and 130nm in diameter for tungsten fiber.

5.21 Measurement of the top curvature height of the pillar for each pressure with (a) $1x10^{-3}$Pa (b) $3.6x10^{-3}$Pa (c) $8x10^{-3}$Pa for tungsten and (d) $3.6x10^{-3}$Pa (e) $8x10^{-3}$Pa for SiOx EBID deposits. 95

5.22 Three-dimensional simulations of the electron beam induced deposition: (a) TEOS precursor gas with the pressure of 40Pa with electron does of 300K, 600K, and 900K. (b) WF_6 precursor gas with the pressure of 120Pa. with electron dose of 300K, 600K, and 900K. (c) Simulated growth rate of SiOx and tungsten EBID process with electron dose for simulation is up to 900K with the pressure of (40 Pa). 97

5.23 Different scan modes deposition: (a) line deposition of tungsten with four different scan modes (TV2, TV1, SLOW2, SLOW1). (b) line width variation due to the scan modes of the SEM. 100

6.1 Brief schematic explanation of mask and pattern develop. 104

6.2 Clear defect repair of Cr/Qtz binary mask using EBID. 109

6.3 Clear defect repair of TaBN//Mo-Si ML/Si EUV mask. 110

6.4 Etching of TaN absorber layer with (beam energy 2 KeV, beam current 0.02 nA in 0.2 Pa pressure) (a) different times (b) 5 seconds (c) 20 seconds and (d) box mode with 2minutes. 113

6.5 Simulated interaction volume with 2KeV beam energy in TaN absorber layer on EUV mask blank by “Win Casino”. 114

6.6 Etching with 0.2 Pa ambient pressure using XeF_2 with 2KeV beam energy, 53 pA of beam current for 4 minutes of box mode. 116

6.7 Deposition of tungsten on quartz. (a) with variation of pressure (b) with variation of temperature. 118

CHAPTER 1

INTRODUCTION

The requirement of the semiconductor industry for fabrication on ever smaller scales has now been extended to other fields such as biology, chemistry, and optics. For higher device density in circuits, for better resolution in optics, and for the production of Micro-Electro Mechanical Systems (MEMS), electron microscopy is the most widely used tool for fabrication and imaging, and the Scanning Electron Microscope (SEM) is the most common and useful instrument for these purposes. While there are already many methods for two-dimensional fabrication using photon or ion beam sources, the special benefits of the technique developed here are that it can be employed in any SEM, sample preparation is straightforward, and the normal imaging and analysis modes of the microscope can be used during and after deposition.

The controlled erosion or deposition of a specimen resulting from the passage of an ion beam through an atmosphere of a suitable precursor gas is a well-established procedure for micro-scale materials manipulation. While the ion technique is rapid and reliable it has the disadvantage that the beam itself can ablate, stain, and contaminate the target

with Gallium or other ions, and ion optics are less widely accessible and less well developed than electron optics. We have therefore been investigating the theory and practice of depositing metal using only an electron beam and variety of gases. The aim of this work has been to develop techniques that can be applied to the editing, correction, and repair of optical, ultra-violet (UV) and extreme ultra-violet (EUV) masks used in advanced photolithography.

As predicted by Gorden Moore [1], the packing density of semiconductor devices continues to increase. To achieve ever higher packing density, the features on the photo-mask (reticle) used to pattern the wafer have also to become smaller and their placement has to be more accurate. Additionally, because a current mask may contain upwards of a billion separate features the possibility of an error in the size, shape or position of some fraction of this number is high. Masks are also fragile and sensitive to handling, mechanical, and radiation induced, damage since these will result in printable defects. Because a set of masks for a Central Processing Unit (CPU) chip such as Pentium can cost upward of a million dollars there is a strong economic incentive to repair, rather than to replace, a damaged reticle. The increase use of optical proximity corrections (OPC) [2] [3] to enhance the resolution of photo-lithography also leads to a need for a method

which can ‘edit’ (i.e remove or modify an existing feature and replace it with new one) a mask without causing printable damage. While mask design, writing, and inspection have all become more complex, no task has increased in complexity more than mask repair.

Defects in photo-masks are classified as being either “clear” – indicating that an area transmits the illumination instead of blocking it – or “opaque” – when an area stops the incident radiation instead of passing it. Both are equally likely, both are significant sources of printable and possibly fatal defects and both must be connected.

Earlier, when mask line widths were on the order of a few micrometers, laser repair tools to cut and clean traces were the workhorses of the industry. These were fast and fairly easy to use, but were limited in spatial resolution and beam spot size, and they had only a limited capability for depositing material onto the mask. For binary (i.e. chrome on quartz) masks, thermal removal of the chrome also tended to damage the quartz substrate requiring another repair step since even the small amounts of damage that were produced would print as a defect on the wafer. Focused ion beam (FIB) tools [4] have also been used to repair clear defects by depositing an opaque carbon patch where the chrome is missing, but FIB tools have only limited ability to repair opaque defects because the

procedure creates unacceptable damage to the quartz and implants gallium ions into the substrate, so staining the mask and generating a printable defect. Some newer FIB mask repair tools therefore use gas assisted etching (GAE) for chrome [5] to make high-quality repairs of opaque defects. In these systems, a precursor gas is introduced which enhances the chrome etch rate, so minimizing the quartz damage and gallium implantation allowing the mask maker to repair clear defects with carbon deposition and opaque defects with chrome GAE. [5]

As lithographic wavelengths are reduced from 248 nm to 198 nm, however, defect repairs become much more difficult. Lithography at and below 193 nm presents a new series of challenges with the need to reduce quartz damage and improve the edge accuracy for mask repair. For a better solution to the need to repair small defects without causing mask damage, I have used an electron source since it has the advantage of a low beam diameter for small area repair. In addition we can easily find defects by using the imaging modes of the SEM and then fix them directly through electron beam induced deposition (EBID) and etching.

CHAPTER 2

LITERATURE REVIEW

Studies reporting the use of electron beam for the controlled deposition and erosion of materials have been published for a decade or more. The purpose of this chapter is to review this literature and to summarize the basic information that it contains.

2.1 Historical Background of Electron Beam Induced Deposition (EBID)

There are many ways to deposit materials across a large area of a target or substrate, but for localized deposition it is necessary to use a tool that can be controlled on a very small scale. If the target area falls within the range from the sub-micron to the nano-meter scale then a good candidate for this application is an energetic beam of particles such as photons, ions, or electrons. Such beams have been used for deposition or etching for a long time, and in many areas of both industrial application and academic research and each has its own particular benefits and drawbacks which in turn determine their uses and limitations.

Electron Beam Induced Deposition (EBID) is not new. From the earliest days of electron microscopy it was found that the incident beam produced dark stains on the sample. Investigations showed that the dark image of this contamination square was due to the hydrocarbons in the chamber of the electron microscope which came from the back streaming of the vacuum pump oil [6] [7]. The formation of carbonaceous films on surfaces under electron bombardment in vacuum has been extensively studied [8] [6] [9] [10]. Broers et al. [11] was among the first to deliberately exploit this effect so as to fabricate nanometer scale structures in a scanning transmission electron microscope (STEM) [12].

2.2 Comparison of Focused Ion Beam (FIB) and EBID

Focused ion beams and electron beams can both be used for high resolution deposition processes. The basic principle of this method is the introduction of a vapor containing some suitable chemical form of the desired material to be deposited into the sample chamber. Molecules from the gas adsorbed at the surface of the specimen are dissociated by the electrons, or ions, impinging at the scanned area on the sample surface. The desired material is deposited while the other components are pumped away. This

deposition method can be used for device modification, the repair of photolithography masks, and the fabrication of field emitter tips [13].

For EBID Kretz *et al*. [14] suggested that the electron beam directly damages the adsorbed molecules which decompose as a consequence, and Kunz and Mayer [15] proposed that secondary electrons were the component which initiated the decomposition. For focused ion beams, Melngailis et al. [16] suggested two different models, a thermal spike model and a collision cascade model.

2.3 Related Factors Affecting EBID Process

Many factors affect EBID, including the choice of precursor gas, electron-gas and electron-solid interactions, beam parameters, such as energy and current, target temperature, and chamber parameters, such as pressure. In the next section the literature on each of these topics is summarized.

2.3.1 Depositing Materials

There is a need to deposit many kinds of materials depending on their function and purpose. Therefore many different kinds of precursor gases have been investigated. Table

2.1 and 2.2 tabulates some of the gases that have been studied and the materials that they cause to be deposited.

2.3.2 Electron-Gas and Electron-Solid Interaction

The spatial resolution of EBID is mainly dependent on the primary electron beam diameter and the distribution of the secondary electrons. However, there is abundant experimental evidence that the width of dots and lines fabricated by EBID with high energy electrons, considerably exceeds the diameter of the electron beam writing tool [17] [18] [19] [20]. Many authors consider that this lateral broadening is mainly caused by the low energy secondary electrons (SE), emitted from the substrate as a result of the primary electron beam irradiation . This assumption is based on the fact that the electron-impact molecular dissociation, assumed to be the main process in EBID, has an interaction cross-section which is peaked at the low kinetic energies [21] [22] which are characteristics of secondary electrons.

Information about the behavior of the secondary emission can be obtained by studying the electron scattering in the target. The problem of electron-solid interaction should be ideally solved experimentally, by measuring the relevant physical quantities resulting

Table 2.1: Physical properties of EBID/IBID precursors. (S-solid, L-liquid, G-gas) [23]

Depo Mat.	Precursor Molecular formula	Vap. Press at RT	S	L	G	Reference
Au	$Me_2Au(hfac)$ $C_7H_7F_6O_2Au$	700 mtorr		x		[24] [25] [26] [27] [28]
	$Me_2Au(acac)$	8 mtorr				
	$Me_2Au(tfac)$	40 mtorr				[29] [30] [31] [32] [33]
	$AuClPF_3$		x			[34]
Al	$Al(CH3)_3$			x		[35] [36]
Cu	$Cu(hfac)_2$		x			[13]
	$(C_5HF_6O_2)Cu(CH_3)$ $3SiCH=CH_2)$	420 mtorr	x			[37]
Cr	$Cr(CO)_6$	10 mtorr		x		[38]
Fe	$Fe(CO)_5$	3 mtorr		x		[26] [39]
	$Fe(C_5H_5)_2$					[40]
Mo	$Mo(CO)_6$	78 mtorr	x			[41]
Os	$Os_3(CO)_{12}$					[42]
Ni	$Ni(CO)_4$	10 mtorr			x	[43] [44]

Table 2.1: Continued.
[23]

Depo Mat.	Precursor Molecular formula	Vap. Press at RT	S	L	G	References
Pd	$Pd(OOCCH_3)_2$					[45]
	$Pd(C_3H_5)(C_5H_5)$					[45]
Re	$Re_2(CO)_{10}$					[46]
Ru	$Ru_3(CO)_{12}$					[42]
Rh	$Rh(PF_3)_2Cl_2$	55 mtorr	x			[47] [48]
Pt	$(CH_3)_3(C_5H_5)Pt$ or $C_5H_5PtMe_3$ or $CpPtMe_3$	54 mtorr	x			[49] [50] [29] [30] [51] [52]
	$(CH_3C_5H_4)(CH_3)Pt$	54 mtorr	x			[53] [54] [55]
SiO_x	$Si(OCH_3)_4$	420 mtorr		x		[56]
SiO_2	$Si(C_2H_5O)_4$	1.5 mtorr				[57]
Si	SiH_2C_{l2}					[58] [59]
W	$W(CO)_6$	17 mtorr	x			[31] [60] [61] [62] [63] [64] [17] [65]
	WF_6				x	[58] [66]
C	C_8H_8or $C_6H_5CH=CH_2$	10-25 torr				[67] [68]
	$C_{12}H_{26}$ to $C_{18}H_{38}$			x		[69]
	$C_{16}H_{10}$					[70]

Table 2.2: The chemical formulae and corresponding names for EBID/IBID precursors.[23]

Depo Mat.	**Precursor Chemical formula**	**Name**
Au	$(CH_3)_2Au(hfac)$	dimethyl gold hexafluoro acetylacetonate
	or $C_7H_7F_6O_2Au$	
	$Me_2Au(acac)$	dimethyl gold acetylacetonate
	$Me_2Au(tfac)$	dimethyl gold trifluoroacetylacetonate
	$AuClPF_3$	gold trifluorophosphine chloride complex
Al	$Al(CH_3)_3$	trimethyl aluminium
	$Al(C_4H_9)_3$	tri-isobutyl aluminium
Cu	$Cu(hfac)_2$	copper hexafluoroacetylacetonate
	$(C_5HF_6O_2)Cu(CH_3)$	hexafluoroacetylacetonate copper vinyl-trimthyl-silane
	$3SiCH=(CH_2)$	or HFA-Cu-VTMS
Cr	$Cr(CO)_6$	chromium hexacarbonyl
Fe	$Fe(CO)_5$	iron pentacarbonyl
	$Fe(C_5H_5)_2$	ferrocene
Mo	$Mo(CO)_6$	molybdenum hexacarbonyl
Os	$Os_3(CO)_{12}$	osmium carbonyl

Table 2.2: continued.

Depo. Mat.	**Precursor chemical formula**	**Name**
Pd	$Pd(OOCCH_3)_2$ $Pd(C_3H_5)(C_5H_5)$	Pd-Ac palladium acetate palladium allylcyclopentadienyl
Re	$Re_2(CO)_{10}$	rhenium carbonyl
Ru	$Ru_3(CO)_{12}$	ruthenium carbonyl
Rh	$Rh(PF_3)_2Cl_2$	
Pt	$(CH_3)_3(C_5H_5)Pt$ or $C_5H_5PtMe_3$ or $CpPtMe_3$	cyclopentadienyl-trimethyl-platinum
	$(CH_3C_5H_4)(CH_3)Pt$	methylcyclopentadienyl-trimethyl-platinum
SiO_x	$Si(OCH_3)_4$	tetramethoxysilane (TMS)
SiO_2	$Si(C_2H_5O)_4$	tetraethoxysilane (TEOS)
Si	SiH_2C_{l2}	dichlorosilane
W	$W(CO)_6$ WF_6	tungsten hexacarbonyl tungsten hexafluoride
C	C_8H_8 or $_6H_5CH=CH_2$ $C_5H_8O_2$ $C_{16}H_{34}$ $C_{12}H_{26}$ to $C_{18}H_{38}$ $C_{16}H_{10}$	styrene methyl methacrylate (MMA) hexadecane liquid paraffin pyrene

from the primary beam bombardment. However, the details of the interaction process remain partially unknown, due to the limitations of present experimental techniques. In this situation, simulations become the most powerful theoretical method as an idealized replacement for experiment. Monte Carlo (MC) simulation is the most general method for secondary electron emission. Monte Carlo (MC) electron trajectory simulation techniques have been earlier studied by Koshikawa and Shimizu [71], and have been constantly improved by Joy [72], Ding [73], Shimizu [73], Reimer [74], Mutara [75], Kotera [76], and Hovington [77].

2.3.3 Temperature Dependence of the EBID

The growth rate of the deposit is strongly influenced by the temperature of the substrate since this affects the adsorption and residence time of the precursor gas molecules on the surface and thus the probability of dissociation by the electron beam. Little has been published about the dependence on substrate temperature but role of the surface diffusion in specimen contamination under electron bombardment has been emphasized by Hart [78], Muller [79] , Wall [80] , Reimer [81], Amman [82].

2.3.4 Pressure Dependence of the EBID

The deposition yield is proportional to the precursor pressure in the vicinity of the specimen. This pressure can be varied by many ways such as changing the size and shape of the specimen chamber [31] [32] [38], or changing the nozzle injector [83] [84] [67]. Kohlmann calculated the effect of nozzle geometry on deposition parameters and found an optimal inner diameter at the end of the nozzle of 80㎛ with conically increasing diameter. The molecular flow rate into the system from the vapor phase has been studied by Davies [67].

2.4 The EBID Spatial Resolution

Control of the spatial resolution is the most important factor in electron beam induced deposition and this is especially crucial for manipulation on the nanometer scale. Many authors have investigated this problem, usually based on the assumptions that secondary electrons generated in the target are the key to deposition and that the surface area over which they are emitted far exceeds that of the primary beam. Even though the radius of the electron beam on the surface is typically 3nm to 5nm, according to some authors the production of secondary electrons in the target by backscattered electrons (BSE) limits

the EBID minimum feature size at best to 15-20nm [50] [59] [66] [85].

Some authors have observed that in the particular case of tip growth, the fabrication resolution seems to be limited only by the primary beam diameter, so they promised sharper tips, provided a finer focused beam could be obtained. Kohlmann et. *al* [17] deposited material to a height of 1μm with a 50nm tip and deduced a relationship by fitting the parameters of beam current, beam energy, temperature, exposure time, and applied these parameters to develop a tip for the scanning tunneling microscope [86].

Another possible direction for improving the resolution of the fabrication is to use low energy electron beams, including even the use of scanning tunneling microscopy where the energy is as low as 1eV. In this way individual features as small as 0.8nm in diameter and 0.7nm in height were produced by Uesugi et al. [87], magnetic stripes of 5nm FWHM and 2nm high was fabricated by Pai et al. [88], and 3nm width with 4nm spacing between individual dots were obtained by Marchi [48].

CHAPTER 3

THEORETICAL BACKGROUND

3.1 Particle Beams

The fabrication devices on a scale of micrometers or less require tightly focused particle beams of photons, ions, or electrons. Since each of these beams is an electromagnetic wave, its wavelength is of importance because the Abbé diffraction limit determines the smallest beam spot. Table 3.1 are lists the wavelengths (in μm) of three particles (Photons, electrons, and protons) at various energies.

Photon beams: Photons with wavelengths between 1 and 1000nm comprise the spectrum from soft X-rays to extreme ultraviolet (EUV), to visible light. Lithography with visible, UV, or EUV radiation is a well tried process which produces circuit features with a resolution which is diffraction limited. The Abbé limit of an objective lens is determined by the size of the Airy diffraction disc formed, and the radius of the central disk is determined by the combined numerical apertures of the objective and the condenser. When the condenser and objective have equivalent numerical aperture, the Airy pattern radius from the central peak to the minimum is given by the equation (3.1).

Table 3.1. Particle wavelengths at various particle energies E_0 (eV).
[89]

Particle energy E_0 (eV)							
Particle (μm)	1	10	10^2	10^3	10^4	10^5	10^6
Photons $\lambda = \frac{1.2399}{E_0}$	1.24	1.24×10^{-1}	1.24×10^{-2}	1.24×10^{-3}	1.24×10^{-4}	1.24×10^{-5}	1.24×10^{-6}
Electrons $\frac{1.23\times10^{-3}}{(E_0+10^{-6}E_0^2)^{1/2}}$	1.23×10^{-3}	3.88×10^{-3}	1.23×10^{-4}	3.88×10^{-5}	1.22×10^{-5}	3.70×10^{-6}	8.7×10^{-7}
Protons $\lambda = \frac{28\times10^{-6}}{E_0^{1/2}}$	2.87×10^{-5}	9.70×10^{-6}	2.87×10^{-6}	9.07×10^{-7}	2.87×10^{-7}	9.70×10^{-8}	2.87×10^{-8}

$$r_{(Airy)} = \frac{1.22\lambda}{2NA_{(obj)}} \qquad (3.1)$$

Where $r_{(Airy)}$ is the radius of the Airy, λ is the wavelength of illuminating radiation, and $NA_{(obj)}$ is numerical aperture of the objective (and condenser) lenses. "NA" is dependent on the convergence angle of the inverted cone (figure 3.1) of illumination entering the objective aperture, as well as refractive index of the imaging medium:

$$NA_{(obj)} = n \cdot \sin\theta \qquad (3.2)$$

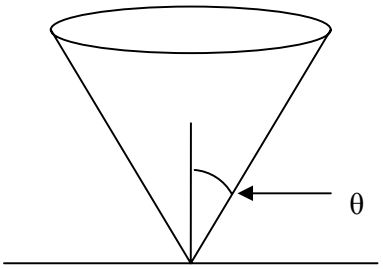


Figure 3.1: Numerical aperture angle of inverted cone

where θ is the semi-angle of the objective aperture and n is the refractive index of the medium (air, water, or oil) between the objective and the specimen. The image resolution, D is given by the equation:

$$D = \frac{k\lambda}{NA} \qquad (3.3)$$

where k is typically about 0.25 although lower values can be obtained by stratagems such as oblique illumination. The spatial resolution can be enhanced by enlarging NA or by moving to shorter wavelengths, such as deep UV light, or soft X-ray which can improve the fabrication resolution down to the sub 100nm level.

Depending on their photon energy these light sources can be used in a variety of ways for patterning and fabrication.

--- to expose resists (beam sensitive materials) to form patterns which are made visible by subsequent development and processing.

--- to directly remove materials by sputtering and erosion (ablation).

--- to deposit material directly from the beam (ion implantation) or indirectly by using the beam to stimulate a precursor gas.

For general fabrication purposes (micro and nano-scale) any of these methods is useful

within the limits set by the inherent resolution of the beam but for the special tasks considered here - the editing, correction, or repair of photolithography mask and integrated circuits (chips) - need a technique which can perform localized deposition/erosion at high resolution. Because ion beams, especially the commonly encountered Ga^+ beam stain samples by implantation the use of electron beams is the preferred method.

The ion beam processing of material can be divided into non-spatially selective methods, using a broad or flood ion beam, or spatially selective methods, using a focused ion beam (FIB). Flood or “showered” ion beam machining and milling (SIBM) employ low energy ions (50 to 1500eV) and is used as a universal etching technique to remove any unwanted material, regardless of its mechanical or chemical properties. The ions are usually generated by a liquid metal ion source (LMIS), or less often by a gas field ion source (GFIS), and are in most cases gallium Ga^+ and less often indium In^+, silicon Si^+, gold Au^+, Hydrogen H^+ or argon Ar^+. Focused ion beam machines use higher beam energies (10-50 keV) and focus the beam, typically of Ga^+ ions, into probes with diameters smaller than 10nm. Ions can be also used in lithography, employing the same resists as are employed in electron beam lithography (EBL). However, the most

advanced commercial applications of focused ion beam (FIB) technology is in micromachining by sputtering and milling, which permits the rapid and damage free generation of cross-sections and thin foils. An unavoidable problem when using FIBs in failure repair is ion implantation (staining) in device or mask. [23]

Electron beam processing is thus the best candidate for these tasks because it has the highest resolution when compared with photon and ion beam processing. Because electrons have larger wavelength than the ions of comparable energy the diffraction limited resolution is potentially significantly worse, although the higher quality of electron as compared to ion optics limits this effect. In addition electrons are not implanted, cause no staining and produce no ablation.

3.2 Basic Mechanism of EBID

The basic principles of electron beam induced deposition (EBID) are quite simple. Primary electrons (PE) from the electron gun, Backscattered Electrons (BSE), or Secondary Electrons (SE), from the target sample interact with the precursor gas molecules which are adsorbed on, or are very close to, the surface and disrupt the molecule to produce either deposition, or release a chemically active species for erosion

as illustrated in figure 3.2.

Depending on the nature of the deposit, volatile elements are removed from the chamber by the pumping system and non-volatile elements are removed by adhering to the surface. The experimental situation is thus- the material to be processed is placed beneath the electron beam and in an environment of the chosen precursor gas. The desired chemical effect will occur because of the interaction of electrons with the sample and with the gas. The PE interact directly with the gas as they pass through it traveling toward the sample. When the beam reaches the surface electron-solid interactions take place resulting in the production of emitted SE and BSE. These components can also react with gas either at, or close to, the surface.

The important question is which of these groups of electrons drives the EBID process the PE, the BSE or the SE? The working hypothesis is that the precursor gas is dissociated by energy transferred from electrons. This is possible because precursor gases for deposition/erosion are typically zero-valence compounds (e.g WF_6 and XeF_2) and so dissociation requires only a limited amount of energy. The efficiency (cross-section) of this kind of process can be generally described as having the functional form [90]

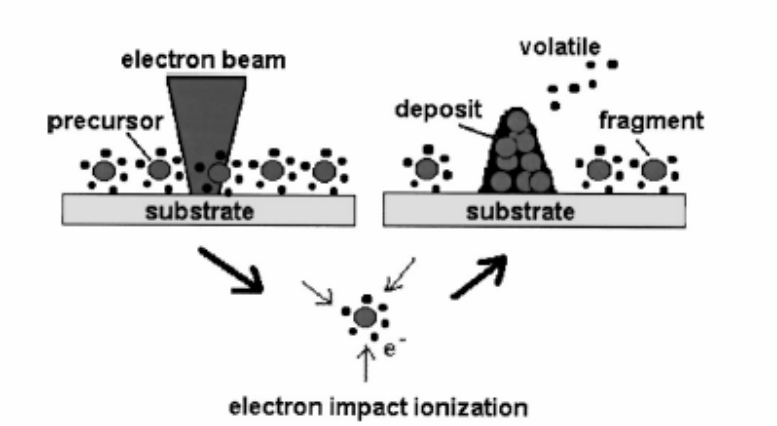


Fig. 3.2: Illustration of EBID process. [93]

$$\sigma_{diss}(E) \approx (K/E)\ln(E_{ac}/B) \qquad (3.4)$$

It can be expected that E_{ac} ≈ few eV (5 – 50 eV) [91] [92] so a consideration of this equation suggests the SE defined as having energies (0 – 50 eV) would probably more efficiently stimulate deposition than BSE (~ 50% of PE energy) or the PE. However it must be noted that depending on the beam energy and the atomic number of the target, SE may only constitute a relatively small fraction of the emitted electrons so BSE may still result in a significant contribution.

3.3 Interaction Between Electrons and Solid Matter

Electron beam induced erosion or deposition occurs as result of an interaction between the electron beam and precursor gas so the choice of gas will determine the nature of operation performed. The theory of this type of process is not yet fully developed because insufficient data on the kinetics and functional behavior of the method have not yet been obtained and analyzed, so a key goal of this thesis is to remedy this deficiency.

Electron - solid interactions start with the incident primary electron which is emitted from electron gun of the SEM or TEM. A variety of signals are generated when this

incident beam of electrons interacts with a specimen as shown in figure 3.2. After the primary electron beam hits a solid target covered with precursor molecules, a complex interaction situation arises as shown in figure 3.3. Adsorbed precursors can be dissociated by many kinds of electrons which happen to be in their proximity. Initially, primary electrons will interact with the adsorbed molecules and stimulate their dissociation. Further, it can be seen from the figure 3.4 that the primary electrons are scattered in the target so producing secondary electrons labeled SE1 which finally escape to the surface.

The primary beam also produces backscattered electrons (BSE), which in their turn can scatter within the substrate and produce supplementary secondary electrons, labeled on the surface as SE2. This labeling of secondary electrons, used in [91] takes as criteria their energy and their origin. From the figure 3.4, it is obvious that in addition to the primary electrons (PE: electrons coming from the gun), the backscattered electrons (BSE: electrons with energies between 50 eV and the incident energy experiencing elastic scattering from the target) and secondary electrons SE1 (electrons with energies up to 50 eV generated at the sample surface by inelastic collisions with the beam) and SE2 (formed by the between BSE) can also induce dissociation of adsorbed precursor

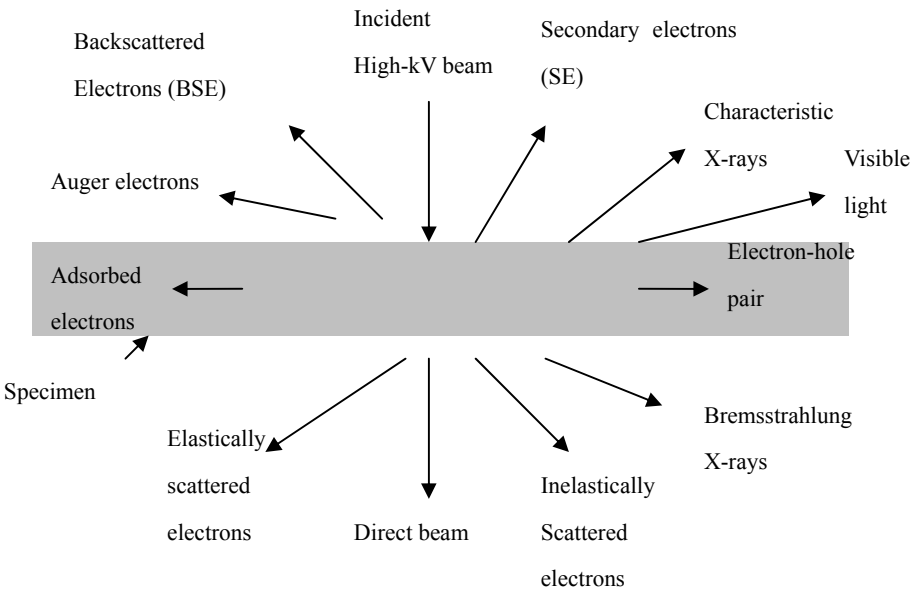


Fig 3.3: Signals generated from electron and solid interaction.

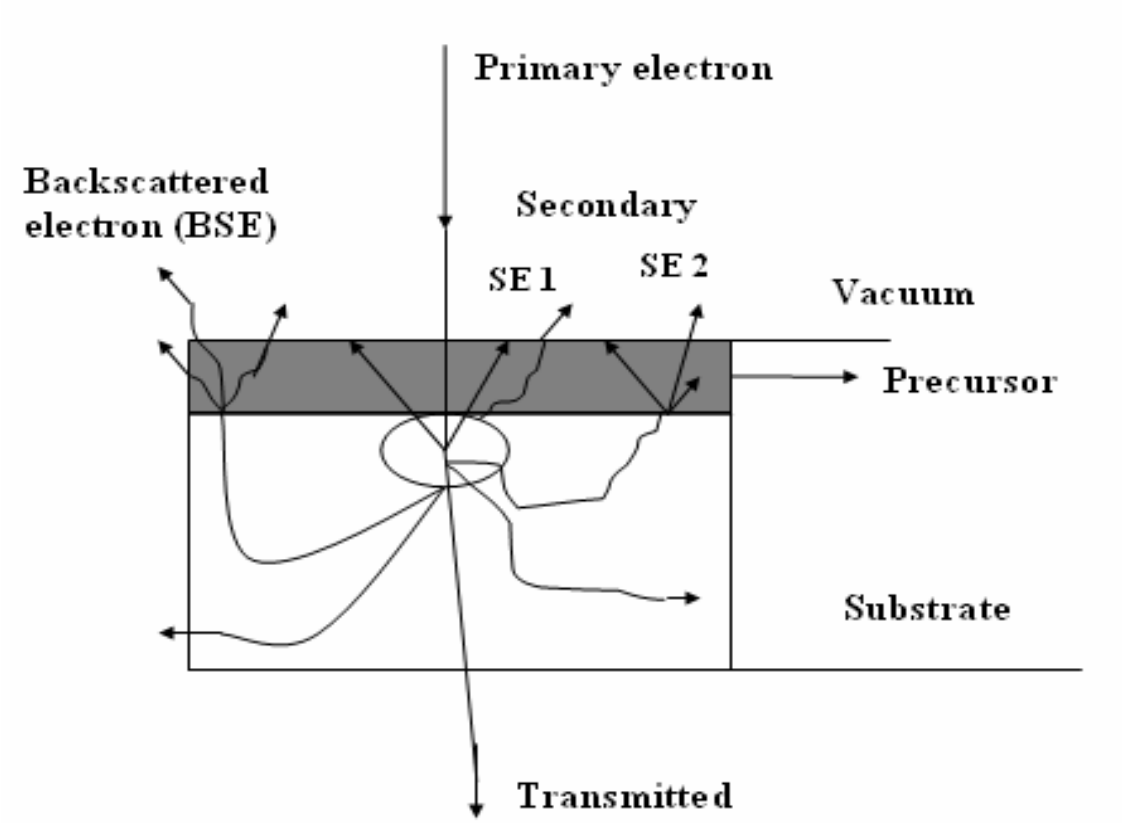


Fig 3.4: The typical EBID interaction electron-target-precursor interaction scheme.

molecules, each species of electrons with different cross-sections and making different contributions to the deposited structure shape.

These electron trajectories can be modeled by Monte-Carlo (MC) simulations using public domain programs that are readily available and suitable for use on small computers. Monte-Carlo (MC) electron trajectory simulation techniques have been earlier studied by Koshikawa and Shimizu [71] and improved by Joy [72], Ding [73], Shimizu [94], Reimer [74], Kotera [76], Hovington [77], and etc.

3.4 Growth Rate of EBID

The growth, or deposition, rate is influenced by many factors such as the exposure time, beam current, beam energy, the pressure of the chamber, and the temperature of the target. The deposition rate R(x) with beam energy of E_0 at distance x from the beam central point of incidence has unit of molecules/unit area/sec and it is given by [39] as

$$R_{SE}(x) = \int_0^{Ep} f(x, E) \cdot \sigma_{diss}(E) \cdot NdE \quad [\text{atoms}/\text{Å}^2/\text{s}] \qquad (3.5)$$

where $f(x,E)$ = the flux of electrons passing through the surface as function of the

position and energy [electrons/unit area/sec], $\sigma_{diss}(E)$ = the electron-induced dissociation cross-section of the precursor molecule [unit area] as function of the incident electron energy, N = the surface density of adsorbed precursor molecules [molecules/unit area]. The deposition rate can also be described as a volume per unit area per second as [42]

$$R_{SE}(x) = \int_{Eall} f(x, E)\sigma_{diss}(E)NVdE \qquad (3.6)$$

where V = the volume occupied by a dissociated molecule.

3.5 Spatial Resolution of the Deposit

The spatial resolution of EBID can be affected by many factors such as the scale of the electron-solid interactions, chamber pressure, temperature of the substrate, the flow of precursor gas, and the design of the gas injection system.

3.5.1 The Role of Secondary Electrons (SE)

Most models of the EBID process take into consideration only the parameters of the primary electron (PE) beam [42], but there is substantial experimental evidence that the

lateral size of features, fabricated by EBID with high energy electrons considerably exceeds the diameter of the electron beam writing tool [20] [19] [18] [17]. Many authors assume that this limitation to the feature size is caused by secondary electrons (SE) produced in the target by inelastic scattering of the primary electron and backscattered electrons. This assumption is based on the fact that the electron-impact molecular dissociation, the main process in EBID, has a cross-section which is peaked at low kinetic energies.

The growth of dot shaped deposition from secondary electrons (SE) is as illustrated in figure 3.4 and 3.5. Initially the width of the deposit is affected by the secondary electrons (SE) generated from the surface of the target but after the deposit begins to grow the primary electron beam interacts with the deposit and produces secondary electrons which emerge through the side wall of the feature being grown and result in broadening. The time dependence of the broadening of the diameter is hard to quantify because it differs with beam energy, beam current, depositing materials, substrate material, pressure, temperature and more, but qualitatively the diameter vs time is roughly described in figure 3.6. An exact prediction of the diameter as a function of time is difficult because it is affected by so many factors such as the settings of electron optics, the cleanliness of

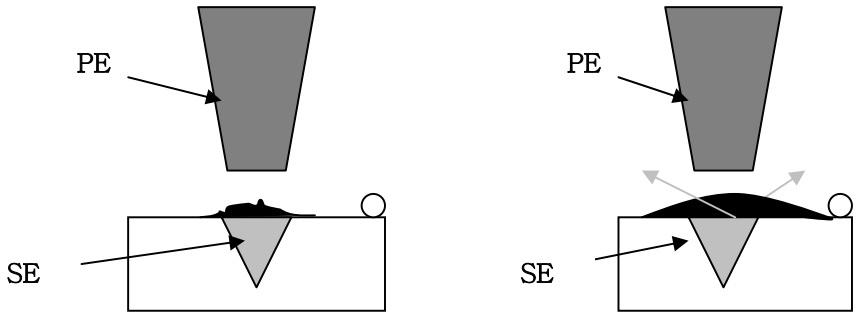


Figure 3.5: The role of secondary electrons (SE) at different growth moments: (a) in the beginning, (b) after a tip structure has grown. [23]

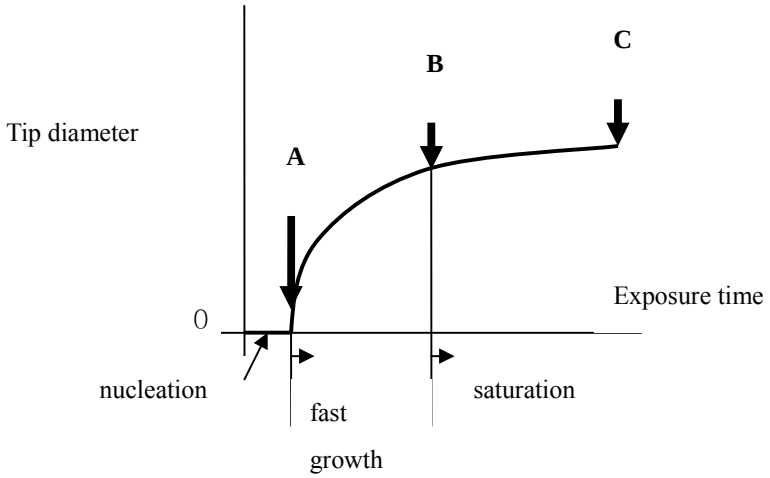


Figure 3.6: A typical curve showing the evolution of the cone diameter [23]

$$R_{SE}(x) = \int_0^{Ep} f_{SE}(x, E)\sigma_{diss}(E)NdE \quad [\text{atoms/Å}^2/\text{s}] \qquad (3.7)$$

the SEM chamber, the partial pressure of the precursor gas, the surface diffusion of the gas molecules and the cleanliness of the sample surface. The dissociation rate produced by secondary electrons will be given by

Most researchers have started with a Monte-Carlo simulation or an analytical model and then determined the SE spatial and energy distributions on the target surface, $f_{SE}(x, E)$ to estimate $R_{SE}(x)$. But due to the lack of information about the dissociation cross section $\sigma_{diss}(E)$, this topic remains an ongoing research area and there is as yet no clear consensus about the growth mechanism. This topic will be considered later in this thesis.

3.6 Influence of Beam Energy

The electron beam energy plays a critical role in determining the growth and lateral size because it determines the dissociation cross section of the beam with the precursor gas and the electron beam interaction volume within the substrate. The general dependence of the dissociation cross section on incident electron energy can be written as [90]

$$\sigma_{diss}(E) \approx (K/E)\ln(E/B) \qquad (3.8)$$

where K and B are constants. From equation (3.8) the dissociation cross section is proportional to the inverse of the beam energy and this term affects the growth rate in equation (3.5). The lateral growth rate of the deposit is related to the secondary electron yield coming from the surface of the substrate and this is also related to the interaction volume of the electron and to the target material due to the escape of the SE and BSE which depend on the depth of the interaction volume.

The interaction volume is determined by the electron beam energy, the atomic number of the target material and tilt angle of the specimen to the electron beam [95]. Figure 3.7 shows the effect of electron interaction volume with the material. Higher beam energies and lower atomic number material result in larger interaction volume versus those obtained at low beam energy and higher atomic number materials. This phenomenon affects the generation of the SE and BSE distribution on the surface of the substrate and changes the size or the shape of the depositing material.

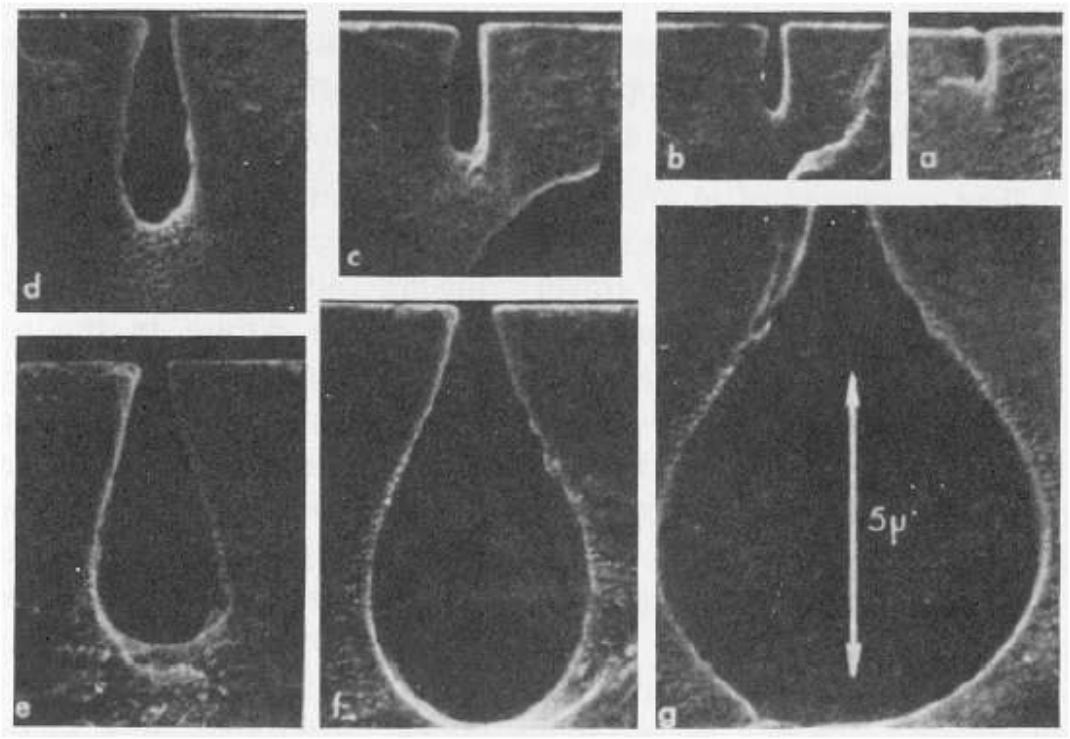


Figure 3.7: Direct visualization of the electron volume in polymethylemethacrylate. In (a) through (g), the electron dose is the same, but the etching time is increased progressively to reveal successively lower energy deposition (radiation damage) levels (from Everhart *et* a*l*., 1972). [95]

3.7 Temperature Effect on EBID

The temperature of the substrate, or of the deposited material, plays a critical role in determining the growth rate and shape. The majority of the interaction above or just at the substrate subsurface is governed by the temperature. This also determines the crystal structure of the deposit and its electric properties, such as conductivity or the work function, which are of importance for the electron emission tip growth. [96]. The number of available precursor gas molecules is governed by the surface population of an adsorbate, n_a, and is given by

$$n_a = \left[\frac{p}{\sqrt{2\pi MRT}} \right] \tau_0 \exp[\Delta H_{des}/RT] \qquad (3.9)$$

where P is the pressure, M is the molecular weight, R is the universal gas constant, τ_0 is the inverse of the frequency, and ΔH_{des} is the enthalpy of desorption [97] [98]. The above equation (3.9) shows that the number of molecules on the surface of the substrate will decrease as the temperature of the substrate is increased. This leads to the reduction of the growth rate of deposit and also affect of the shape of the deposit. Randolph *et al*. [98] compared experimental and simulation data for the growth of oxide from

tetraethylorthosilicate TEOS as function of temperature and find that the growth rate of SiO_2 decreases with higher temperature and satisfies an Arrhenius relation.

The heat accumulated as the result of the energy transfer from the primary electrons (PE) will increase as the deposition time gets longer, and the number of the precursor gas molecules on surface of the pre-deposited material will be reduced. We could see growth rate reduction from growth of SiO_2 and W in chapter 5.6 with stable gas flow. This tells that the reason for this not the mass transport limit but due to the heat by the PE and caused reduction of adsorbed gas molecules. This will affect the radius of the deposit and the distribution of secondary electron emitted from the pre-deposited material will differ from that found on a plane substrate, so the shape and the size will affected significantly by the temperature.

3.8 Thickness Determining Factors

The number of gas molecules which impinge on the substrate per unit area at unit time is proportional to the gas pressure. The pressure dependence of the deposited thickness is dependent on the quantity of precursor gas on the substrate surface. That is to say, a higher pressure supplies a larger number of precursor gas molecules on the surface.

Therefore the deposited thickness is enhanced with increasing precursor gas pressure.

The film thickness also depends on the electron dose and this is related to the exposure time of the beam irradiated area. So the deposited film thickness d is proportional to the electron beam exposure time t. Therefore the deposited film thickness d becomes

$$d=Rt \qquad (3.10)$$

where R is growth rate for electron beam deposition. The constant R varies with any change of the environment of deposition experiment. Kohlmann calculated the deposition rate as a function of the current density of the primary beam with as variable parameter the gas flux on the surface. [99] While the growth rate reduction with increasing beam energy at a constant dose per scan was explored by Hoyle. [64] Their results show with beam energies of 2, 5, 10, 15, 20 KeV with fixed current as 4 ± 0.02 nA gave thicknesses of 0.55, 0.33, 0.38, 0.35, and 0.33 μm.

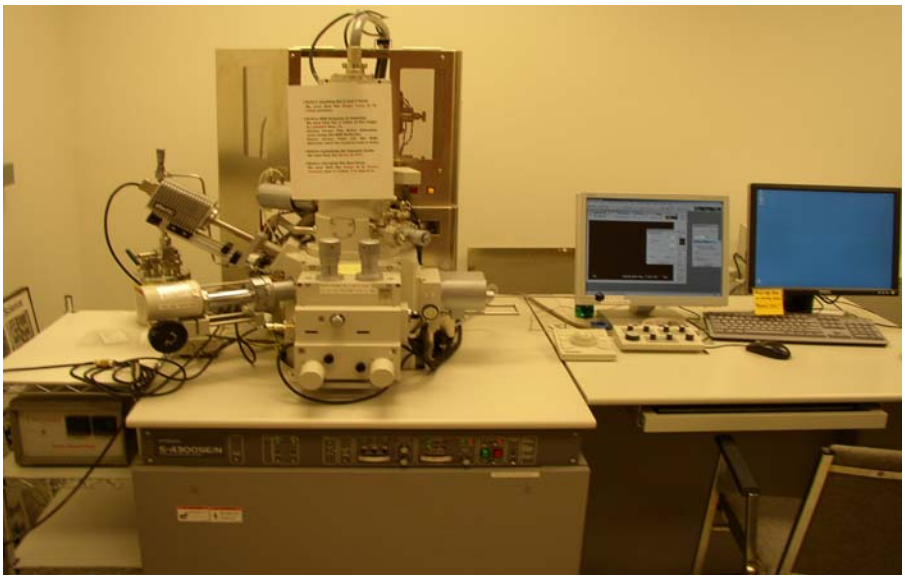
CHAPTER 4

EXPERIMENTAL EQUIPMENT AND PROCEDURES

4.1 Experimental Procedures for EBID

4.1.1 Scanning Electron Microscope (SEM)

The accurate fabrication of submicron features with an electron beam requires a small beam radius such as is provided by a commercial scanning electron microscope (SEM). The work described here was performed on a Hitachi S-3500 VPSEM (Variable Pressure or Environmental SEM) and a Hitachi S-4300/N SE as shown in Fig. 4.1. An important consideration is the cleanliness of the specimen chamber vacuum. If this is contaminated by hydro-carbons then the metal deposited will be mixed with carbon leading to poor mechanical and electrical properties. However in our Hitachi S4300 SE/N, which uses a Schottky field emission gun, the sample chamber is dry pumped to a working pressure of about 1E-6 Torr and a residual gas analysis shows that most of this is attributable to air and to water vapor. The hydrocarbon background is below 1E-8 Torr in magnitude and should have negligible effect on the process (figure 4.2).



(a)



(b)

Figure 4.1: Fabrication and etching facilities. (a) Hitachi S 4300/N SE (b) Hitachi S-3500N scanning electron microscope (SEM) for the EBID experiment attached with SE, BSE, and X-ray detectors.

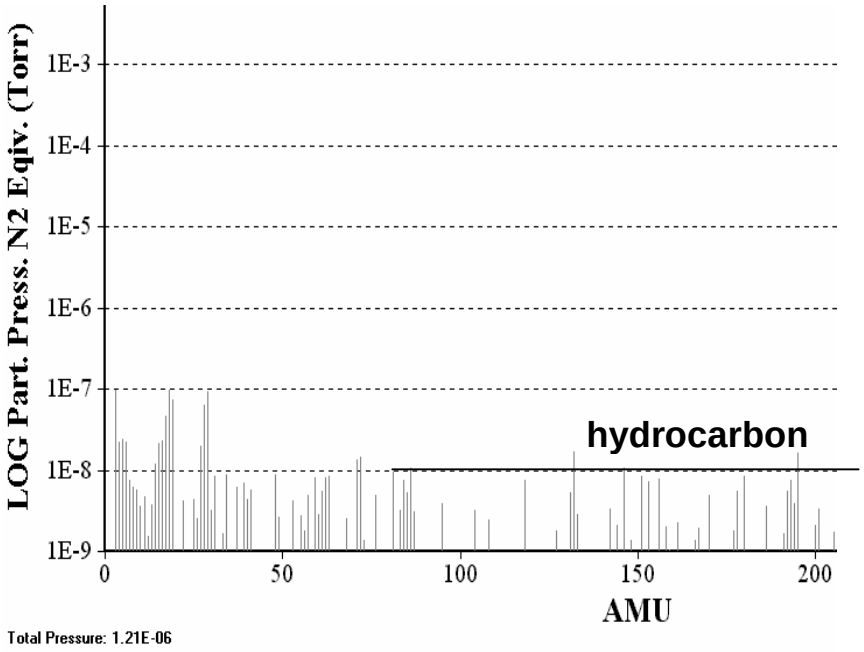


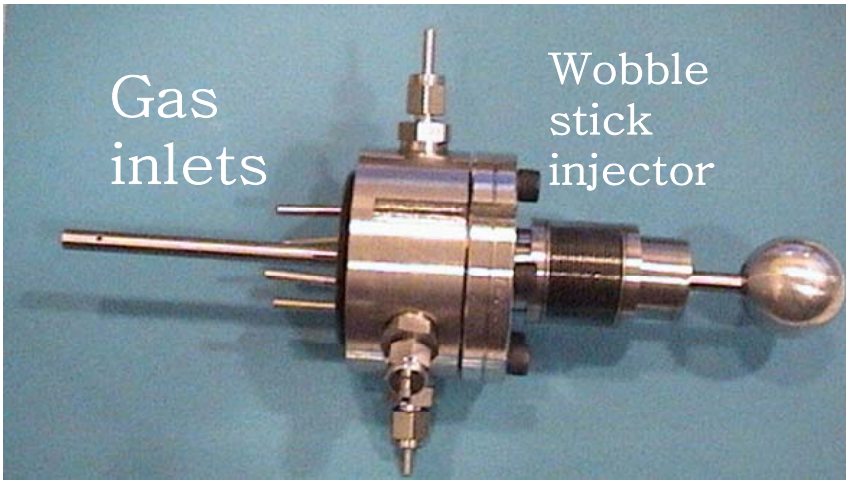
Figure 4.2: Chamber environment of S-4300 SE/N measured by Residual Gas Analyzer (RGA)

4.1.2 Gas Injection System

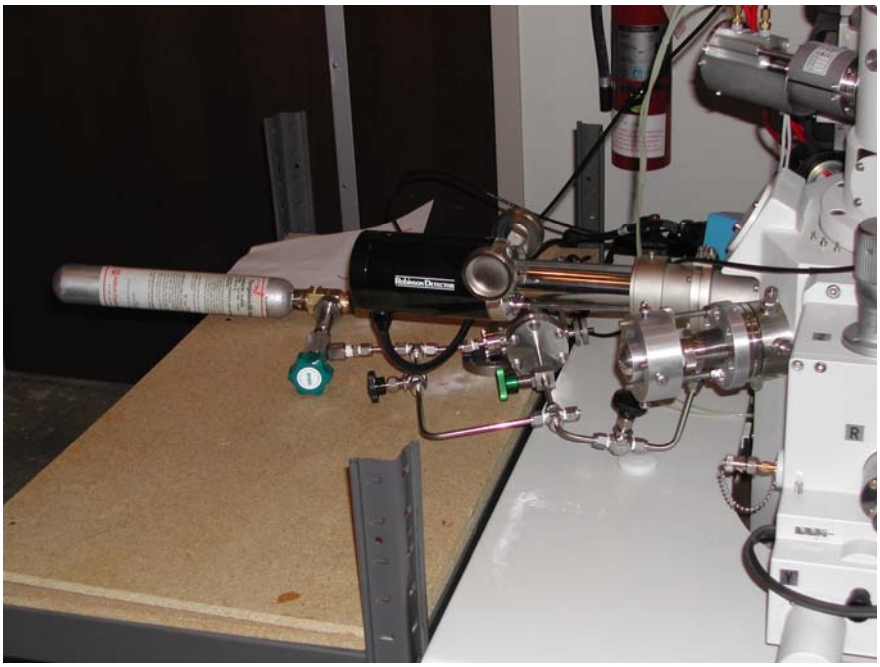
Precursor gas was injected into the SEM chamber through a wobble stick manipulator system equipped with four nozzles as shown in Fig. 4.3 (a) and attached to the SEM as seen in Fig 4.3 (b). The precursor gas is injected at about 1mm above the sample by manually controlling the needle position from outside of the SEM. The deposition process is monitored *in situ* by using the energy dispersive X-ray spectrometer (EDS) system attached to the microscope. From an analysis of relative height of peaks in the spectra the thickness of the deposition can be measured with good precision by applying a calibration curve derived from Monte Carlo simulations. Originally, silicon tubing was used in the gas injection system to deliver the gas from the outside metal tubing to the hypodermic needle. Later, it was found necessary to change this to neoprene tubing to avoid the reaction of fluorine with the silicon which caused contamination to the deposited material, and corrosion.

4.2 Precursors Gases

For tungsten deposition tungsten hexa-carbonyl ($W(CO)_6$) and tungsten hexafluoride (WF_6) are the most commonly used precursors and these were selected as the initial



(a)



(b)

Figure. 4.3: Gas injection system. (a) for 3-dimensional manipulation (b) Gas injection system attached to the Hitachi S-4300 SE/N.

choices for this work. Both of these choices have both positive and negative features.

4.2.1. Tungsten hexa-carbonyl: $W(CO)_6$

Most of the relevant work reported in the literature has been focused on the selective deposition of tungsten (W) using tungsten hexa-carbonyl $W(CO)_6$ as the precursor [31] [61] [60] [62] [100] [64] [17]. $W(CO)_6$ is a solid at room temperature and pressure and so must be heated to 80~95°C in order to reach a vapor pressure large enough to deliver ~0.1 Pa of gas into the SEM. Heating the solid provides a convenient way of controlling the gas flow, but $W(CO)_6$ is prone to condense in the delivery tubing making it necessary to clean or change the tubing after almost every experimental run. In addition the material deposited was shown by Auger analysis to contain over 70% of carbon, as well as a significant amount of oxygen contamination. While the presence of carbon is not a problem for mask applications, because it is a good UV absorber, the presence of the carbon and oxygen significantly increases the resistivity of the tungsten rendering the deposited metal unsuitable for circuit repair applications. The decision was therefore made to change the precursor gas to WF_6.

4.2.2 Tungsten hexa-fluoride: WF_6

Compared with $W(CO)_6$, tungsten hexa-fluoride (WF_6) is easy to use because it has a low melting point (~ 2.5°C) and is thus a liquid at room temperature with a high vapor pressure. It is therefore not necessary to heat the precursor and there is no chance of the gas decomposing and depositing metal so blocking the delivery tubing into the SEM chamber. However, WF_6 is highly toxic, requiring us to equip the SEM with a specially designed gas extraction system to safely remove the gas from the laboratory. In addition the fluorine released during metal deposition causes corrosion to the vacuum fittings and electrical wiring in the sample chamber of the SEM and degrades and ultimately destroys the vacuum pump oils. During this experimental work these problems were mitigated by frequently changing the pump oils and carefully cleaning the sample chamber.

4.3 Experimental Procedure

4.3.1 Deposition with Tungsten hexa-carbonyl ($W(CO)_6$)

Initially hexa-carbonyl ($W(CO)_6$) precursor was employed for the deposition of tungsten metal using the S-3500 VP SEM which has a thermionic electron emission gun. As supplied $W(CO)_6$ is a white powder at room temperature and so it needs to be heated to

inject the vapor into the SEM. The $W(CO)_6$ powder was ground in a mortar and pestle and then put it in a 25ml glass flask, and warmed on a hot plate up to 80℃ using plastic tubing to connect the flask to the injection device. During the early trials the high pressure generated in the glass flask caused the plastic tubing to pop out and become unstable, so this arrangement was replaced with a 10ml metal cylinder and wrapped with heating tape to avoid condensation due to the temperature variation of $W(CO)_6$. Maintaining the temperature of the flow system within a small range was critical for avoiding the blockage of the metal tubing due to condensation. If the temperature was allowed to drop too low then the precursor condensed and caused a blockage. If the temperature was allowed to get too high then the precursor dissociated in the delivering tube rather than on the sample surface. At the end of every experiment, it was found necessary to change the metal tubing due to the temperature drop caused by the blockage that had built up.

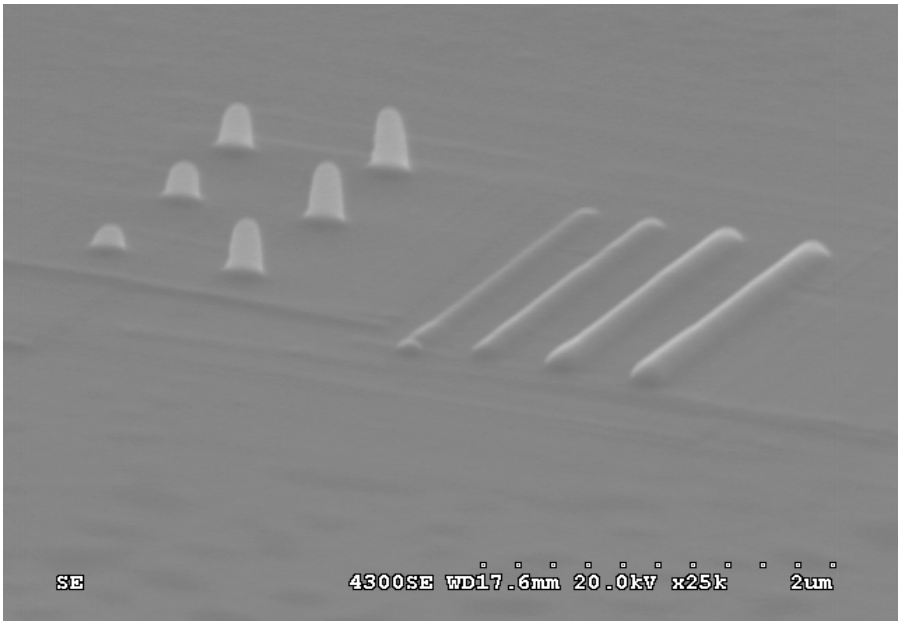
4.3.2 Deposition with Tungsten hexafluoride (WF_6)

Deposition using tungsten hexafluoride as a precursor proceeds in a similar way although there are now no problems with the blockage of the delivery tube due to the condensation

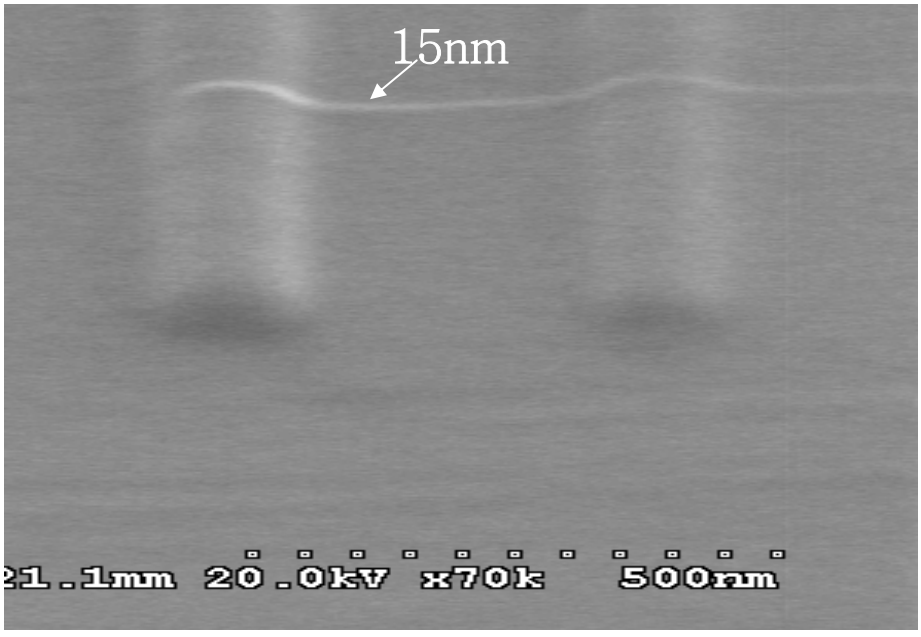
of tungsten as experienced when $W(CO)_6$ is used as a precursor. Auger spectroscopy confirms that the deposited material is pure tungsten with only traces of carbon. Depositions produced by slow (few milliseconds per pixel) line scans show line width which are typically 100nm wide or more with a half-cylindrical cross-section. High speed (few tens of microseconds per pixel) line scans i.e. smaller electron doses with the same beam conditions (with effective dwell times of below 1μs/pixel), however, give much finer lines as illustrated in Fig. 4.4 (a) and (b). Flyback of the incident beam produced 15nm lines on the larger feature written at slower speeds. It is assumed that this is due to residual WF_6 that remains for a short time on the substrate and is activated during the flyback of the beam at the end of a scan frame.

4.4 Experiments for Pressure Effect

To study the effects of pressure on deposition, tetraethylorthosilicate (TEOS) and WF_6 precursor were used to deposit tungsten and SiOx nanopillars. The growth was performed at three different pressure regimes, $1x10^{-3}$Pa ("low"), $3.6x10^{-3}$Pa ("medium"), and $8x10^{-3}$Pa ("high") which were monitored by the Penning gauge that was attached to the SEM. The localized pressure below the injector is likely 2-3 orders of magnitude



(a)



(b)

Figure 4.4: Deposition with WF_6. (a) Tilted image of deposition with WF_6 for 10 sec to 60 sec. (Beam energy:1 Kev, Current: 20 pA, Magification:45 K) (b) Very fine line of tungsten deposited by high speed scan.

higher than the background pressure of ~$7x10^{-5}$Pa in the chamber [66] [58]. The beam energy was 20 KeV and the beam current was measured using a Faraday cup mounted on the sample stage for each pressure. Once the beam was accurately focused, the microscope settings were not changed during the course of the experiment as shown in figure 4.5. The beam current changed slightly during the course of the experiments and the specific currents for the experiments were: for TEOS, $I_{faraday}$=(3.78pA at $8x10^{-3}$Pa, 4.72pA at $3.6x10^{-3}$Pa, 4.68pA at $1x10^{-3}$Pa); for WF_6, $I_{faraday}$=(3.81pA at $8x10^{-3}$Pa, 3.77pA at $3.6x10^{-3}$Pa, 3.83pA at $1x10^{-3}$Pa). The magnification of the SEM during the growth process was fixed at 50,000x, and the temperature of the substrate was fixed as room temperature. The growth time was varied from 6 to 420 seconds and was changed in increments of 10 seconds up to 1 minute, 20 seconds up to 2 minutes and then increased by 1 minute up to 7 minutes. The deposition of SiOx and tungsten was done using the spot mode of the SEM to grow pillars so as to see the height and aspect ratio distinctively. The shapes and sizes of the deposited features were measured *in situ* by high-resolution SEM imaging after the deposition was completed by tilting the specimen stage 60 degrees.

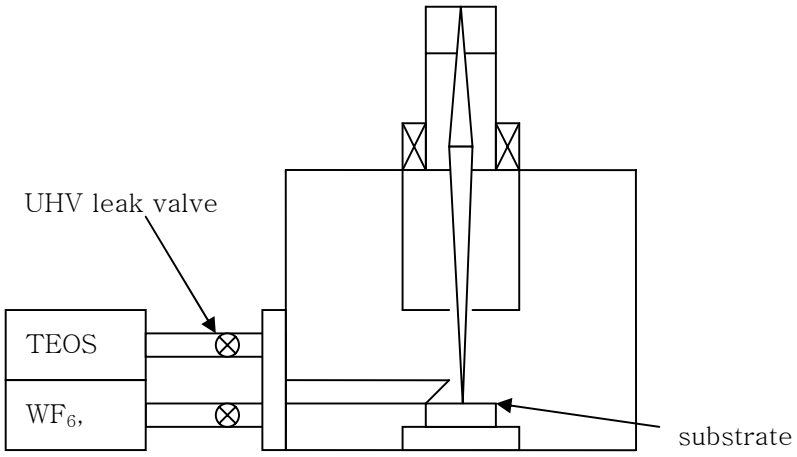


Figure 4.5: The system set up for deposition with different pressure with TEOS and W precursor gas.

4.5 Temperature Dependence

Deposition of material using the EBID technique is based on an interaction between the electron beam and the substrate. Energy transfer from the electron beam to the substrate generates heat in the area where we wish to produce a deposit. This temperature rise, added to the base temperature of the substrate plays an important role in determining the growth rate of the deposition process. In this experiment, we performed depositions on commercial chrome and quartz (Cr/Qtz) binary masks while changing the temperature of the mask using Peltier cold stage (figure 4.6).

In this experiment, a piece of a binary mask was mounted on the cold stage using copper tape to ensure good conduction of heat from the stage to the mask. The temperature was varied from -20 to 70℃ in increments of 10℃, the deposition time for each box was 3 minutes with beam energy of 20 KeV in variable pressure mode with 50Pa of chamber pressure.

4.6 Effect of Scan Mode of SEM

The scan mode is an important factor for determining the size of the feature of the deposits. The “scan mode” of the SEM described the way in which the electron beam is

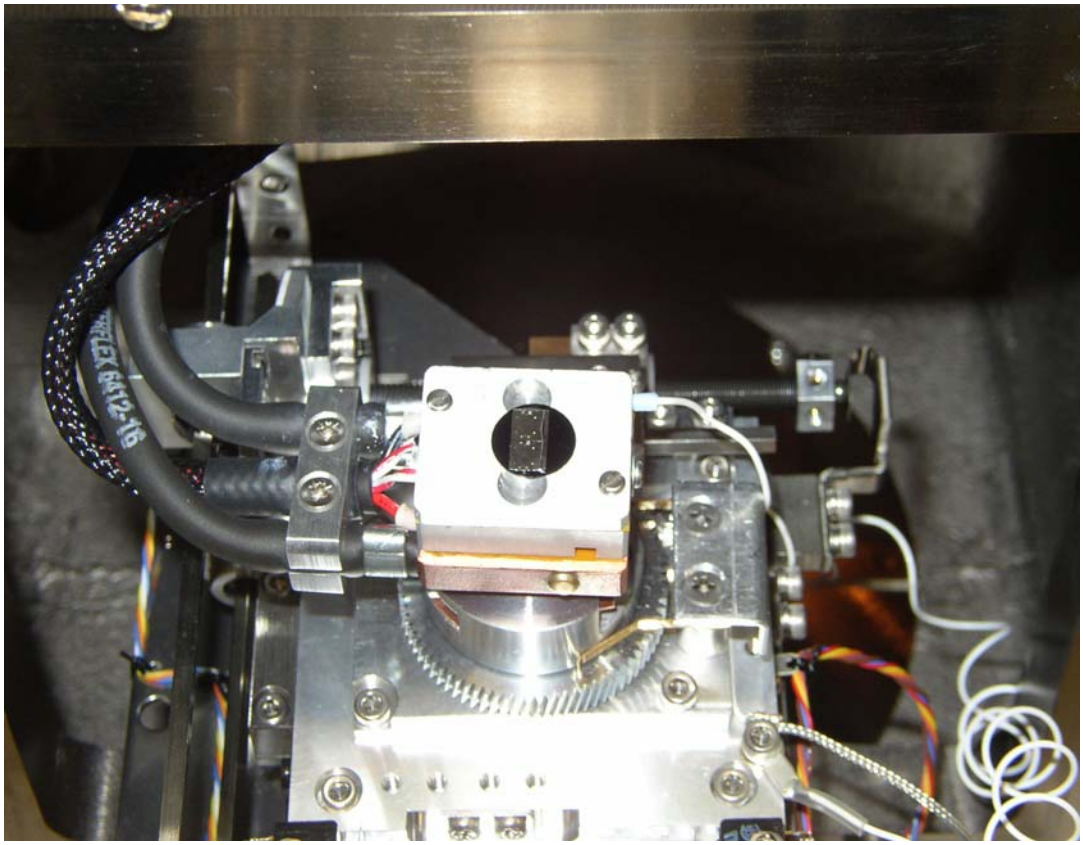


Figure 4.6: Peltier cold stage connected to the sample holder of SEM for control of temperature of the substrate.

scanned (“rastered”) over the sample. In line mode the beam is scanned either once, or repetitively, along a horizontal track. This can be accomplished over a wide range of speeds ranging from about 10 microseconds per pixel up to tens of milliseconds per pixel. In spot mode the beam remains stationary on a selected pixel for a chosen period time. In scan mode the beam is rastered over a range of X and Y position at a chosen dwell time (varying from 1μsec. per pixel (TV1) to 20 milliseconds per pixel (SLOW2) scan). Therefore deposition with four different scan modes (Scanning speeds of the beam for a line from the manual are TV=0.225sec/frame, SLOW1=0.35ses/frame and SLOW2=2sec/frame) has been experimented with the condition of 20KeV beam energy, 2.7nA of beam current pressure of $3.3x10^{-3}$ Pa, 10000x of magnification for 2 minutes of beam irradiation. Figure 4.7 is showing that widths of the lines are changed with the scan mode of SEM.

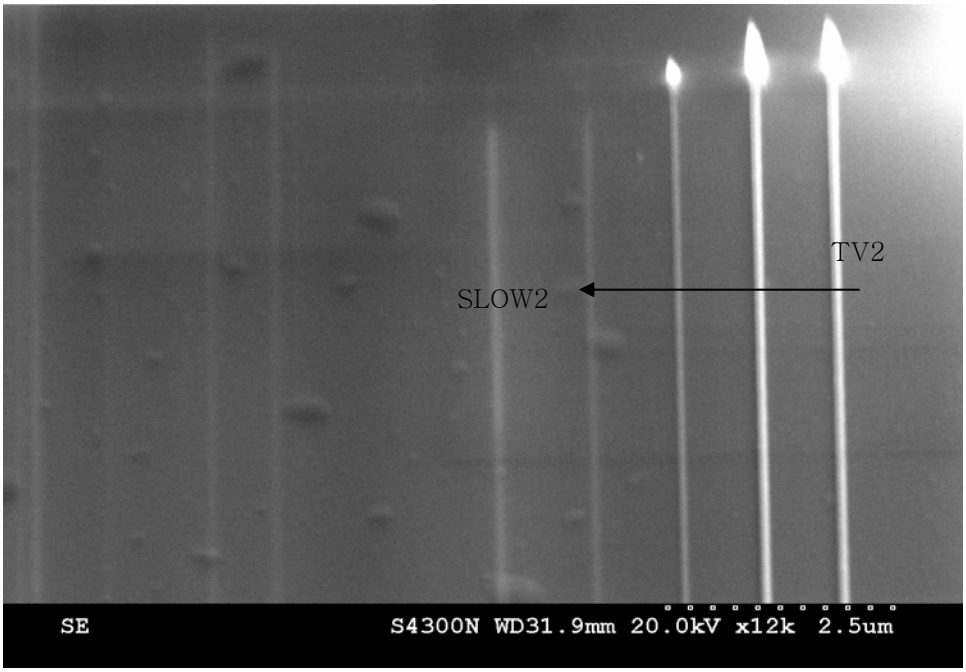


Figure 4.7: Deposition of tungsten lines with different scan modes (TV2, TV1, SLOW2, SLOW1).

CHAPTER 5

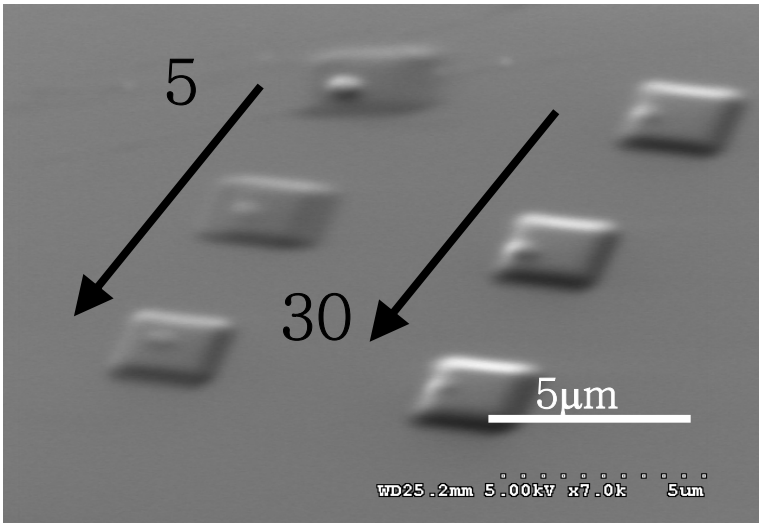
RESULTS AND DISCUSSION

5.1 Characterization of $W(CO)_6$ Deposits

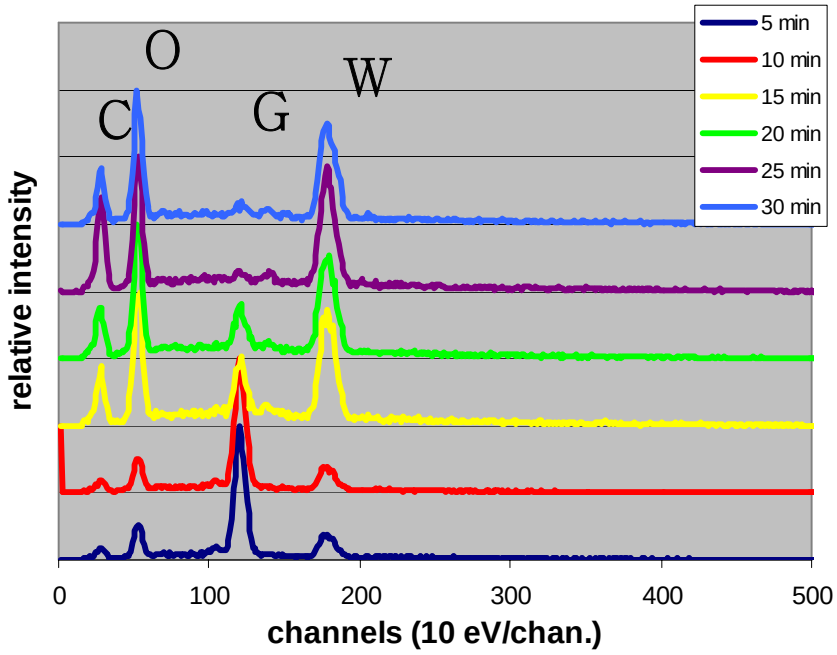
The thickness of the EBID metal films was measured *in situ* and during deposition by performing energy dispersive X-ray microanalysis on them with the electron beam. The procedure involved by measuring the ratio of the height of the tungsten M line peak in the spectrum to that of a suitable peak from the substrate. Because the most convenient X-ray emission from the tungsten is an M-line which exactly overlaps the silicon K-line at 1.74 KeV, the decision was made to use germanium as the substrate material. This is not expected to have any effect on the deposition process. Monte Carlo simulations [Win-Casino version 2.0, Drouin *et al*.] [101] were performed to produce a calibration curve for the thickness of the deposited tungsten as a function of the height of the tungsten to germanium ratio in the X-ray spectrum.

5.2 Calibrating Layer Thickness

Fig. 5.1 (a) and (b) shows the results of deposition using a $W(CO)_6$ precursor. A series of 2.5μm x 2.5 μm tungsten boxes were deposited over a range of times varying from 5~30 minutes in 5 minute increments and using a 5 keV beam energy. Fig. 5.1 (a) is a SEM micrograph of the six deposits with increasing $W(CO)_6$ exposure and Fig. 5.1 (b) shows the EDS spectra acquired using a probe beam energy of 5keV, after each run, illustrating how the germanium signal from the substrate decreases and the tungsten, carbon, and oxygen peaks simultaneously increase with increasing time. In absolute terms it takes about one thousand incident electrons to deposit one tungsten atom for $W(CO)_6$ case (1.6 picograms from 2.5μC incident dose), which is a relatively high efficiency process. Auger spectra, Fig. 5.2 (a) and (b) recorded on a PHI 680 Scanning Auger Microprobe also confirm that tungsten is being deposited. A quantitative analysis of the spectra shows that the material consists of 12 atomic percent of tungsten and 70 atomic percent of carbon, a ratio which is close to that of the precursor itself. The high amount of carbon does not greatly disturb the efficiency of the deposit as a EUV absorber, but it does result in a lower electrical conductivity and so $W(CO)_6$ chemistry is not a good candidate for electric circuit repair where the high resistivity would slow device response. Auger

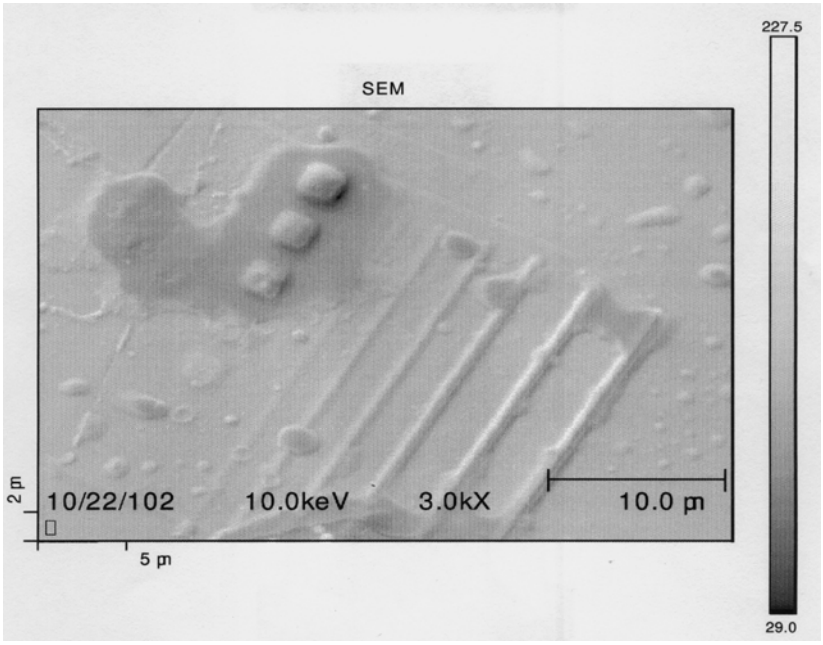


(a)

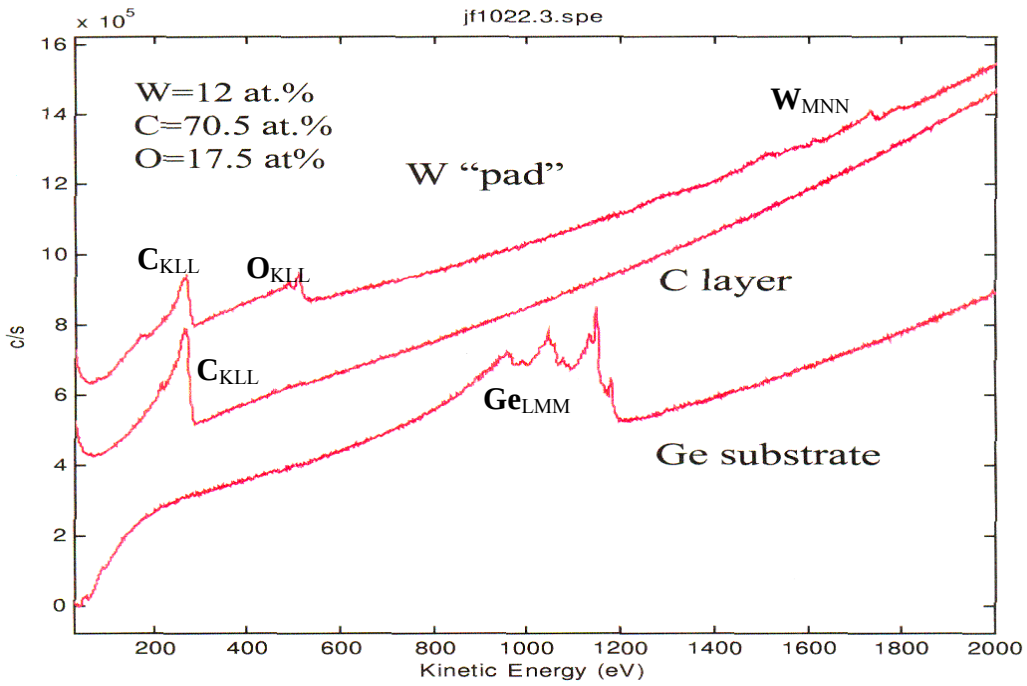


(b)

Figure 5.1: Tungsten deposition with increasing time: (a) 2.5µm x 2.5µm tungsten box deposition using $W(CO)_6$ precursor. (b) EDS spectra of deposits of Fig. 4.4 (a).



(a)



(b)

Figure 5.2: Measurement of tungsten with $W(CO)_6$ precursor: (a) scanned area for the Auger analysis, (b) Auger spectra from the PHI 680.

analysis also shows that carbon contamination builds up around features that have previously been written, probably as the result of residues of the precursor and hydrocarbons in the specimen chamber. Therefore this carbon deposition degrades the resolution of the deposited features.

The deposit thickness was derived from calibration curves computed from the 'Win Casino' Monte Carlo simulation. This simulation package employs Mott scattering to describe the electron interactions, an improved stopping power model corrected for low energies, and the Casnati X-ray cross-sections and has been shown to produce reliable data. The ratio of the tungsten (M) line to germanium (K) line (Fig 5.3 (a)) X-ray counts is monotonically proportional to the thickness of the tungsten layer. Figure 5.3 (b) shows the computed calibration curve for 5keV beam energy for the thickness of the tungsten layer as a function of the Ge/W peak ratio. From the simulation, a ratio of Ge/W of 25 is equivalent to a 3nm thickness and a Ge/W ratio of 2 is equivalent to a deposition thickness of 15nm. This simple approach is therefore highly sensitive to the nano-meter thickness deposits. In our simulation, carbon and oxygen components were not included but this omission does not cause a significant error because these elements only cause a small change in the X-ray absorption coefficient at the W L-line. This measurement

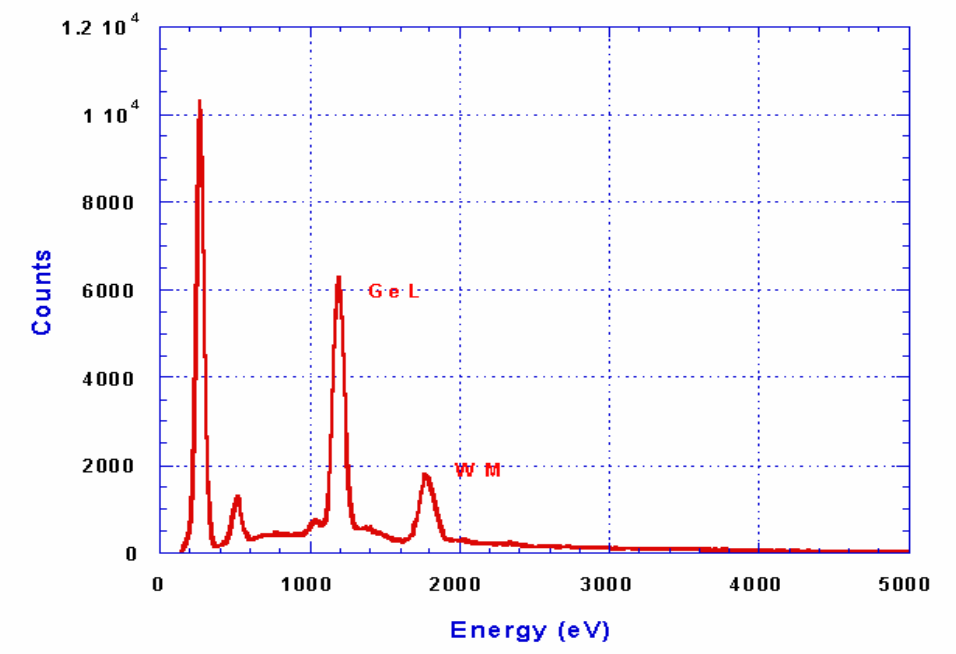


Figure 5.3: Calculation of thickness by integrated intensity of X-ray peak ratio: (a) X-ray analysis after $W(CO)_6$ deposition with beam energy of 10 KeV for 5 minutes on germanium, (b) Ge/W peak ratio versus tungsten thickness from simulation.

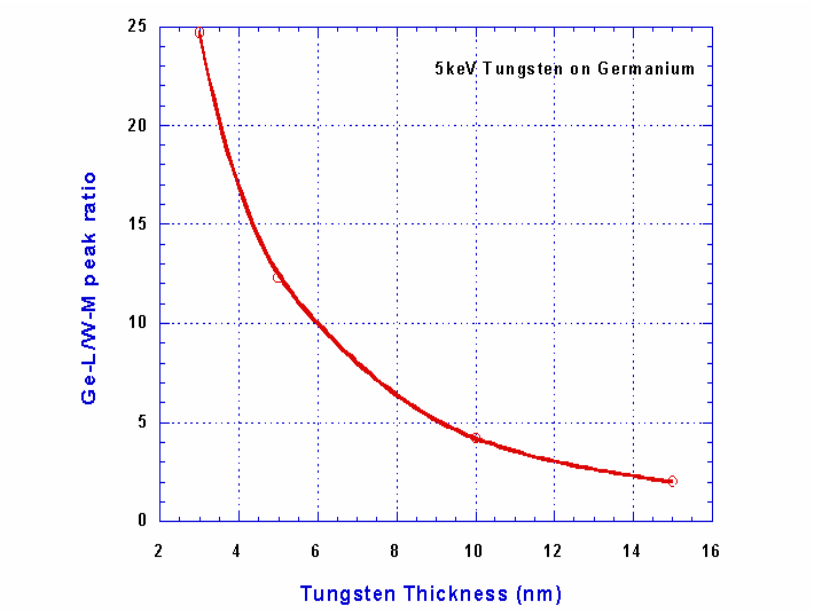


Figure 5.3: Continued

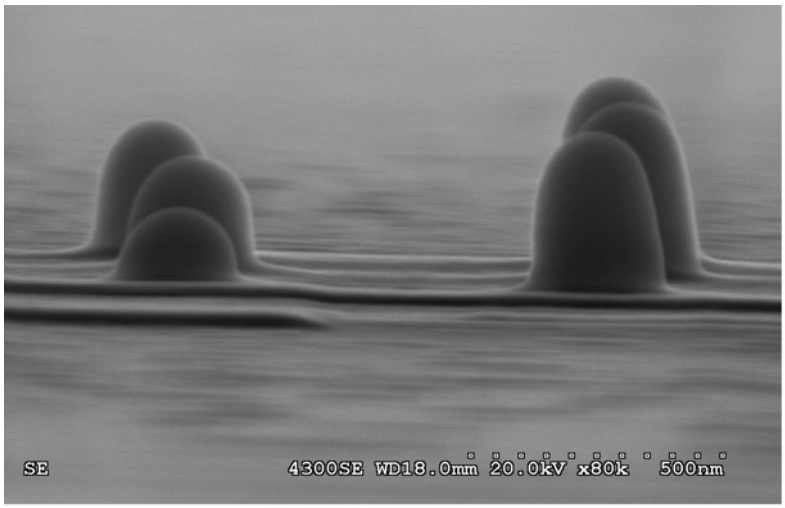
(b) Calibration curve for Ge/W peak ratio versus tungsten thickness from simulation

procedure is for rough estimation of W thickness since the ratio of tungsten in the film was small compare to carbon and oxygen.

5.3 Growth Rate of Deposits

The growth rate of the deposition is the one of the important factor that must be considered because it changes with every factor of the conditions employed such as pressure, temperature, beam energy, beam current, precursor gas, and so on. Deposition was studied in two different scan modes, spot and line, to compare the growth rate of the tungsten deposition as shown in figure 5.4 (a), (b) and (c). The variation of the measured height of the deposits is shown in figure 5.4 (c).

From the figures it can be seen that the growth rate falls with increasing time in both spot and line mode depositions. In the case of the spot mode irradiation, the growth rate is not linear with time, instead the growth is fastest initially but then falls as time increases. This might be explained as being the result of heating the deposited material resulting in a reduction of the sticking coefficient of gas on the surface and, therefore, a lower effective supply of molecules for dissociation [17]. The growth rate of line features is more difficult to quantify because of their large contact area compared to spot mode



(a)



(b)

Figure 5.4: Deposition with WF_6 : (a) with spot mode for 10-60 sec.(beam energy 1 keV, specimen current 3pA), (b) with line mode for 30-120 sec. with 30 sec. increment (beam energy 1 keV, specimen current 3pA), (c) comparison of growth rate with spot and line mode.

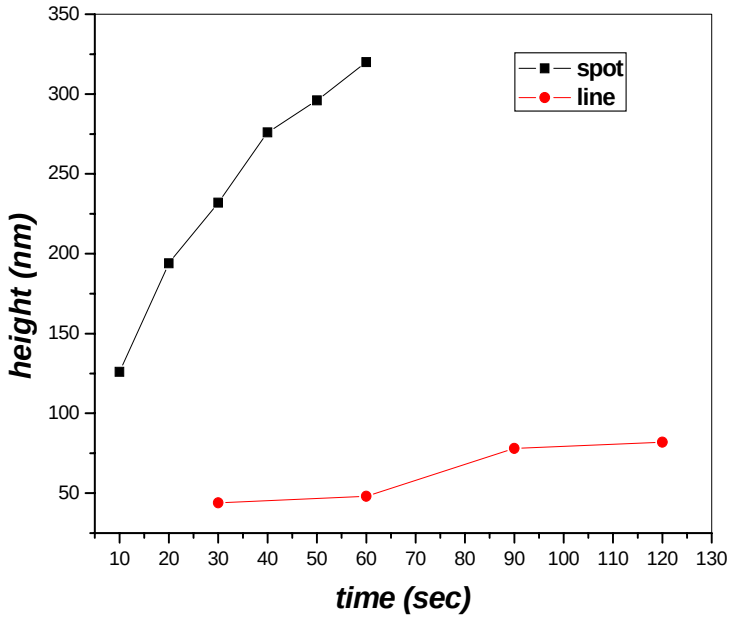


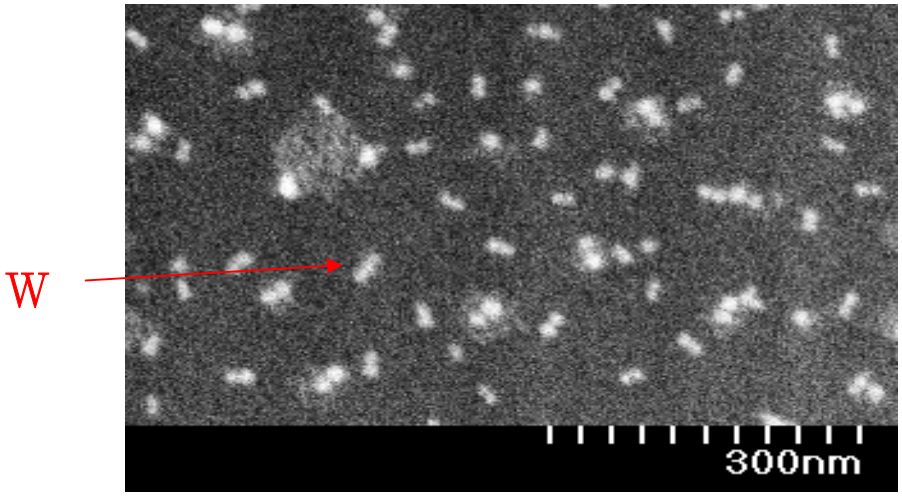
Figure 5.4: Continued

(c) Comparison of growth rate with spot and line mode.

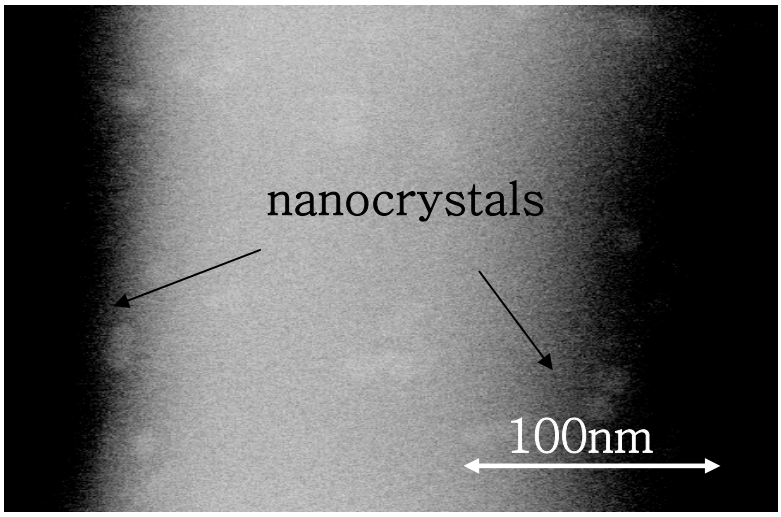
depositions and geometry of the surface. Visually, depositions from WF_6 are very similar to those from $W(CO)_6$ in both size and shape for equivalent beam conditions, but because transferring WF_6 is much easier than $W(CO)_6$ this choice of precursor is now preferred.

A careful examination of areas of the substrate well away from written features showed the presence of nano-sized particles. Scanning Transmission Electron Microscopy (STEM) imaging of thin carbon substrates written with WF_6 confirmed that these particles were dimer or trimers of tungsten spheres about 10nm in diameter as shown in figure 5.5 (a) . These small particles were only observed when the experiment was carried out with water vapor present from the metal cylinder connected to SEM during the deposition. When employing $W(CO)_6$ as precursor this phenomenon was also absent. This unexpected observation might provide an efficient new method to generate nanoscale metallic particles for many uses.

An examination of thin deposited layers of tungsten using the STEM shows them to be essentially amorphous in nature, with no indications of either grain structure or any boundaries. This suggests that molecules that sticks to the surface do not migrate before being decomposed by electrons, and also that the residue then stays fixed in position. However, in areas deposited at high current densities there were indications of



(a)



(b)

Figure 5.5: Image of tungsten clusters. (a) High angle annular dark field image of tungsten clusters using Hitachi HD2000 at 200KeV. (b) Inverted contrast bright field STEM image of tungsten line at 200KeV.

small faceted regions which might be nano-crystalline in nature. These crystallites were only 5 to 10nm is size and are quite small in number shown in figure 5.5 (b). These features may be related to the background nano-particles found on the substrate away from beam irradiated features even though their habit is different to that of the other particles.

Figure 5.6 shows a typical example of a high angle annular dark field (HAADF) Z contrast image of a tungsten line deposited on a thin carbon substrate. The high angle angular dark field (HAADF) signal in the STEM is linearly proportional to the mass thickness - that is to the product of the density (ρ) and the thickness (T) - and to the atomic number (Z). A line profile across a feature therefore provides a cross-section of its thickness profile. This confirms that the profile of a line as shown in figure 5.6 is close to that of a half cylinder, rather than having rectangular faces. The width of lines written with a slow scan speed is of the order of 150nm. This is much larger than the spot size of the electron beam which was less than 20nm in diameter, but Monte Carlo calculations show that the line width is comparable to the beam spreading suffered by the incident 10keV beam within the thin carbon substrate. At a fixed beam energy - here 10keV - and beam current of 2 nanoamps the influence of total dose on the deposition profile when

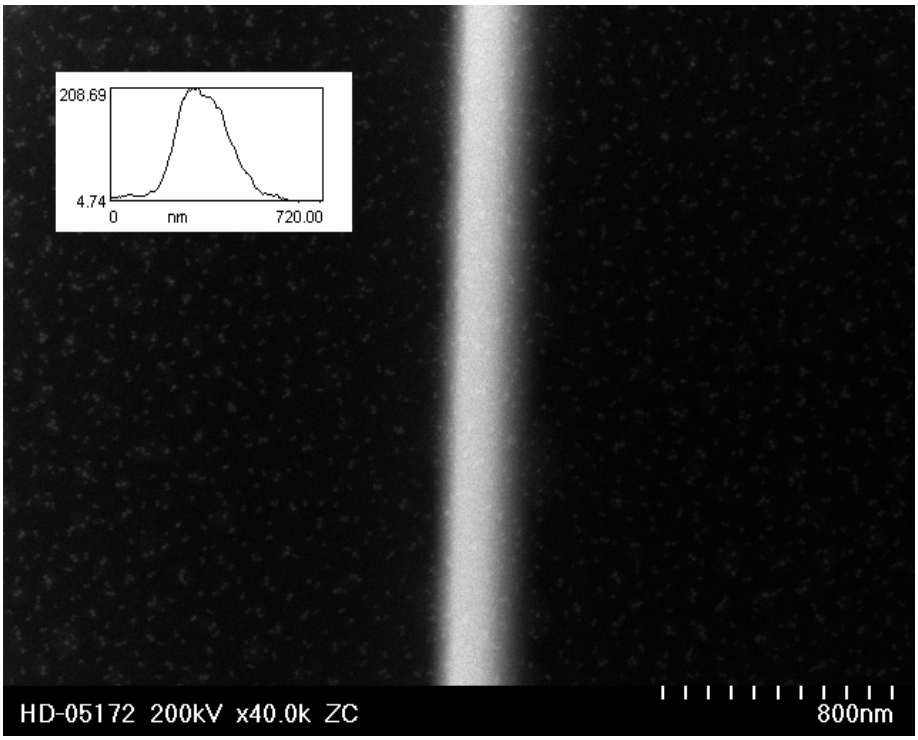


Figure 5.6: High angle annular dark field image of a deposited tungsten line on carbon substrate, showing the line profile.

using $W(CO)_6$ precursor can also be measured from HAADF STEM signals as can be seen in figure 5.6. Backscattered electron line profiles across the lines or squares have intensity proportional to the thickness of the deposited layer. Such profiles in figure 5.7 show that the deposition initially grows quickly but then increases more slowly. The thickness of the lines, and the overall dimensions of the nominally 1 micron by 1 micron squares, however only rises very slowly with exposure. Growth is therefore confined mostly to the vertical direction with little spreading in the lateral plane. The line width is larger than the probe size but smaller than the beam interaction volume.

A plot of the deposition thickness as a function of time, or dose, derived from either X-ray, or other, measurements display a log-linear relationship in our systems for $W(CO)_6$ as shown in figure 5.8. Thus the deposition rate falls as the sample gets thicker. It is assumed that the numbers of adsorbed gas molecules are reducing due to the heat accumulated by energy transfer from the electrons as deposition mechanism procedure. Some other workers in this field have reported a linear growth relationship under conditions similar to ours but the reason for this difference is not yet clear.

It is assumed that the growth of their feature did not reach saturation time and showed the linear behavior. It may be the result of current density in the beam, the presence or

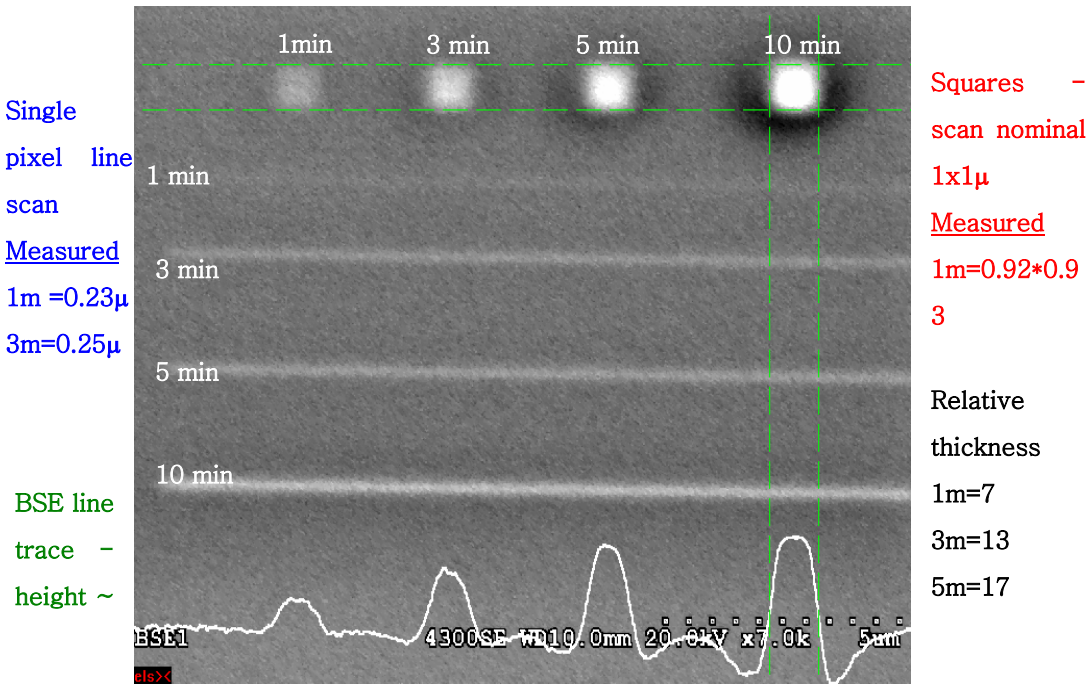


Figure 5.7: Growth at fixed energy (10Kev) and current (2nA) vs time.

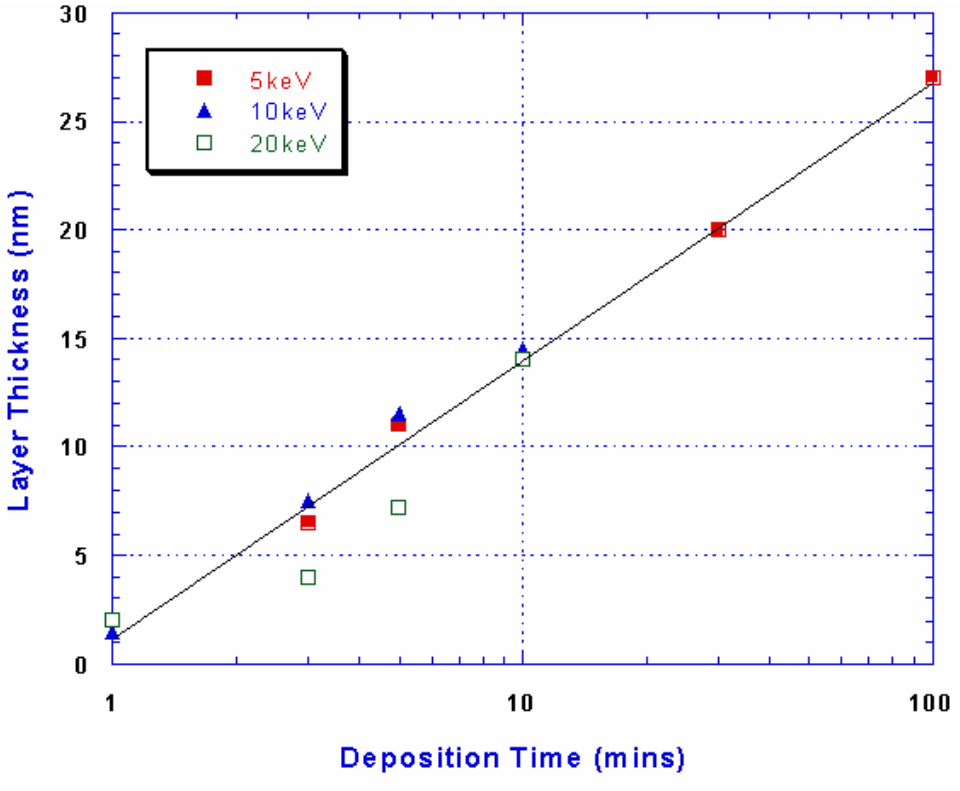


Figure 5.8: Thickness vs deposition time ($W(CO)_6$, at 10Pa with 2nA).

absence of electric fields, or process parameters such as the rate of gas delivery not being totally controlled.

5.4. Role of Secondary Electrons (SE)

When viewed in cross-section at a high tilt angle both line and spot depositions show a characteristically rounded profile. As seen before from figure 5.4 (a) and (b), neither the width of the lines nor the base width of the spots increases with the beam dose, any changes being confined to the vertical direction. This would be consistent with the assumption that growth occurs as a result of secondary electron ionization of the precursor. Secondary electron production will be maximized at the point of beam impact and hence growth will be concentrated in the vertical direction. The width of the lines would be determined by the flux of SE leaving the surface at each point. When this flux becomes too small then growth ceases.

Many of the parameters and quantities needed to build a model describing how secondary electrons produce deposition are not well known or known at all so some guesses have therefore to be made. The usual assumption is that the ionization of the precursor gas will have its maximum probability at relatively low electron energies,

similar to the data (figure 5.9) shown for the impact ionization of hydrocarbons. Because the scattering cross section σ is proportional to inverse of the energy, namely σ~1/E, secondary electrons (SE) which have an energy range of 1~50eV are the first candidates, backscattered secondary electrons (BSE) which have an energy range of 50eV~ are the second candidates and finally the primary electron (PE) with energy of larger than 1 keV is the third candidate, for the electrons which contribute most for the deposition mechanism. If this analysis is correct then secondary electrons would be the species most likely to cause the ionization. We have studied this proposed mechanism by applying a bias to the target substrate as shown in figure 5.10. If SE were indeed the driving force for growth then positively biasing the sample should suppress SE emission and so slow or stop the deposition. On the other hand, if we apply a negative bias to the sample then secondary electrons will be repelled from the target and lead to an enhancement of growth rate.

As seen in figure 5.10, the growth of the pillars was not affected significantly either by positive or negative biasing. Furthermore, changing the bias also had only a negligible effect on whether or not growth of a pillar was vertical. In fact all that is observed as the bias is varied is a small decrease in tip radius and some bending of the growth axis. The

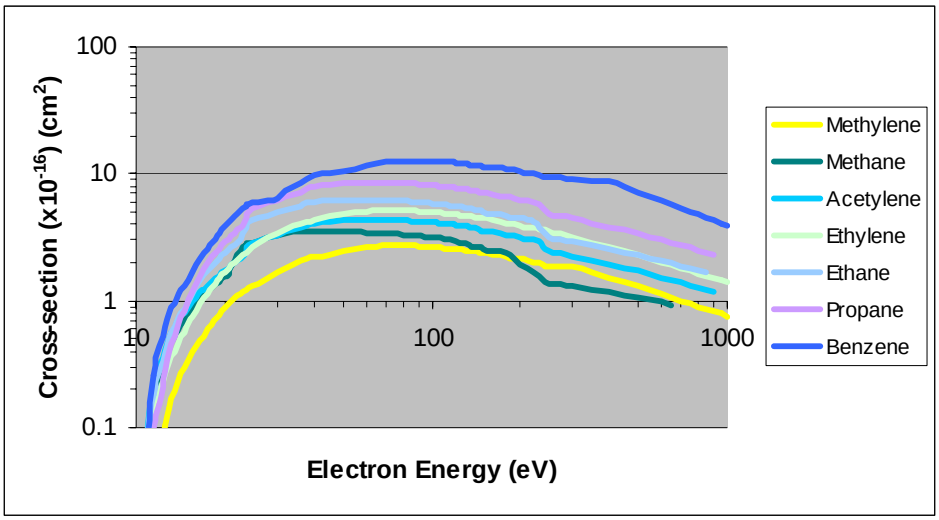


Figure 5.9: Impact ionization data for hydrocarbons.
[http://physics.nist.gov/PhysRefData/Ionization/Xsection.html]

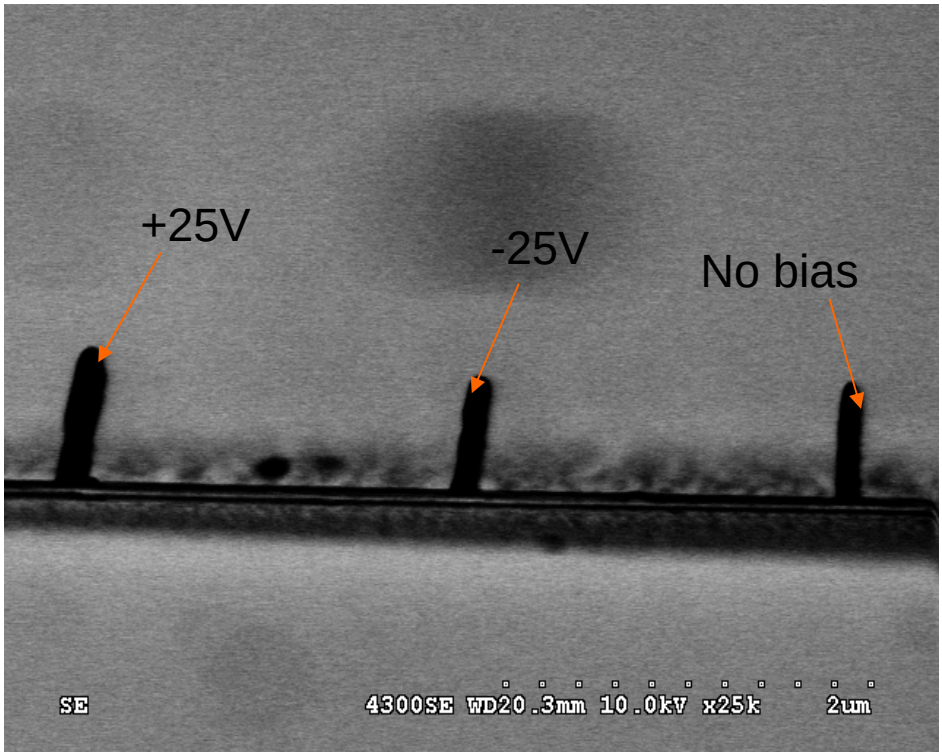


Figure 5.10: Biased by 25volts positive and negative grew for 2min with 1 KeV.

assumption that a positive bias would eliminate SE emission from the surface, and hence stop any growth is not, in practice, correct. Under positive bias SE emission could still continue but the emitted electrons follow the local field lines back to ground potential. In this case the SE image would vanish, but growth stimulated by SE production at the surface would continue. Consequently this experiment does not demonstrate at all whether or not SE are the species most important for the growth of the deposit. In any case it is likely that the other electrons, BSE and PE, must also play a role to the deposition

5.5 Biasing Effect on Box mode Deposition and Etching

The trajectory of SE and BSE which comes out of the surface of the biased substrate with energy of 50eV and 200eV respectively is shown in figure 5.11 We can see that the SE trajectory from the surface recaptured onto the surface again from figure for positive 180V biased trajectories of SE and BSE are all repelled for negatively biased case. This tells that the deposition or the etching be will be affected by the retracted SE and growth or depth profile will vary under different bias condition of the substrate. We can also estimate the deposition rate and etch rate will increase when positive bias is applied to

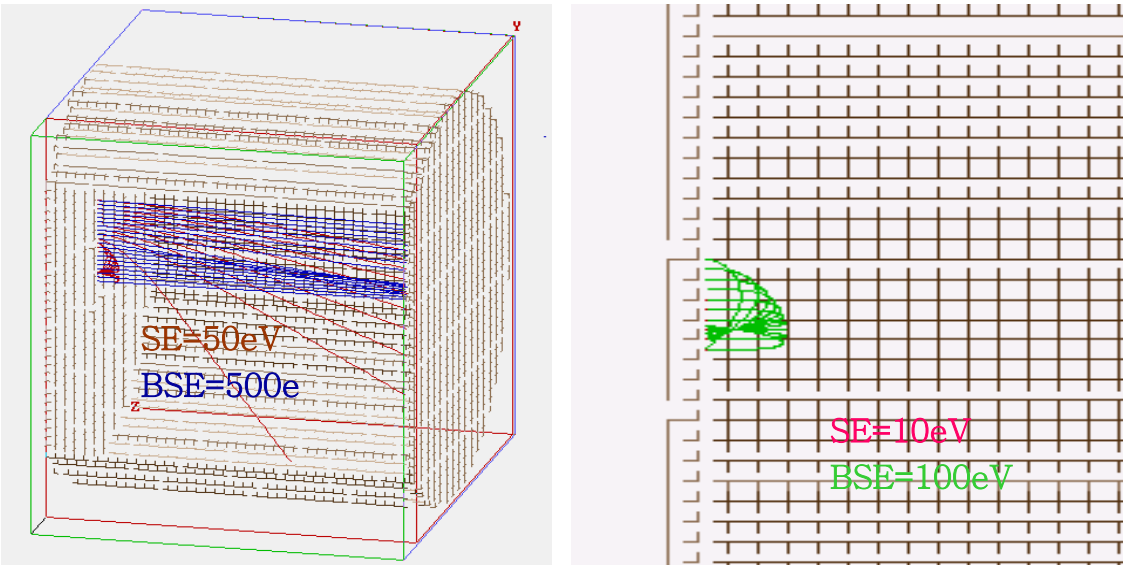
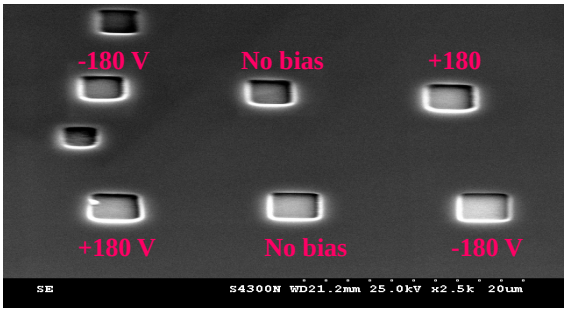


Figure 5.11: Simulation of trajectory of SE and BSE under positive 180 volt of potential applied on 1x1cm^2 box in SEM with two different emission energies.

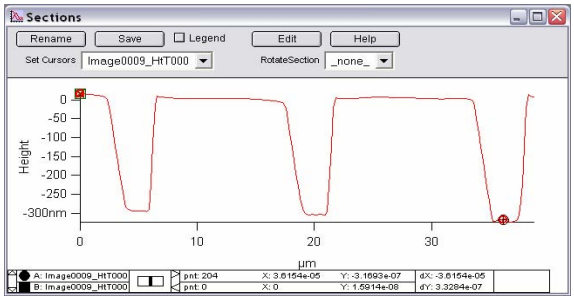
the substrate compare to the no bias case and positive bias will decrease deposition or no change in rate compared to no biased case.

As seen in figure 5.12, etching profile is showing that deeper etching when positive 180V was applied than no bias with 90nm and 50nm respectively. For the negatively 180V biasing is showing that the depth with about 20nm and 50nm less than that of no biased etching. The reason for two different etching with opposite sequence of biasing from the injection needle is to distinguish whether it is the effect of pressure or the effect of given bias. From the figure 5.12 (b), (c) the etched depth changes with the relative bias and this means that the difference of the depth profile is due to the bias not by the gas pressure.

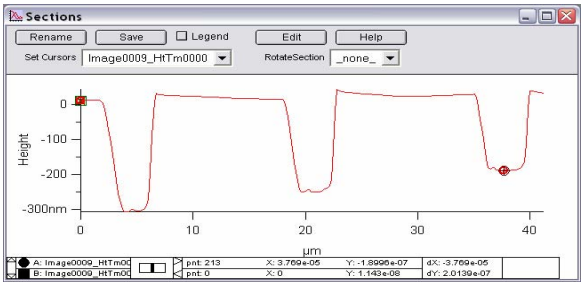
The tungsten deposition of the box also been carried out under different bias as seen in figure 5.13 with same bias as etching. It is showing that growth of the box under the positively 180 biasing is about 30nm higher than that of no biasing and about 20nm less in case of negatively bias from the AFM scan as seen in figure. From the etching and deposition experiments, etching under the bias is showing distinctive variation than deposition under bias. The reason for this seems to be the affect of the SE from the side wall of the front of etching site. During the etching with positively biased, SE or BSE



(a)

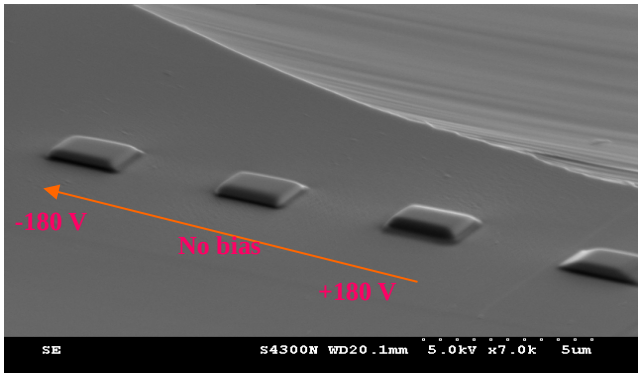


(b)

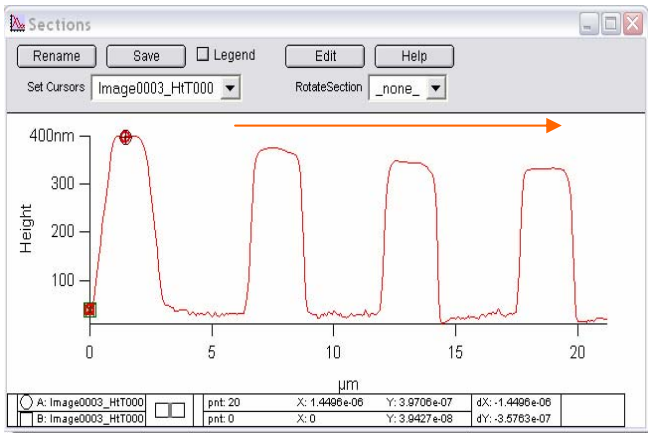


(c)

Figure 5.12: Biased by three different biases in box mode. (a) 4x4µm^2 box etching with -180 volt, no bias, and +180 volts with 5KeV for 1minute. (b) Depth profile measured with AFM of upper three. (c) AFM of bottom three.



(a)



(b)

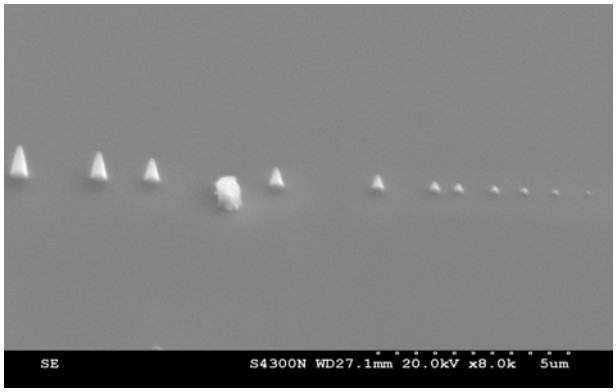
Figure 5.13: Biased by three different biases in box mode. (a) 4x4µm^2 box deposition with -180 volt, no bias, and +180 volts with 5KeV for 30minutes. (b) Depth profile measured with AFM of upper three.

generated from the surface will hit the front side wall of etched site and will generate SE or BSE. Therefore the number of recaptured SE and BSE in etching with positively biased is higher than that of deposition under no biased and negatively biased etching.

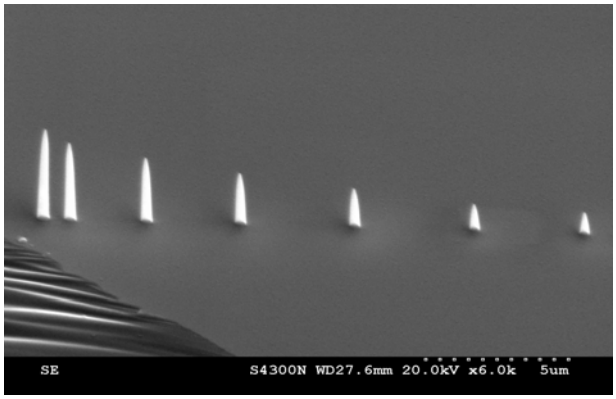
5.6 Pressure Effect

Figure 5.14 and 5.15 show SEM images of deposits of SiOx and tungsten from TEOS and WF_6 precursors respectively, at three different chamber pressures. From high resolution imaging of each fiber (figure 5.14 and 5.15), the heights and widths of each nanofiber were measured (figure 5.16 and 5.17) and the total volume was calculated (figure 5.18). Figure 5.16 illustrates that the height of the fibers increases with growth time and with increasing precursor pressure.

In general, the growth rate of the TEOS fibers is ~2x faster than WF_6 at the same measured background pressure. While the growth rate is known to saturate due to electron beam heating [98], the fall-off in the WF_6 fiber growth rate for the $8x10^{-3}$ Pa pressure after 300 seconds is believed to be due to fluctuations in the WF_6 pressure during growth.



(a)



(b)



(c)

Fig. 5.14. Growth with TEOS Precursor gas with the pressure of (a) $1x10^{-6}$Pa (b) $3x10^{-6}$ Pa (c) $8x10^{-6}$Pa

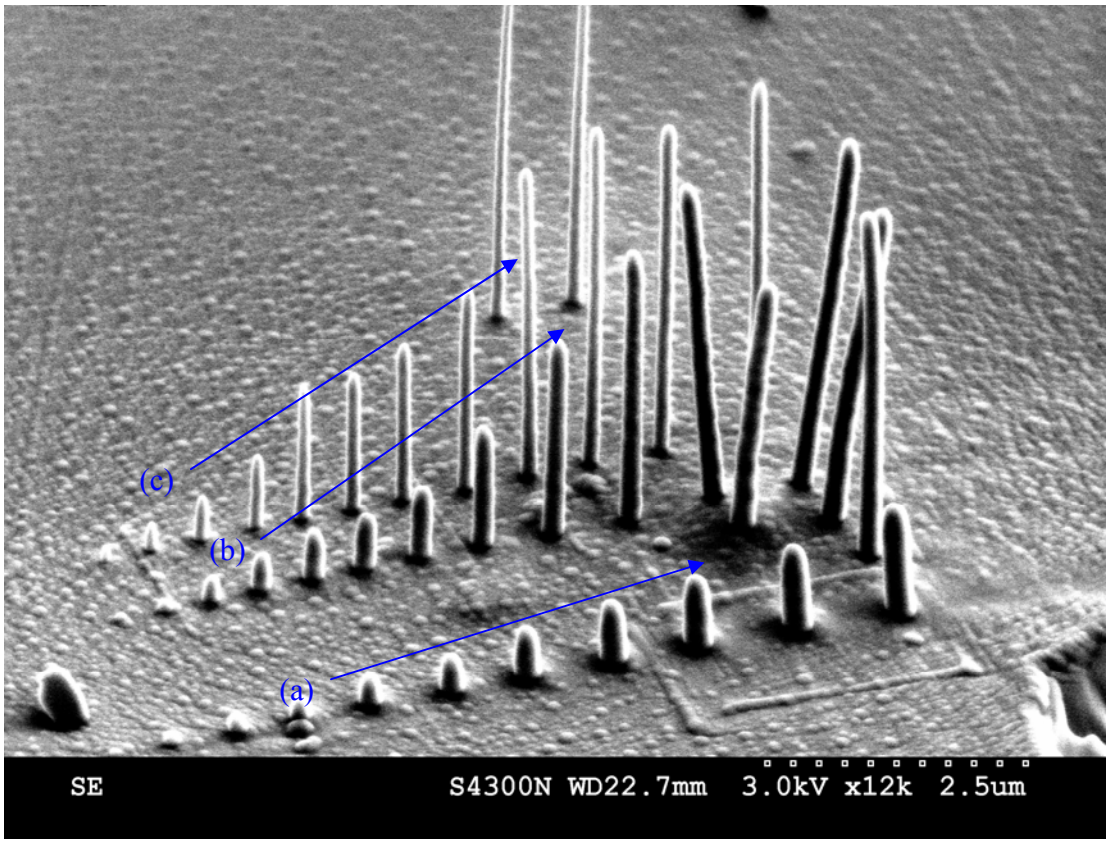
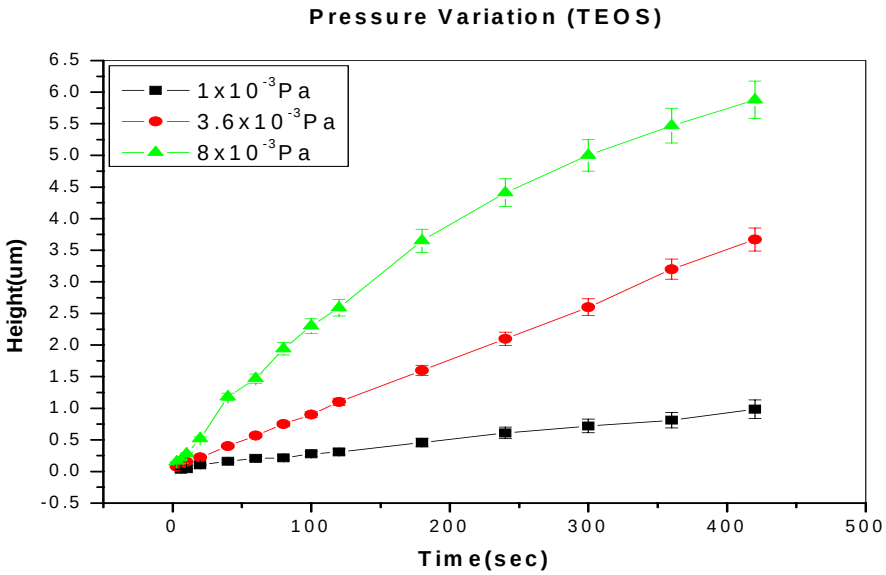
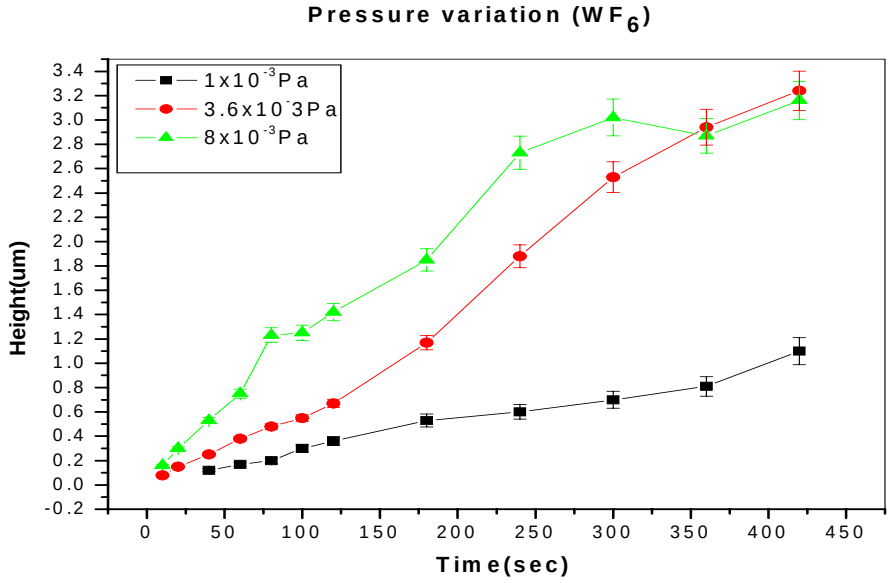


Figure 5.15: Growth with WF_6 precursor gas with the pressure of (a) $1x10^{-6}$Pa (b) $3x10^{-6}$ Pa (c) $8x10^{-6}$Pa.

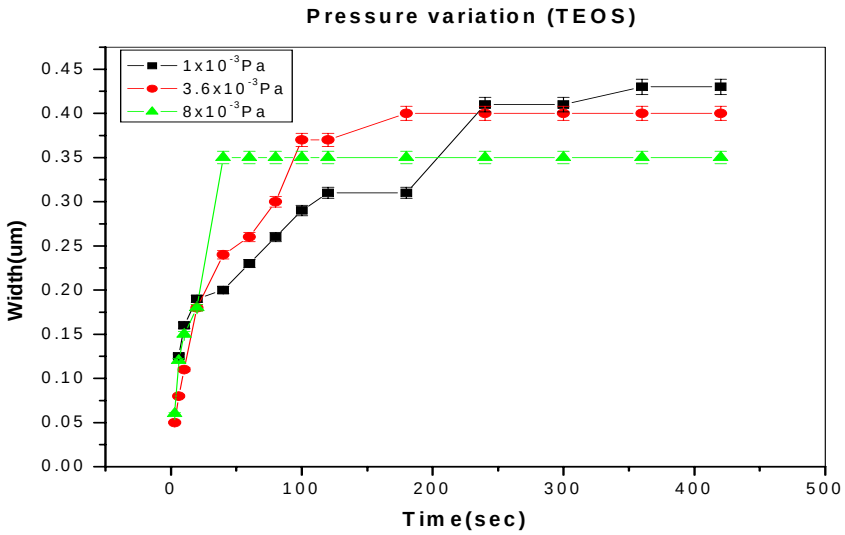


(a)

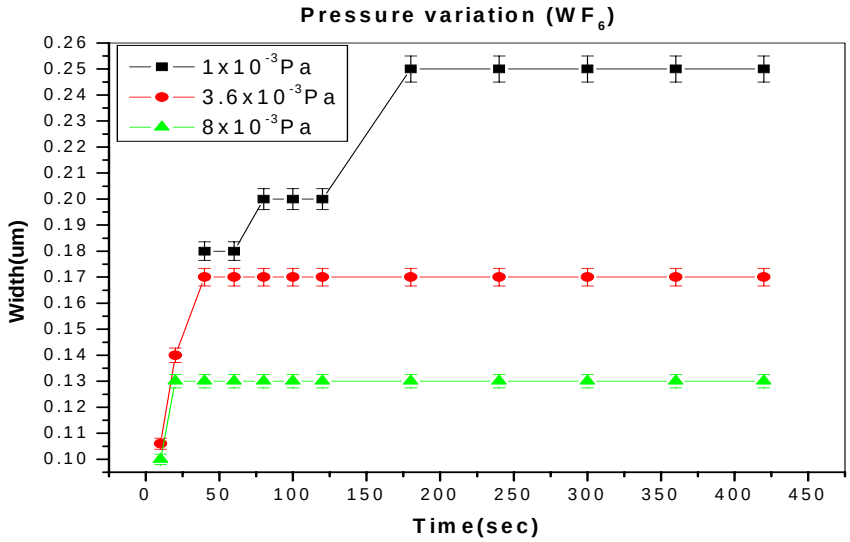


(b)

Figure 5.16: Heights of nano pillar deposits of
(a) SiOx and (b) W

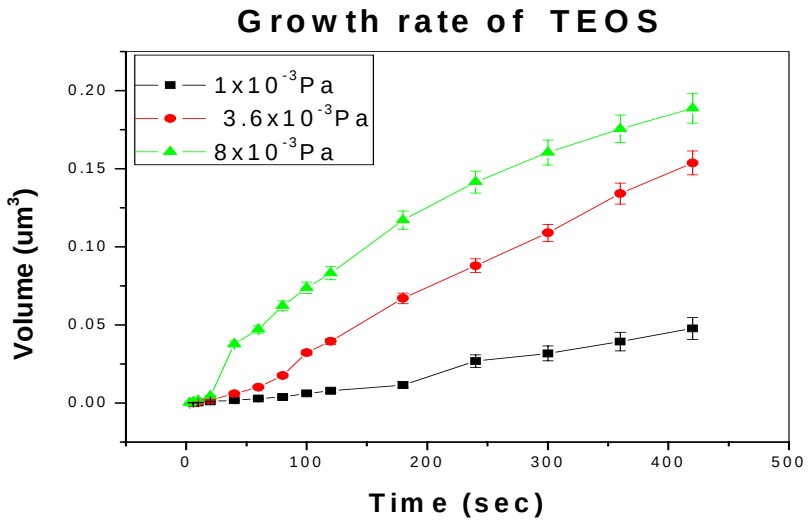


(a)

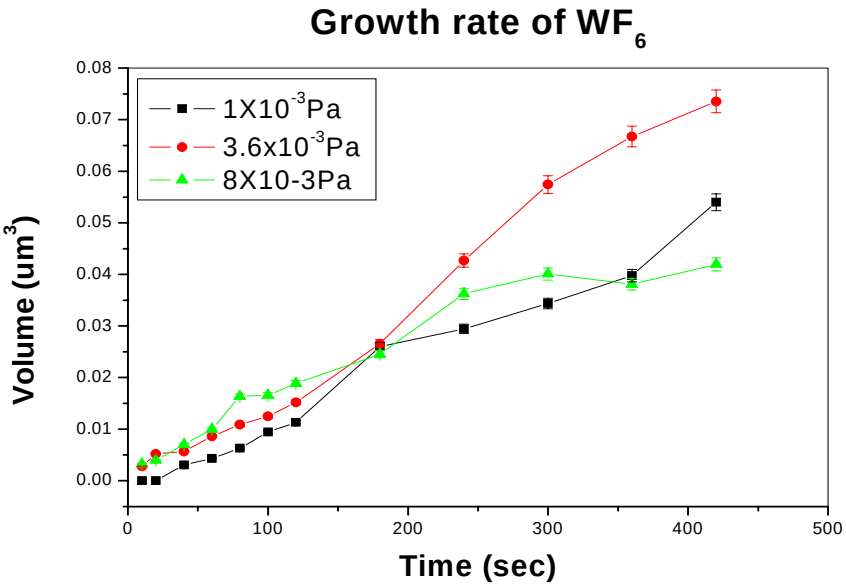


(b)

Fig. 5.17: Width of nano pillar deposits of
(a) SiOx and (b) W



(a)

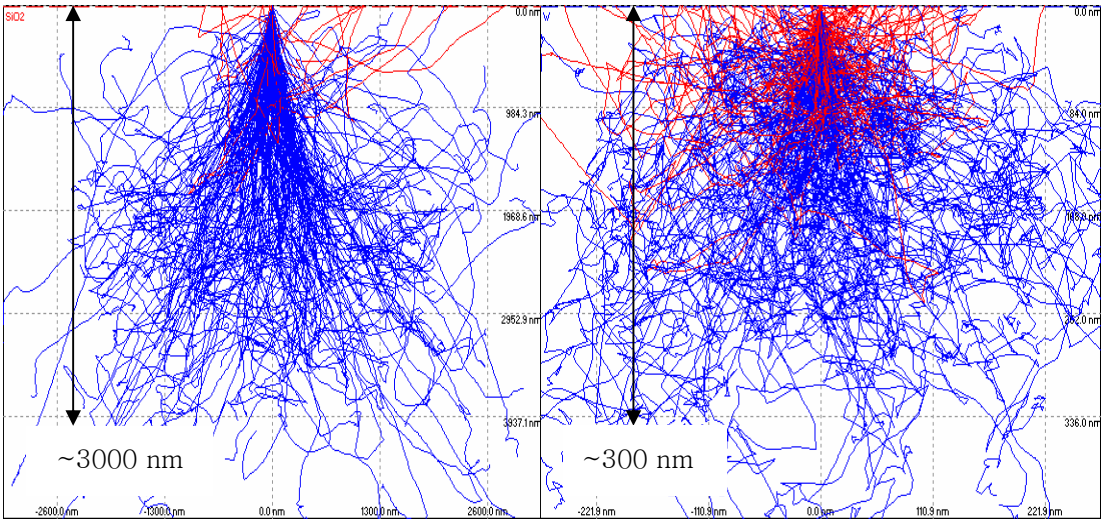


(b)

Figure 5.18: Growth rates of nano pillar deposits of (a) SiOx and (b) W by calculation

From the figure 5.14, growth of SiOx used by TEOS precursor shows cone shape growth and, as the pressure becomes higher, the end radius of the deposits get smaller. From the figure 5.15, growth of the tungsten used by tungsten hexafluoride (WF_6) shows an almost cylindrical growth habit and as pressure gets higher the end radius of the deposits also gets smaller and saturates at lower times. This difference in shape between the two materials can be understood in relation to the beam interaction volume. The shape of interaction volume depends on the electron beam energy and the deposited target material.

Figure 5.19 shows the interaction volume plots of electrons at 20keV from Monte Carlo simulations, which demonstrate that the interaction volume of SiO_x is much larger than W at the same energy. The electron range depends inversely on the density of the material and so the interaction volume in W (ρ=19250/kg-m^{-3}) is much smaller than that in SiO_2 (ρ=2330/kg-m^{-3}). We can estimate the electron inelastic scattering range with the density of the material using Kanaya-Okayama Range formula given in equation (5.1). The calculated ranges were $R_{ko}(W)$ = 851nm and $R_{ko}(SiO_2)$ = 4720nm for tungsten and SiO_2 bulk sample, respectively.



(a) (b)

Figure 5.19: Monte-Carlo simulation of interaction volume with the beam energy of 20KeV for bulk substrate. (a) SiO_2, (b) Tungsten.

$$R_{ko} = (0.0276AE_0^{1.67})/Z^{0.89}\rho \qquad (5.1)$$

The depth of the interaction volume for SiO_x is about 3μm and about 300nm for W from the simulation. The pillar morphology is related to the effective interaction volume in the nanopillar. Shallow interaction volumes lead to the production of cylindrical shapes and while larger interaction volumes lead to more conical structures. As the effective interaction volume approaches the pillar height, a cylinder is formed. From figure 5.14 and 5.16, it is seen that in the deposition of SiO_x at a gas pressure of $1x10^{-3}$Pa the interaction volume is not reaching the height of 3μm therefore the shape remains as cone type. With the pressure of $3.6x10^{-3}$Pa and $8x10^{-3}$Pa, it is seen that 3μm height is achieved at ~330 seconds and ~120 seconds respectively. We can see that the shape of the SiO_x deposit at the base is changing from conical to cylindrical around these time regime with the pressure. This indicates that it is scattered electrons in the interaction volume that defines the shape of short time regime deposits until interaction volume emerges from the substrate and the shape of top end of the pillar.

Figure 5.17 plots the fiber diameter as a function of precursor pressure and growth time for WF_6 and TEOS grown fibers. From figure 5.17, one notes that the fiber diameter

saturates at different times and values as a function of precursor pressure. One important observation is that while the pillar diameters change with pressure, the point at which they saturate for tungsten and SiOx occur at similar heights for both materials. For instance deposition of SiO_x saturates at a height of around 1μm for all pressure and deposition of tungsten saturates at around 0.3μm for medium and high pressures, and 0.5μm for low pressure. This shows that the lateral growth saturates at a similar height in three different pressures. We can assume that the effective interaction volume is completely in the nanofiber and the scattered electrons confined in the interaction volume limit the lateral growth.

As seen in figure 5.16, the vertical growth of SiOx is proportional to the pressure of TEOS and WF_6 and the growth behavior is similar to that reported previously [17] [32] [20] [50] [98]. The plots show linear growth for lower times and the overall growth rate at low times are proportional to the growth pressure; at low pressure the rate is 2.3nm/sec, at medium pressure the rate is 8.6nm/sec and at high pressure the growth rate is 21.6nm/sec For the high pressure, the growth rate reduces after 3 minutes from 21.6nm/sec to about 10.1nm/sec. It is suspected that at these long growth times, there is a reduction in the surface population of gas molecule due to electron-beam-induced

heating (EBIH) as described by Randolph *et al*. [98]. Figure 5.16 (b) shows the growth rate of the tungsten nanofibers from WF_6. From figure 5.16, the growth rate is proportional to the WF_6 pressure; at low pressure the growth rate is 2.6nm/sec, at medium pressure the growth rate fluctuated but had an average growth rate of 8.2nm/sec, and at high pressure the growth rate is 9.6nm/sec.

When the heights of the pillars are compared the lateral growth saturation begins for the SiOx pillar height the width saturate at around 1μm and for the W pillar the height that the width saturates is around 0.3μm.

Monte-Carlo simulations of the interaction volumes in the pillar based on the material and diameter from the experiment were performed and compared with the tip of the deposits as shown in figure 5.20 and 5.21. The conditions for the simulations are 20 KeV beam energy, 1000nm of the fiber height, and use of 3000 electrons. The result shows 797nm and 723nm as the average final axial position for SiOx deposits and careful measurement of real deposits show that the tip curvature start around 590nm and 470nm with the width of 400nm and 350nm. For tungsten deposits, the average axial positions

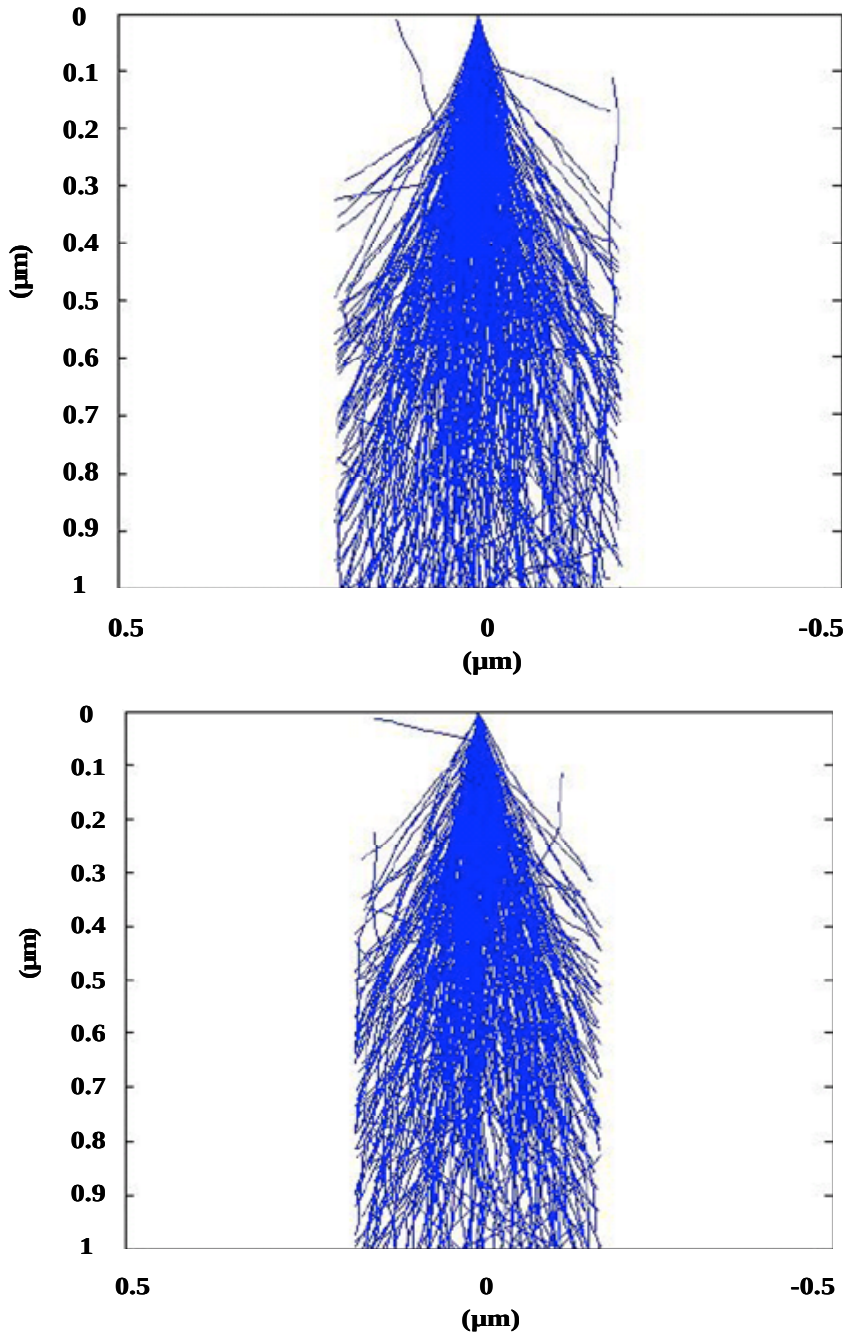


Figure 5.20: Monte-Carlo Simulations of the effective interaction volumes in the pillars with 20 keV beam energy: (a) 400nm in diameter and 350nm in diameter for SiO_2 fibers.

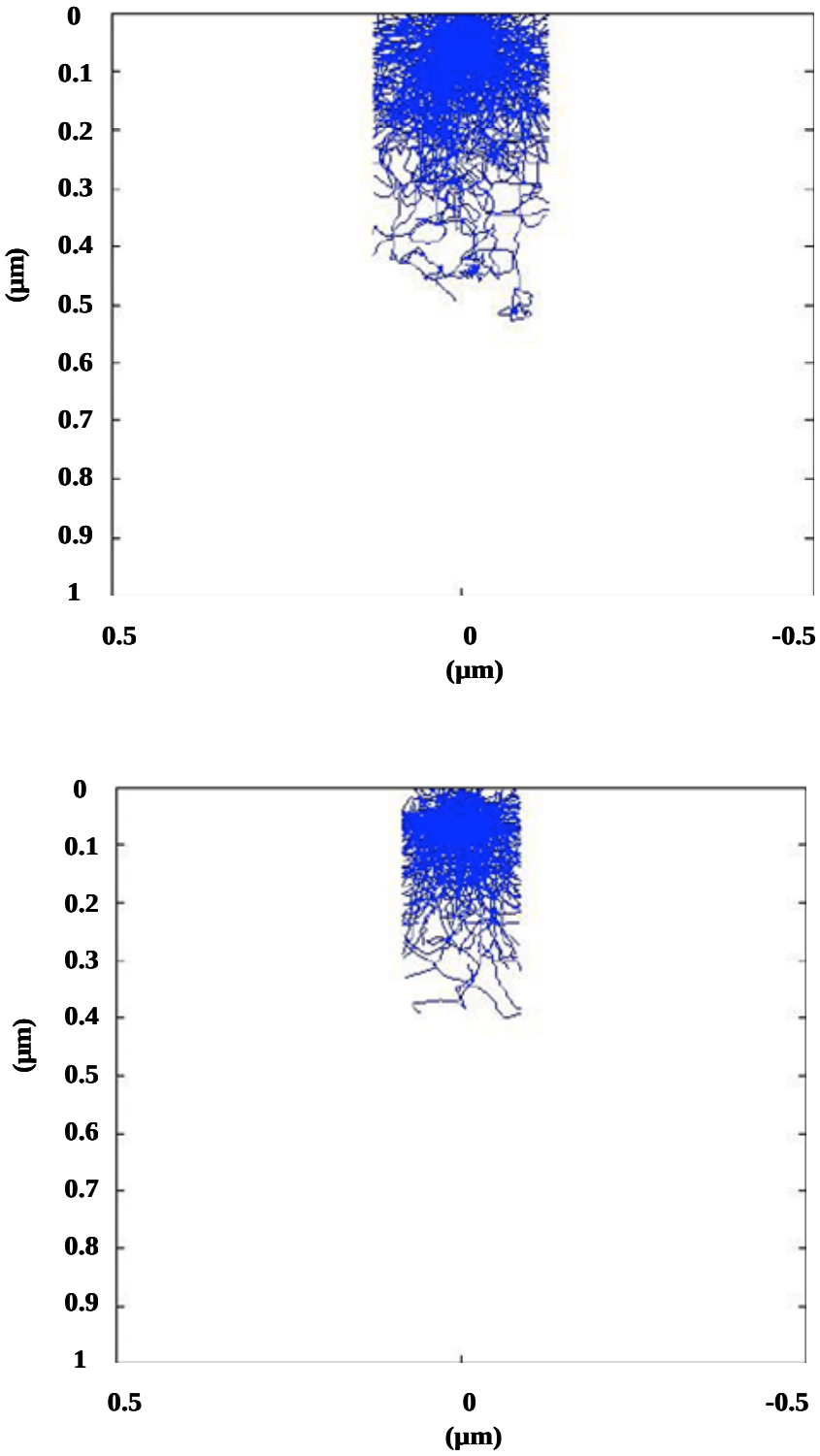


Figure 5.20: continued.

(b) 250nm, 170nm in diameter for tungsten fiber.

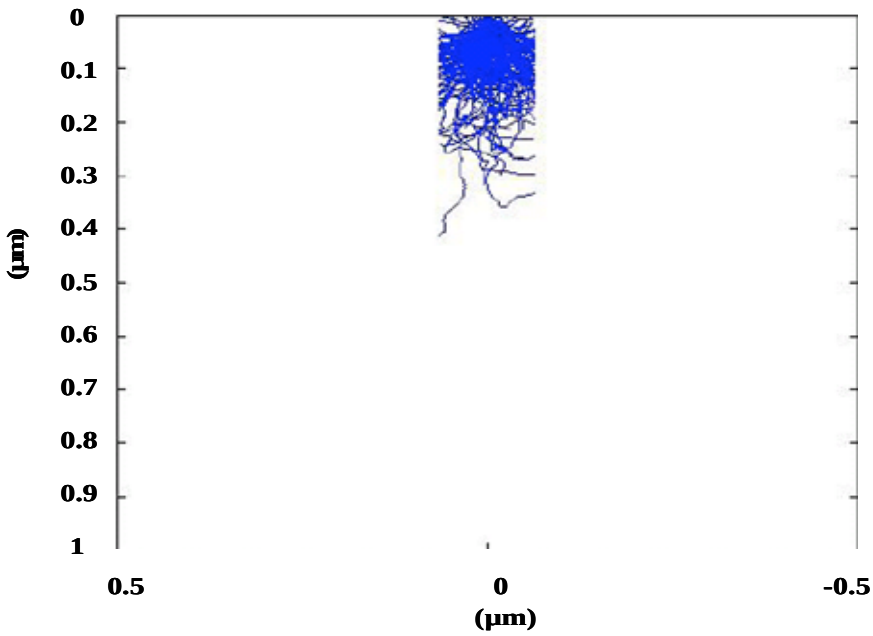
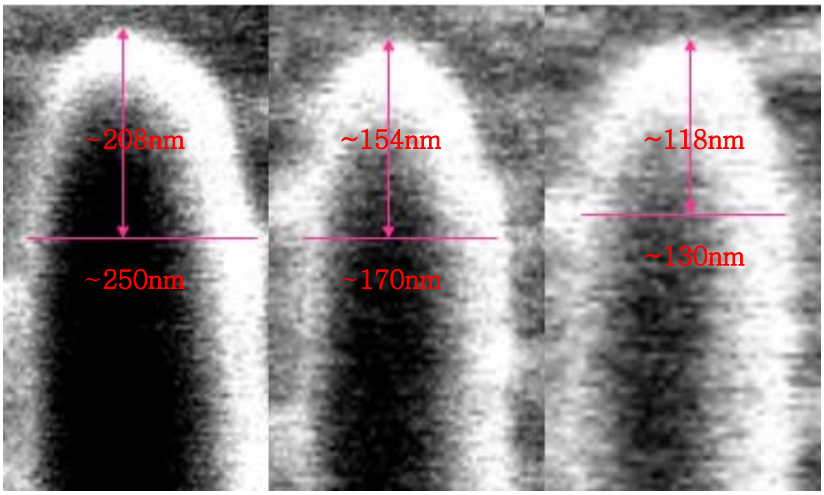
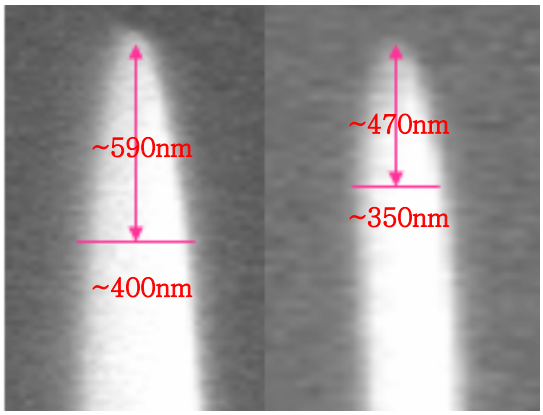


Figure 5.20: continued.
(b) 130nm in diameter for tungsten fiber



(a) (b) (c)

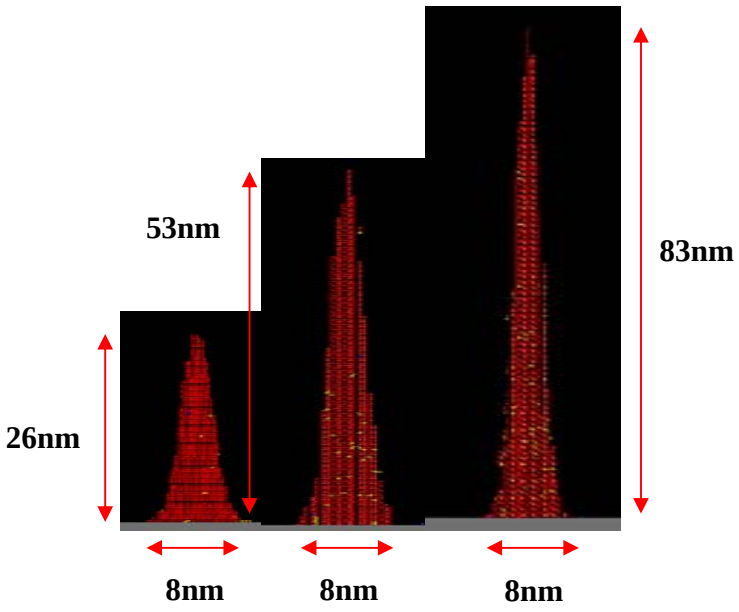


(d) (e)

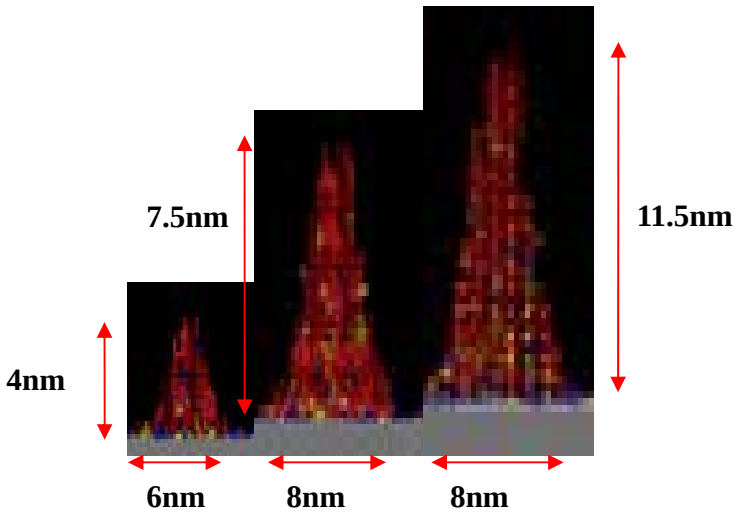
Figure 5. 21: Measurement of the top curvature height of the pillar for each pressure with (a) $1x10^{-3}$Pa (b) $3.6x10^{-3}$Pa (c) $8x10^{-3}$Pa for tungsten and (d) $3.6x10^{-3}$Pa (e) $8x10^{-3}$Pa for SiOx EBID deposits.

of the pillars are 116nm, 102nm, and 95nm, the height of real deposits are 208nm, 154nm, and 118nm with the width of 250nm, 170nm, and 130nm. The simulation shows that the interaction volume in the pillar defines the shape of the pillar tip and is in good agreement with the both materials even with the small number of the electrons. This confirms that the interaction volume in the pillar is shorter than that in bulk materials because the pillar cannot confine the interaction as occurs in the bulk material.

Figure 5.22 shows the simulated growth of a cylinder from the substrate using 900,000 electrons, resulting in 8nm high growth. This is too small a dose to grow the pillar to a height at which lateral growth has saturated, but carrying on the simulation to this level would have required excessive computing time. The growth behavior of SiOx is predicted to be linear as is found experimentally, but for tungsten deposition, it also shows as similar growth behavior up to about 12nm as shown in figure 5.22 (c). To help save time the pressures used for the simulations were 40Pa for SiOx and 120Pa for tungsten deposition, values which are about 1000 times higher than those used experimentally. The comparison of the height of the simulation and experiment differ by a factor of about 100 times and this reflects the difference in electron dose. The value of this simulation is that we can determine what type of electrons (e.g. SE (secondary

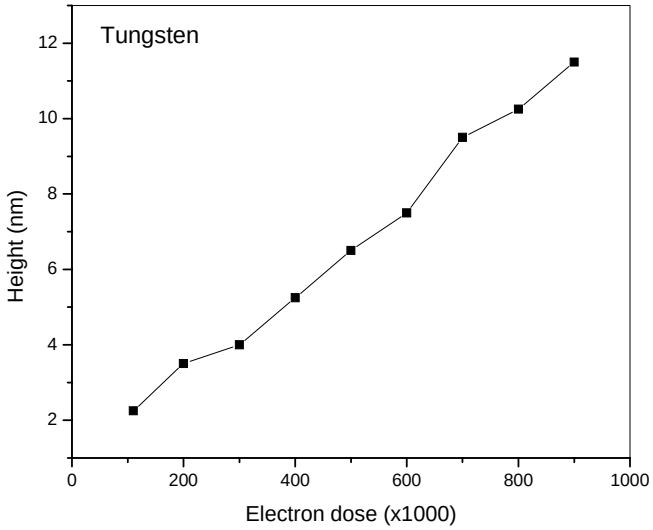


(a)



(b)

Figure 5.22: Three-dimensional simulations of the electron beam induced deposition with (a) TEOS precursor gas with the pressure of 40Pa with electron does of 300K, 600K, and 900K. (b) WF_6 precursor gas with the pressure of 120Pa. with electron dose of 300K, 600K, and 900K.



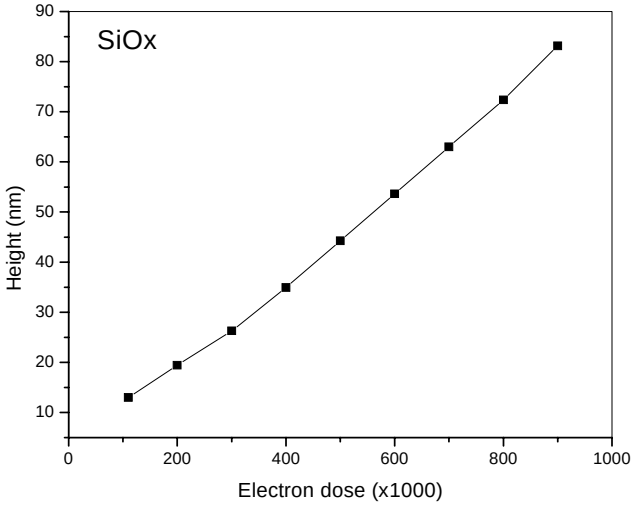


Figure 5. 22: continued (c) Simulated growth rate of SiOx and tungsten EBID process with electron dose for simulation is up to 900K with the pressure of (40 Pa).

electron), BSE (backscattered electron), FSE (forward scattered electron), and PE (primary electron)) will contribute to the deposition mechanism.

These experiments show that the interaction volume of the electron plays a critical role in defining the width and shape of the pillars grown by electron beam induced deposition. The interaction volume in the substrate is related with the width of the pillar and interaction volume in the pillar (effective interaction volume) is related with the tip shape. From a comparison with the simulation, we could possibly estimate the pillar sizes and tip shape for the further deposition with variable beam conditions, materials, and pressure with the simulation.

5.7 Effect of Scan Speed of SEM

The scan speed is important for determining the size of deposited feature. From figures 5.23 (a) and (b), the channels from deposited at the faster scan mode (TV1) to slow scan mode (SLOW2), show that the line width is changing about 0.02 μm from TV1 to TV2, 0.03 μm from TV2 to SLOW1 and about 0.5 μm from SLOW1 to SLOW2 scan mode. As mentioned from the chapter 4 in figure 4.9, the large deposition occurs at the beginning of the line deposition at the position where the beam dwells after flyback.

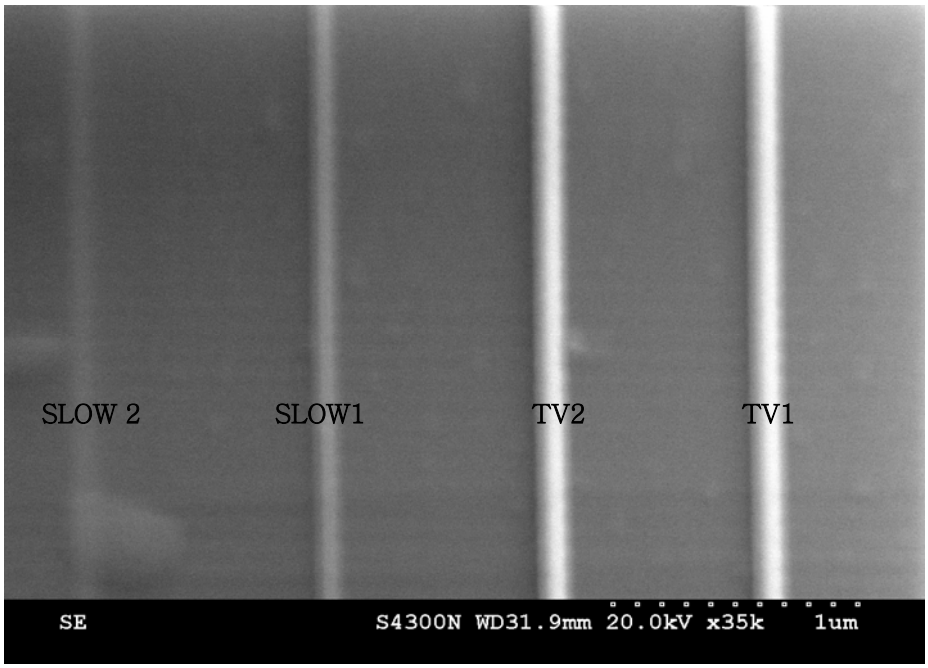


Figure 5.23: Different scan modes deposition: (a) line depositions of tungsten with four different scan modes (TV1, TV2, SLOW1, SLOW2).

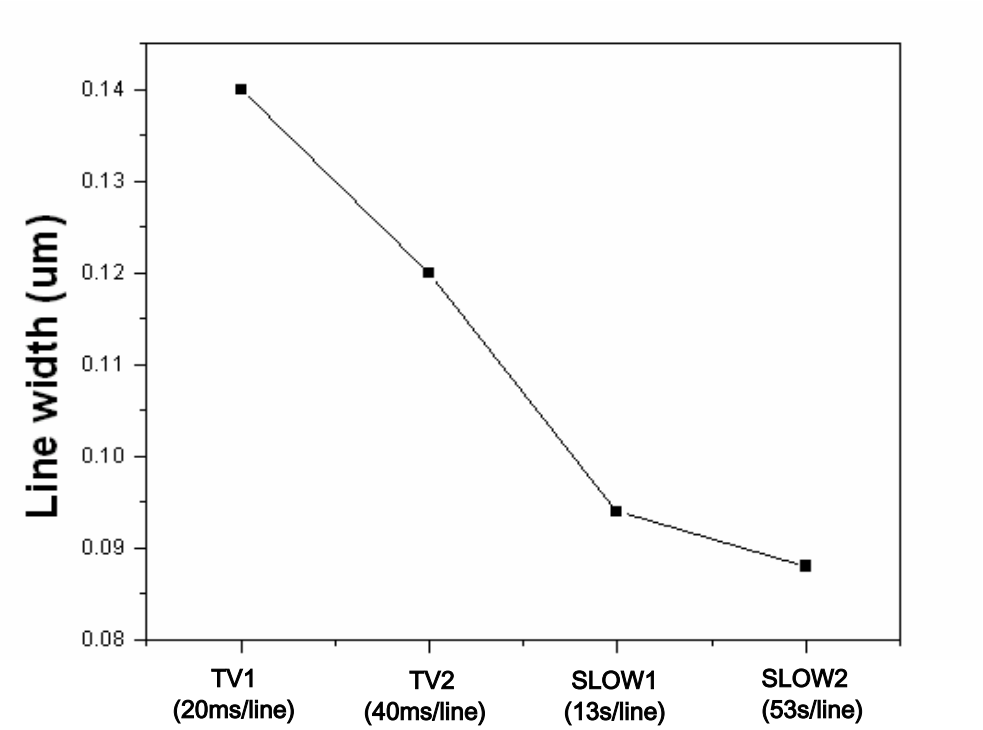


Figure 5.23: Continued

(b) Line width variation due to the scan modes of the SEM.

This variation is possibly due to the supply rate of the gas on the injector line after each scan. For a faster scan rate such as TV2, the precursor gas will supply enough precursor molecules on each scan to deposit on the line. But for slow scan rates such as SLOW1, the line becomes thinner and narrower than for the TV2 rate because the gas flux is insufficient to continuously support the initial growth rate. For the accurate feature size deposition, optimizing of the scan mode speed and gas supply seems to be necessary. The electron dose deposited on a line for 2 minutes can be calculated as 3.2μC (TV), 1.63μC (SLOW 1), 1.62μC (SLOW 2). This shows that the electron dose deposition required for the TV mode is larger than that required for SLOW but not a big difference for SLOW1 and SLOW 2 mode as the experiment.

CHAPTER 6

PRACTICAL APPLICATIONS

6.1 Mask Repair

The benefits of easy manipulation, controlled deposition, and selective etching provided by the technique of EBID are potentially of importance for application to the semiconductor and nanotechnology industries. Possible uses of EBID are mask editing and repair, mask fabrication, IC modification and chip repair, the production of nano-tips for scanning tunneling microscope (STM), and atomic forced microscopy (AFM), field emitter sources, electrical contacts for nano-bio applications, 3D nanostructures, and more. In this section work on mask repair for chrome and quartz (Cr/Qtz) binary mask and multi-layered extreme-ultraviolet (EUV) mask using EBID will be described.

6.1.1 A Brief Explanation of Mask Repair

Photolithographic masks are used for patterning features on circuits and their principle is illustrated in figure 6.1. Descriptions of the types of masks commonly used commercially are:

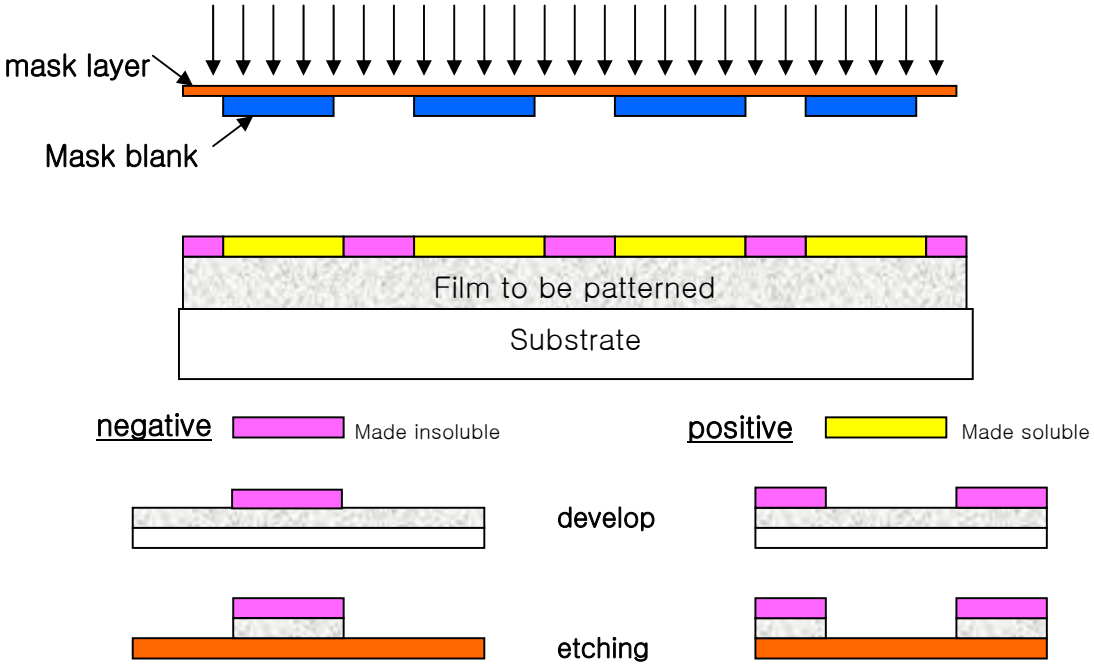


Figure 6.1: Brief schematic explanation of mask and pattern develop.

• Chrome Masks. (Binary Chrome on Quartz)

The 5 or 6-inch chrome on quartz photo mask is still the most commonly used. This mask is suitable for both visible and UV radiation and can fabricate features down to about 150nm. There are potentially two types of defects, opaque and clear in such masks. Clear defects are areas where the chrome is missing and must be replaced. Opaque defects are regions which are supposed to be clear, but which have chrome on other materials on them that must be removed. Critical repair issues for chrome photo-masks include charge neutralization, edge placement accuracy, quartz damage, and transmission after repair.

• Phase Shift Masks (PSM).

Chipmakers have strong economic incentives to try to extend stepper operation beyond their present resolution limits which are set by the Abbé diffraction limit. One current approach employs phase-shifting of the illuminating light in the exposure tool to cause destructive interference at the wafer plane. The “null” from such a destructive interference can be made arbitrarily narrow so allowing the tools to print smaller features. Many types of phase shift masks have been proposed but the most popular type today is

the embedded shifter or halftone mask, in which a semitransparent film is employed to simultaneously reflect and phase shift the illumination.

A typical example of an embedded shifter mask is one using molybdenum silicon oxy-nitride (MoSiON) as the absorbing material instead of chrome. MoSiON transmits a small percentage of the light and also shifts the phase of transmitted light by 180 degrees. This phase-shift technique is not as powerful as some others, but is the simplest to design, write, inspect, and repair.

• Optical Proximity Correction (OPC) masks

OPC is used to improve print results by distorting or modifying features on binary or phase-shift masks in an attempt to compensate for error caused by proximity effects. Usually OPC adds serifs to the ends of lines and shape distortions in critical areas where adjacent lines come close to each other. These OPC features are, in practice, optimized empirically and so during the early stages of developing a mask it is frequently necessary to change details of the OPC. The use of EBID greatly facilitates this effort. Otherwise OPC techniques do not create any major changes in the way these masks are repaired.

• EUV Multilayer mask

EUV Lithography is a projection technique using a reducing optical system (4X) and employing illumination in the soft X-ray regime (10-20nm). Reflectivity at EUV wavelengths is obtained by coating the photomask substrate with metal or compound multilayers. The usual photomask blank consists of a silicon wafer substrate coated with 40 pairs of Mo and Si layers with thicknesses of 3nm to 4nm. This multilayer (or ML) is designed to maximize reflectivity at a wavelength of 13.4nm. Typically, two types of defects are encountered on ML masks; the presence of metal where none is required (opaque defects) or the absence of metal where it is needed (clear defects). For opaque defects; it is necessary to remove excess material by etching and for clear defects; it is necessary to deposit material to reconstruct the desired pattern.

6.2 Repair of Binary and EUV ML Mask

The techniques discussed earlier have been applied to the repair of chrome on quartz binary masks. The first step is to clean the area by etching around the edge of the defect area in the original pattern with XeF_2 using the SEM in variable pressure operating mode at 25Pa chamber pressure. The conditions typically employed for this etching were beam

energy-20KeV, magnification-25000x for line mode and 90000x for spot mode, beam current measured as specimen current-1.65nA, beam irradiation time for spot-2 minutes and for line-5 minutes using the “slow 2” (2sec/line scan) scan mode. The repair was then completed by performing EBID at the area which had previously been etched away. All the conditions were the same except for the beam current which was increased to 4.14nA and the exposure time which was changed to 10 seconds.

As shown in figure 6.2, after completion of the process the repaired area does not show well defined edges and the variation in the BSE image brightness for both spots and lines suggests that the thickness of the repair exceeds that of the original material. This may be the result of many factors such as different growth rates at the cleaned edges of the original pattern, charging of the quartz substrate by the incident electron beam, beam shifts which occur as a result of the charging, and the irregularity of the shape of defect. Similarly it was also found that the end of the repaired line was always brighter in the image than elsewhere, again implying thicker deposition at that point, probably because the scanned beam dwells longer at the start of each raster as shown in figure 6.2.

As a second example a repair of a TaBN//Mo-Si ML/Si EUV as shown in figure 6.3 (patterned with 70nm TaBN on 80 of multi-layers made with 40nm thickness of Mo and

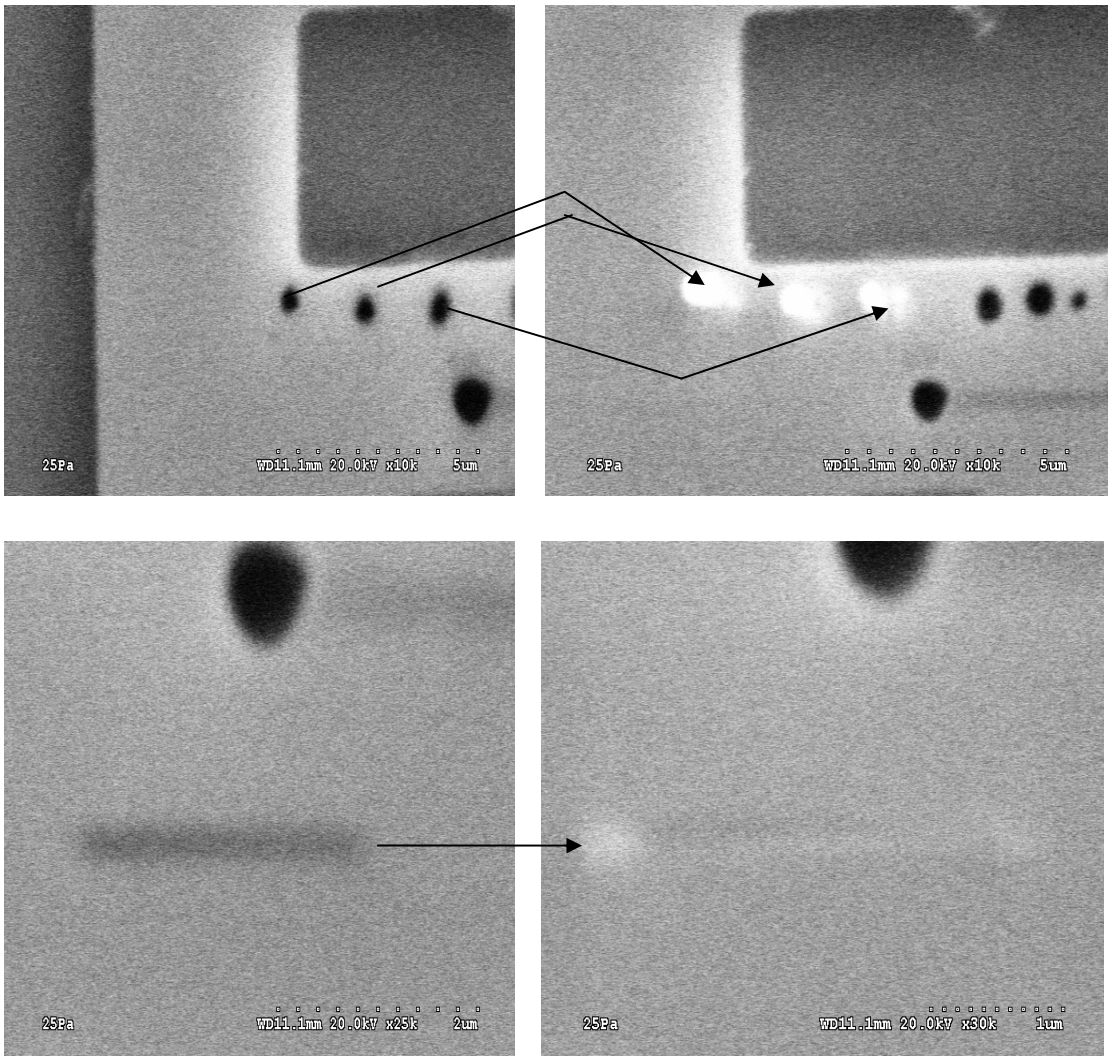


Figure 6.2: Clear defect repair of Cr/Qtz binary mask using EBID.

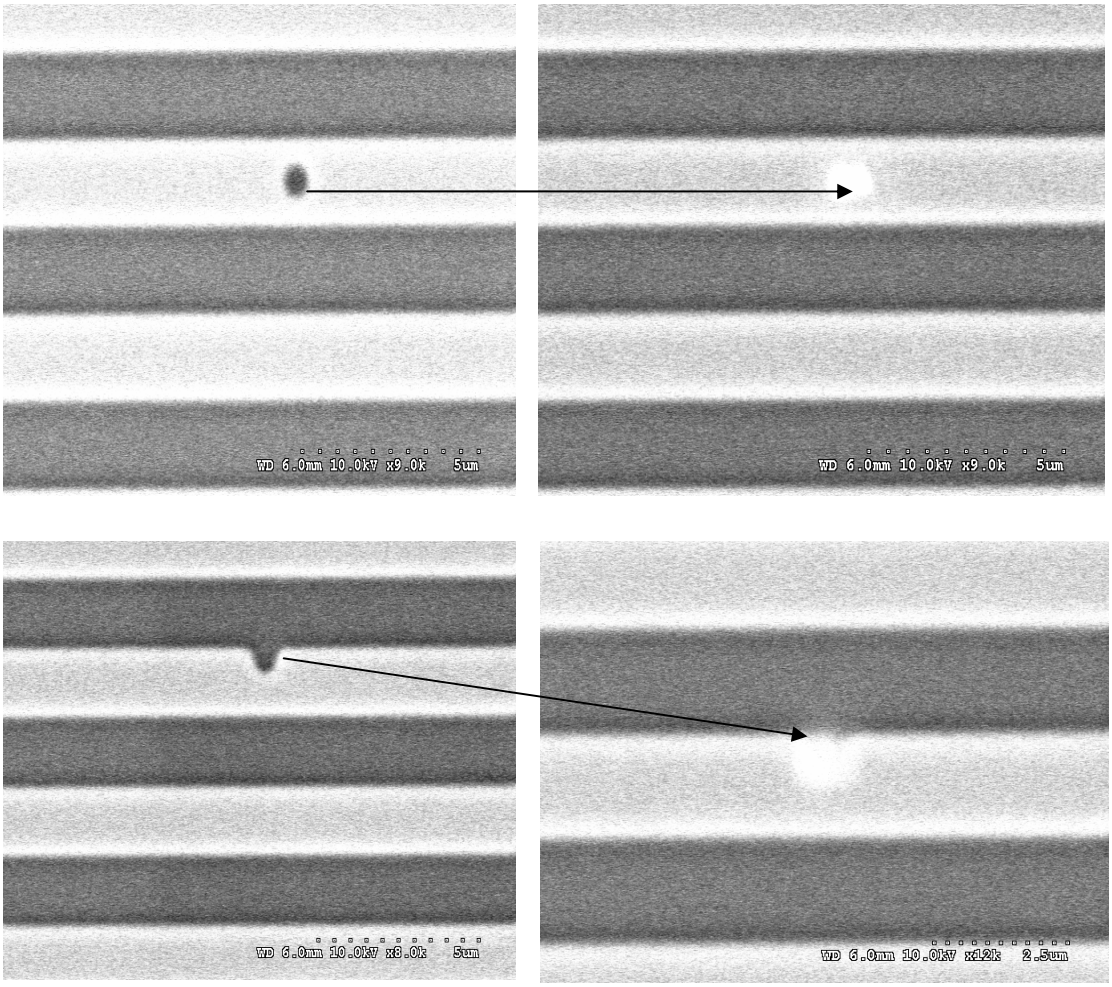


Figure 6.3: Clear defect repair of TaBN//Mo-Si ML/Si EUV mask.

Si on Si substrate) mask was attempted. This repair was done in high vacuum mode with a beam energy of 10Kev, a beam current of 2.05nA, magnification of 12000 for 10 second of deposition for the spot and 5 minutes for the edge with box mode in “TV 1” (TV=0.225s/1 line scan) scan. This repair also resulted in a blurred outline for the repaired areas. For the EUV multi-layer masks, the consistency of the thickness of repaired material is critical for maintaining the same reflectivity of the beam source. If uniformity is not achieved then the result will be a printable defect, possibly requiring a final erosion step in order to make the repair acceptable.

Electron beam induced etching was also performed on TaBN (70nm)/ML EUV mask to demonstrate the repair of opaque defects in the absorber layer pattern. White crystalline XeF_2 was used as the precursor for the etching process. 2 KeV beam energy was chosen to minimize the electron interaction volume not to affect the ML layer and to get slower etch process.

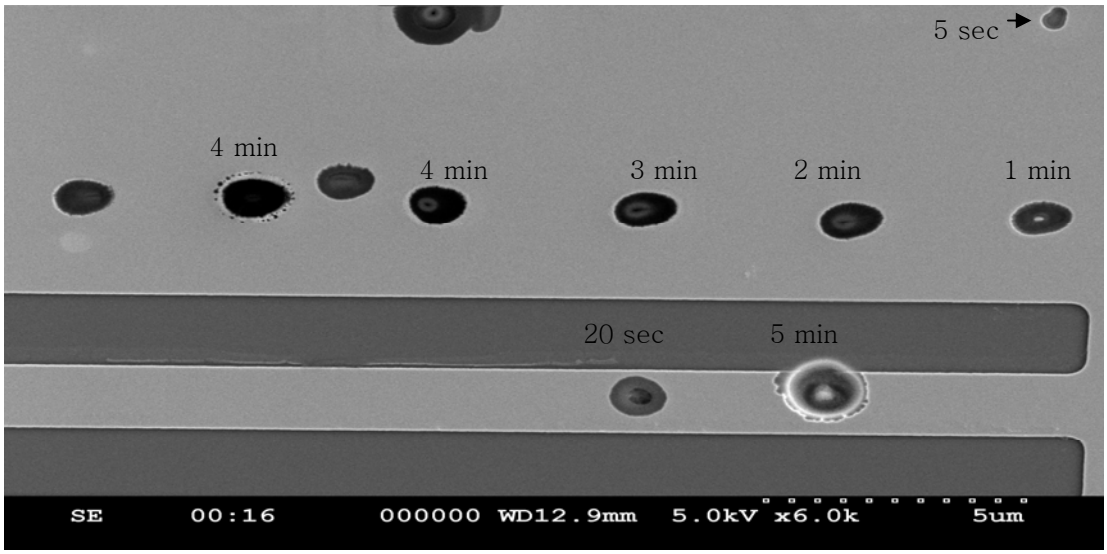
The energy dependence of etch mechanism is not clear and the data presented here differs from the studies of others. The etch rate increases with beam energy was reported by Wang et al. [102] and Fujioka et al. reported oppositely [103]. 1 KeV measurement have been done by Boegli et al. [104], Liang et al. [105], and Edinger et al. [106]. The

use of low beam energy such as 1 KeV protects the multilayers of the mask from the deeper etching caused by higher beam energy and allows finer edge resolution.

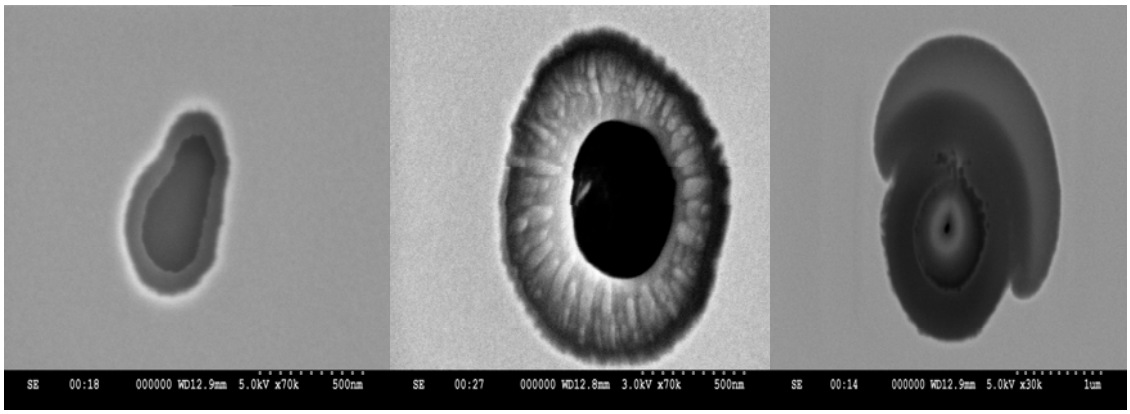
Because it was difficult to get a small probe size when using our Hitachi 3500N VP-SEM at 1 KeV beam energy, 2 KeV was used as a substitute and 12 pA of beam current was employed to etch the TaN absorber layer of EUV mask with 0.2 Pa pressure and a varying spot exposure time with one spot for 5 seconds and 1 minute to 5 minutes as seen in figure 6.4.

It can be seen from the figure 6.4 (b), where the beam exposure time was only 5 seconds, that not only the absorber layer, but also the SiO_2 buffer layer, were completely removed. In practice it is difficult to know that whether or not the reflective multilayers have been removed or attacked. A 2 minute etch in box scan mode (1μm x 1μm) resulted in an etched area circular in shape. This is clearly caused by the SE and BSE emitted from the surface across the width of the interaction volume about the point of incident. Using low beam energy as (1 KeV) for repair improves the shape by reducing the interaction volume but we were forced to used 2 KeV for the clarity of image.

An application of the “Win Casino” Monte Carlo simulation [101] confirms (figure 6.5) that the width and depth of interaction volume at 2KeV beam energy is only about 25nm.



(a)



(b) (c) (d)

Figure 6.4 : Etching of TaN absorber layer with (beam energy 2 KeV, beam current 0.02 nA in 0.2 Pa pressure) (a) different times (b) 5 seconds (c) 20 seconds and (d) box mode with 2minutes.

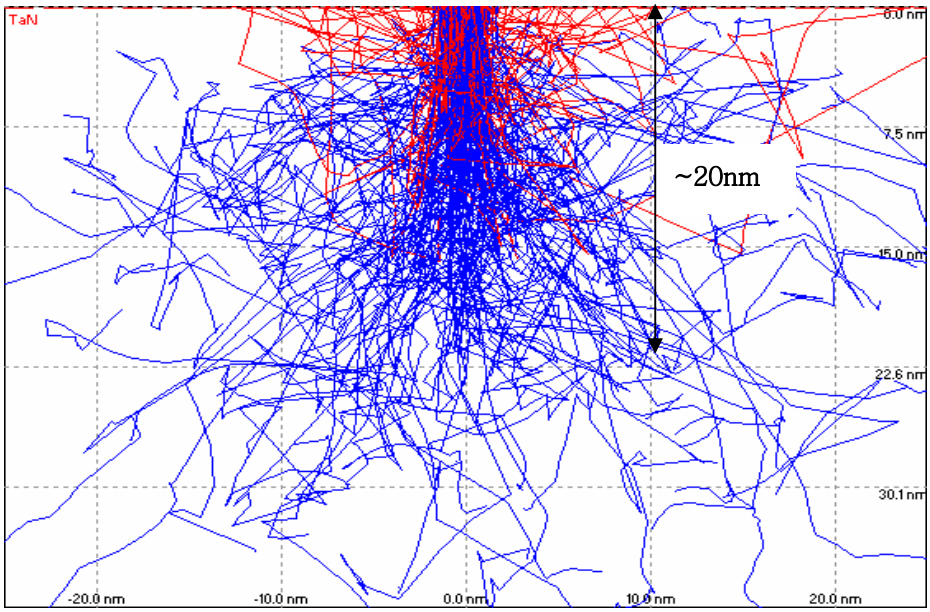


Figure 6.5: Simulated interaction volume with 2KeV beam energy in TaN absorber layer on EUV mask blank by “Win Casino”. [101]

The optimum choice of etching time will not penetrate the oxide buffer layer and will protect the Mo/Si multilayer from etching when repairing opaque defects.

To control the procedure mere affectively the etch rate of the TaN absorber material under electron beam erosion was determined experimentally for suitable set of beam conditions (2 KeV, 53pA current) (figure 6.4).

A rate of ~17nm/min was determined for the conditions, we can estimate that etching process will not attack the 50nm deep SiO_2 buffer layer for the chosen exposure time. For the experiment at 1 KeV beam energy, the etch selectivity of TaN vs SiO_2 is 20:1 [105] and this seems adequate to protect the ML when using 2 KeV electrons. The shift of the etched area about 200nm to the left visible in the image (figure 6.6) may have been caused by instability of electron optics in our SEM.

6.2.1 Repair of Binary Mask Substrate

The charging of the mask substrate is an important problem to overcome during the repair of chrome on quartz binary masks because charging results in a deflection of the beam so distorting the deposition shape, the size or position of the pattern, or sometimes even physically damaging the original pattern. For this reason, experiments to reduce

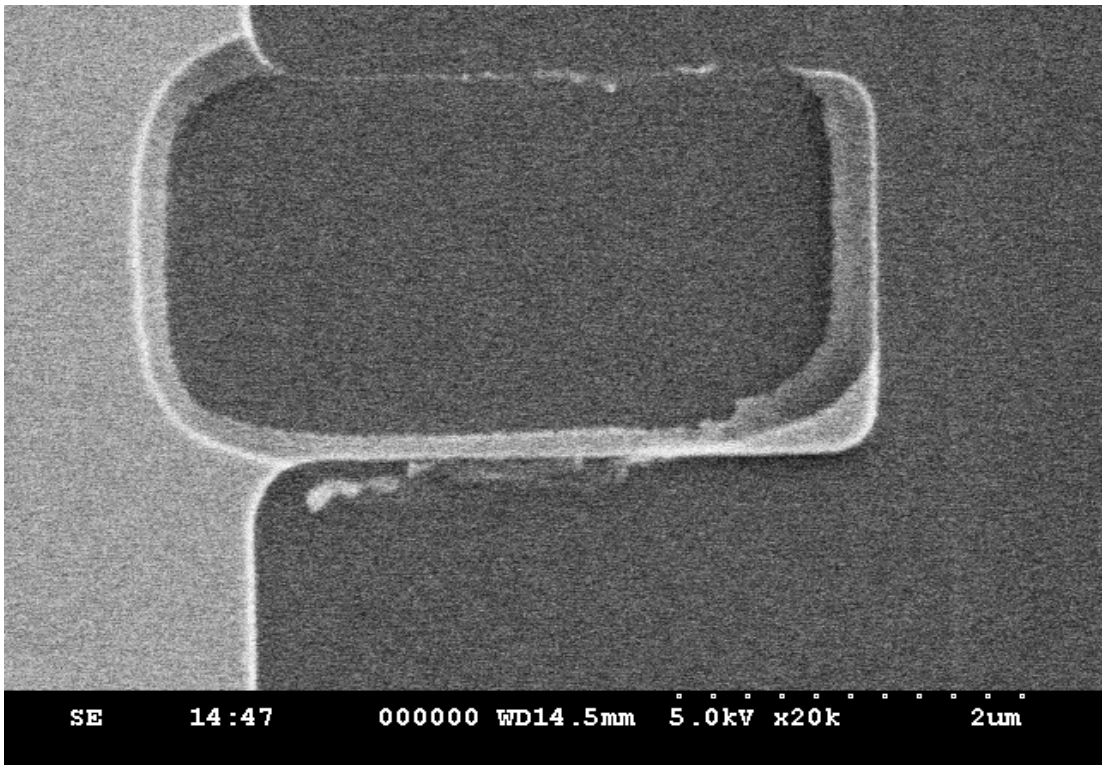
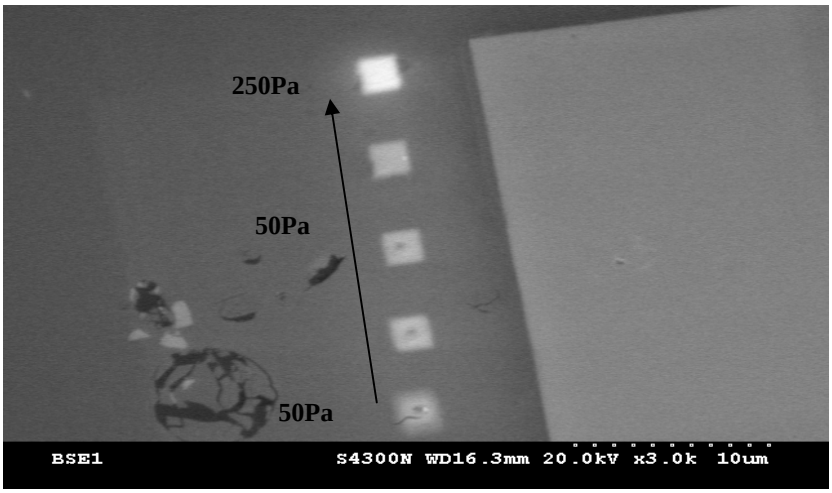
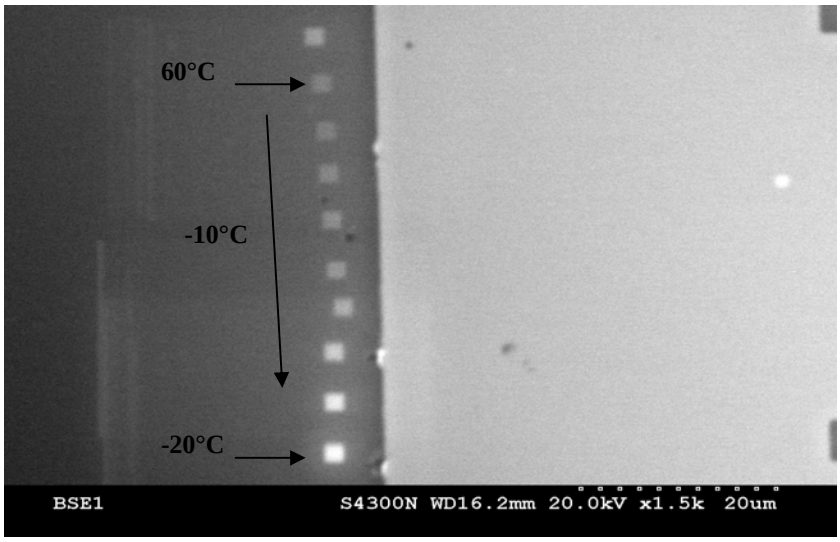


Figure 6.6: Etching with 0.2 Pa ambient pressure using XeF_2 with 2KeV beam energy, 53 pA of beam current for 4 minutes of box mode.

charging were performed by changing the pressure of the chamber when operating in the variable pressure mode of the SEM. When SE from the sample travel through the gaseous environment, collisions occur between an electron and a gas molecule which result in the ionization of the gas molecules and the formation of an ionization cascade. The positively charged gas ions are attracted to the negatively charged specimen and so compensate the effect of the potential that has been acquired. Experiments were done at 20KeV beam energy using 5 minutes exposure time, 4000x magnification, with TV2 (TV=0.225s/1 line scan) scan mode, and changing the pressure from 50 Pa to 250 Pa in increment of 50 Pa, 2μm x 2μm square depositions were made as shown in figure 6.7 (a). As the pressure is increased from 50 Pa two changes are evident. The thickness of the deposit, as judged from the image brightness falls steadily. Since an increase in gas pressure leads to a fall in the severity of surface charging, this indicates that negative surface potential enhances the deposition rate possibly by increasing the SE yield. At the same time the edge definition of the pattern initially improves – suggesting that the reduction in charging improves beam stability – but then degrades as beam scattering becomes significant. And temperature affect of the deposition were tested (as shown in figure 6.7 (b)) changing from -20°C to 60°C. It showed the deposition is better in low



(a)



(b)

Figure 6.7: Deposition of tungsten on quartz. (a) with variation of pressure (b) with variation of temperature.

temperature due to the longer resident time of the gas molecules on the surface of the substrate by looking the brightness of the deposits.

CHAPTER 7

CONCLUSION

The objective of this research was to develop and investigate the properties of electron beam induced deposition (EBID) with the ultimate aim of repairing advanced lithography masks. A gas injection system facilitates deposition in a commercial SEM was constructed and it was confirmed that a commercial SEM could be employed for EBID of metal on a substrate. Parameters such as beam energy, beam current, temperature, pressure and scan rate which can affect the growth of metal have been studied, and the application of the technique to mask repair has been demonstrated.

The studies performed show that controlling the environment to ensure the proper shape, size, and thickness of objects fabricated by EBID is not an easy task. It is related to so many factors such as the gas injection flow rate, the geometry of the injection system, the properties of the precursor gas, the target materials, and to the interaction mechanisms between the electrons and solid. SEM chamber conditions and the substrate temperature also exert a significant effect. Therefore controlling deposition on the nanometer scale to ensure the desired shapes and sizes requires well designed equipment and precisely

calculated conditions.

The study performed here on the repair of masks showed that there are many additional factors, depending on the type of mask, which must also be considered. For chrome on quartz binary masks the effect of charging is a severe limitation because the electric field around the charged area affects the growth of material and so can prevent an effective repair. For the repair of phase shift masks, the thickness of the repaired site has to exactly match that of the original pattern in order to produce the same phase shift of the light source.

To achieve successful mask repair it is therefore necessary to have an understanding of how the precursor gas pressure reduces the charging effect from the electron beam and to acquire more sensitive control of the electron beam time during the raster scan of the area to ensure the proper electron dose for the repair. In future work on using of EBID fabrication for mask repair, it will be important to monitor the hardness and adhesion properties of the deposit in order to optimize the life time of the repaired masks. A variety of types of repair techniques will need to be developed for different types of masks based on their properties.

The studies described in this thesis were focused on the basic techniques needed for

repairing masks using EBID but further studies are needed to achieve better spatial control of the deposit or to provide better predictions of the deposition process using EDID. The future development of precise, and predictable, repair strategies will require a full understanding of the role of electrons (PE, SE, and BSE) and their contribution to the growth mechanism.

REFERENCES

1. Moore, G.E., *Progress in Digital Integrated Electronics.* IEEE International Devices, 1975: p. 11-13.
2. Chang, T.H.P., *Proximity effect in electron beam lithography,.* J. Vac. Sci. Technol., 1975. **12**: p. 1271-1275.
3. D. F. Kyser and N.S. Viswanathan, *Monte Carlo simulation of spatially distributed beams in electron-beam lithography,.* J. Vac. Sci. Technol., 1975. **12(6)**: p. 1305-1308.
4. Yongqi Fu and B.K.A. Ngoi, *Investigation of direct milling of micro-optical elements with continuous relief on substrate by focused ion beam technology.* Opt. Eng., 2000. **39(11)**: p. 3008-3013.
5. T. Liang, et al., *Progress in extreme ultraviolet mask repair using a focused ion beam.* j. Vac. Sci. Technol. B, 2000. **18**(6): p. 3216-3220.
6. Watson, J.H.L., *An Effect of Electron Bombardment upon Carbon Black.* Appl. Phys, 1947. **18**: p. 153.
7. Ennos, A.E., Brit. J. App. Phys., 1953. **4**: p. 101.
8. Stewart, R.L., *Insulating films formed under electron and ion bombardment.* Phys. Rev., 1934. **45**: p. 488.
9. Hiller, J., J. Appl. Phys, 1948. **19**: p. 227.
10. Poole, K.M., Proc. Phys. Soc. London, 1953. **B66**: p. 542.
11. Broer. A.N. and Molzen. W, *Electron-beam formation of 80 A metal structures.* Appl. Phys. Lett., 1976. **29**: p. 596.
12. R. M. Silver, E. E. Ehrichs, and R.A.d. Lozanne, *Direct writing of submicron metallic feature with a scanning tunneling microscope.* Appl. Phys. Lett., 1987. **51(4)**: p. 247.
13. Weber, M., Rudolph, M., Kretz, J., and Koops, H., *Electron-beam induced-deposition for fabrication of vacuum field emitter devices.* J. Vac. Sci. Technol., 1995. **B13**: p. 461.
14. J. Kretz, M.R., M. Weber, and H.W.P. Koops, *Three-dimensional structurization by additive lithography, analysis of deposits using TEM and EDX, and application to field-emitter tip.* Microelectronic Engineering, 1994. **23**: p. 477-481.
15. Mayer, R.R.K.a.T.M., Appl. Phys. Lett., 1987: p. 962-964.
16. J. Melngailis, et al. in *Proc. Int. Symp. Progress Physics and Mod. in Semiconductor Technol.* 1990.

17. Kohlmann-von Platen, K., and Chlebek, J., *Resolution limits in electron-beam induced tungsten deposition.* J. Vac. Sci. Technol., 1993. **B11**: p. 2219.
18. Komuro, M., and Hiroshima, H., *Fabrication and properties of dot array using electron-beam-induced deposition.* Microelectronic Engineering, 1997. **35**: p. 273.
19. Komuro, M., and Hiroshima, H., *Lateral junction produced by electron-beam-induced-deposition.* J. Vac. Sci. Technol., 1997. **B15**: p. 2809.
20. Schiffmann, K., *Investigation of fabrication parameters for the electron beam induced deposition of contamination tips used in atomic forced microscopy.* Nanotechnology, 1993. **4**: p. 163.
21. Sanche, L., *Low energy electron scattering from molecules on surface.* J. Phys B, 1990. **23**: p. 1597.
22. Sanche, L., *Investigation of ultra fast events in radiation chemistry with low energy electrons.* Radiat. Phys. Chem., 1989. **34**: p. 15.
23. Silvis-Cividjian, N., *Electron Beam Induced Nanometer Scale Deposition*. 2002.
24. P. Blauner and J. Ro, *FIB of submicron gold structures.* . J. Vac. Sci. Technol., 1989. **B7**: p. 609.
25. Dubner, A., and Shedd, G., *Ion beam induced deposition of gold by focused and broad-beam sources.* J. Vac. Sci. Technol. B, 1987. **5**: p. 1434.
26. Folch, A., and Servat, J., *High-vacuum versus "environmental" electron beam deposition.* J. Vac. Sci. Technol., 1996. **B14**: p. 2609.
27. Folch, A., and Tejada, J., *Electron beam deposition of gold nanostructures in a reactive environment.* Applied Physics Letters, 1995. **66**: p. 2080.
28. Shed, G., and Lezec, H., *Focused ion beam induced deposition of gold.* Appl. Phys. Lett., 1986. **49**: p. 23.
29. Bruckl, H., Kretz, J., Koops, H., and Reiss, G.. *Low energy electron beam-deposition of metalorganic precursor with a STM at ambient atmosphere.* J. Vac. Sci. Technol. B, 1999. **17**: p. 1350.
30. Floreani, F., Koops, H., and Elsasser, W., *Operation of high power field emmiters fabricated with electron beam deposition and concept of a miniaturized free electron laser.* Microelectronic Engineering, 2001. **57-58**: p. 1009.
31. Koops, H., Weiel, R., and Kern, P., *High-resolution electron-beam induced deposition.* J. Vac. Sci. Technol., 1988. **B6**: p. 447.
32. Lee, K., and Hatzakis, M., *Direct electron-beam patterning for nanolithography.* J. Vac. Sci. Technol., 1989. **B7**: p. 1941.
33. Schoessler, C., Kaya, A., Kretz, J., Weber, M., and Koops, H., *Electrical and field*

emission properties of nanocrystalline materials fabricated by EBID. Microelectronic Engineering, 1996. **30**: p. 471.

34. Utke, I., and Hoffman, P., *Focused electron beam induced deposition of gold.* J. Vac. Sci. Technol. B, 2000. **18**: p. 3168.
35. Gamo, K., Takakura, N., Samoto, N., Shimizu, R., and Namba, S., *Ion beam assisted deposition of metal organic films using focused ion beams.* J. J. Appl. Phys., 1984. **23**: p. L293.
36. Ishibashi, A., Funato, K., and Mori, Y., *Electron-beam-induced resist and aluminium formation.* J. Vac. Sci. Technol. B, 1991. **9**: p. 169.
37. Ochiai, Y., and Fujita., *Electron induced beam deposition of copper compound with low resistivity.* J. Vac. Sci. Technol. B, 1996. **14**: p. 933.
38. Matsui, S., and Mori, K., *New selective deposition technology by electron beam induced surface reaction.* J. Vac. Sci. Technol., 1986. **B4**: p. 299.
39. Kunz, R., Allen, T., and Mayer, T., *Selective area deposition of metals using low-energy electron beams.* J. Vac. Sci. Technol. B, 1987. **5**: p. 1427.
40. Welipitya, D., *Ultraviolet and electron radiation induced fragmentation of adsorbed ferrocene.* J. Appl. Phys, 1996. **79**: p. 8730.
41. M. Weber, H.W.P.K., M. Rudolph, J. Kretz, and G. Schmidt, *New compound quantum dot materials produced by electron-beam induced deposition.* J. Vac. Sci. Technol. B, 1995. **13**: p. 1364.
42. Scheuer, V., and Koops, H., *Electron beam decomposition of carbonyls on silicon.* Microelectronic Engineering, 1986. **5**: p. 423.
43. Rubel, S., Trochet, M., Ehrichs, E., Smith, W., and De Lozanne, A., *Nanofabrication and rapid imaging with a scanning tunneling microscope.* J. Vac. Sci. Technol. B, 1994. **12**: p. 1894.
44. Wang, X., Rubel, S., Purbach, U., and De Lozanne, A., *Resistance of Ni nanowires fabricated by STM-CVD.* Prceedings SPIE, 1997(3009): p. 2.
45. Saulys, D., Ermakov, A., and Garfunkel, E., *Electron beam induced patterned deposition of allycyclopentadyenil palladium using STM.* Appl. Phys, 1994. **76**: p. 7639.
46. Kislov, N., Khodos, I., and Ivanov, E., *Electron-beam-induced fabrication of metal containing nanostructures.* Scanning, 1996. **18**: p. 115.
47. Szkutnik, D., Piednoir, A., Ronda, A., Marchi, F., Tonneau, D., Dallaporta, H., and Hanbuken, M., *Scanning probes as lithography tool for nanostructures.* Applied surface science, 2000. **164**: p. 169.

48. Marchi, F., *Nanometer scale patterning by scanning tunnelling microscope assisted chemical vapor deposition.* Microelectronic Engineering, 2000. **50**: p. 59-65.
49. Koops, H., Kaya, A., and Weber, M., *Fabrication and characterization of platinum nanocrystal material grown by EBID.* J. Vac. Sci. Technol., 1995. **B13**: p. 2400.
50. Hubner, U., and Plontke, R., *On-line nanolithography using electron beam induced vapor deposition by TEM.* Microelectronic Engineering, 2001. **57-58**: p. 953.
51. Takai, M., and Kishimoto, T., *Fabrication of field emitter array using focused ion and electron beam induced deposition.* Microelectronic Engineering, 1998. **41/42**: p. 453.
52. Lipp, S., Frey, L., and Lehrer, A., *A comparison of focused ion beam and electron beam induced deposition processes.* Microelectronics and reliability, 1996. **36**: p. 1779.
53. Tao, T., Ro, S., and Melngailis, J., *Focused ion beam induced deposition of platinum.* J. Vac. Sci. Technol. B, 1990. **8**: p. 1826.
54. Morimoto, H., and Kishimoto, T., *Electron beam induced deposition of Ptfor field emitter arrays.* Japanese Journal of Applied Physics, 1996. **35**: p. 6623.
55. Puretz, J., and Swanson, L., *Focused ion beam deposition of Pt containing films.* J. Vac. Sci. Technol. B, 1995. **10**: p. 2695.
56. Komano, H., Ogawa, Y., and Takigawa, *Silicon oxide formation by FIB assisted deposition.* Japanese Journal of Applied Physics, 1989. **28**: p. 2372.
57. Kunz, R., Mayer, T., *Surface chemical reactions stimulated by low energy electron bombardment.* Mat. Res. Soc. Symp. Proc Materials Research Society, 1987. **75**.
58. Ichihashi, T., Matsui, S., *In situ observation on electron beam induced chemical vapor deposition by TEM.* J. Vac. Sci. Technol., 1988. **B6**: p. 1869.
59. Matsui, S., and Ichihashi, T., *Electron beam induced selective etching and deposition technology.* J. Vac. Sci. Technol., 1989. **B7**: p. 1182.
60. Stewart, D., Stern, L., and Morgan, J. *Focused ion beam induced deposition of metal for microcircuit modification*. in *SPIE proceedings on Electron Beam, X-ray and ion beam technology*. 1989.
61. stewart, D., and Morgan, J., *Focused ion beam induced deposition of tungsten on vertical sidewalls.* J. Vac. Sci. Technol. B, 1991. **9(5)**.

62. Petzold, H., *Ion induced deposition for X-ray mask repair: rate optimization using time-dep. model.* J. Vac. Sci. Technol., 1991. **B9**: p. 2664.
63. Sawaragi, H., and Mimura, R., *Perfomance of a combined focused ion and electron beam system.* J. Vac. Sci. Technol. B, 1990. **8**: p. 1848.
64. Hoyle, P., Cleaver, J., and Ahmed., *Electron beam induced deposition from W(CO)6 at 2 to 20 Kev and its applications.* J. Vac. Sci. Technol., 1996. **B14**: p. 92.
65. McCord, M., and Kern, D., *Direct deposition of 10nm metallic features with the STM.* J. Vac. Sci. Technol., 1988. **B6**: p. 1877.
66. Hiroshima, H., and Komuro, M., *High growth rate for slow scanning in electron beam induced-deposition.* J.J. Appl. Phys., 1997. **36**: p. 7686.
67. Davies, S., and Khamsehpour., *FIB machining and deposition for nanofabrication.* Vacuum, 1996. **47**: p. 455.
68. Harriot, L., and Vasile, M., *FIB deposition of opaque carbon film.* J. Vac. Sci. Technol., 1988. **B6**: p. 18.
69. Bezryadin, A., and Dekker, C., *Nanofabrication of electrodes with sub-5nm spacing for transport experiments on single molecules and metal clusters.* J. Vac. Sci. Technol., 1997. **B15**: p. 793.
70. Yasaka, A., *Experimental study on the influence of liquid metal ion source energy distribution on FIB induced deposition.* J. Vac. Sci. Technol. B, 1991. **9(5)**.
71. Koshikawa, T., and Shimizu, R., *A Monte Carlo calculation of low energy secondary electron emission from metals.* Journal of Physics, 1974. **D7**: p. 1303.
72. Joy, D., *Monte Carlo Modeling for electron microscopy and microanalysis*. 1994, New York: Oxford university press.
73. Ding, Z., and Shimizu, R., *Monte Carlo modelling of electron interaction with solids including cascade secondary electron production.* Scanning, 1996. **18**: p. 92.
74. Reimer, L., and Lodding, B., *Theory of secondary electron emission ii.* Scanning, 1984. **6**: p. 29.
75. Mutara, K., *Monte Carlo simulation of fast secondary electron production in electron beam resist.* J. Appl. Phys, 1981. **52**: p. 4396.
76. Kotera, M., *A Monte Carlo simulation of primary and secondary electron trajectories in a specimen.* J. Appl. Phys, 1989. **65**: p. 3991.
77. Hovington, P., Droun, D., and Gauvin, R., *CASINO: A new Monte Carlo code in C language for electron beam interaction-I: description of the program.* Scanning,

1997. **19**: p. 1-14.
78. Hart, R., Kassner, T., and Maurin, J., *The contamination of surface during high-energy electron irradiation.* Philosophical Magazine, 1969: p. 453.
79. Muller, K., *Elektronen mikroschreiber mit geschwindigkeitsgesteuerter strahlfurung.* Optik, 1971. **33**: p. 296.
80. Wall, J., *Contamination in the STEM at ultra high vacuum.* Scanning Electron Microscopy, 1980: p. 99.
81. Amman, M., Sleight, J., Lombardi, D., Welser, R., and Deshpande, M., *Atomic forced microscopey study of electron beam written contamination structure.* J. Vac. Sci. Technol., 1996. **B14**: p. 54.
82. Reimer, L., *Contribution to the contamination problem in transmission electron microscopy.* Ultramicroscopy, 1978. **3**: p. 169.
83. Kohlmann, K., Thiemann, M., and Brunger, W., *E-beam induced x-ray mask repair with optimized gas nozzle geometry.* Microelectronic Engineering, 1991. **13**: p. 279.
84. Hoyle, P., Cleaver, J., and Ahmed., *Ultralow-energy focused electron beam induced deposition.* Appl. Phys. Lett., 1994. **64**: p. 1448.
85. Komuro, M., Hiroshima, H., and Takechi, A., *Miniature tunnel junction by electron-beam-induced deposition.* Nanotechnology, 1998. **9**: p. 104.
86. Hubner, B., and Koops, H., *Tips for scanning tunneling microscopy produced by EBID.* Ultramicroscopy, 1992. **42-44**: p. 1519.
87. Uesugi, K., and Yao, T., *Nanometer scale fabrication on graphite surfaces by scanning tunneling microscopy.* Ultramicroscopy, 1992. **42-44**: p. 1443.
88. Pai, W., Zhang, J., Wendelken, J., and Warmack, R., *Magnetic nanostructures fabricated by scanning tunneling microscope-assisted chemical vapor deposition.* J. Vac. Sci. Technol., 1997. **B15**: p. 785.
89. Ivor Brodie and J.J. Muray, *The Physics of Micro/Nano-Fabrication*. 1993: Plenum Publishing Corporation.
90. Hall, J., Hansma, P., and Parikh, M., *Electron beam damage of chemisorbed surface species: a tunnelling spectroscopy study.* Surface science, 1977. **65**: p. 552.
91. Joy, D., *The theory and practice of high resolution scanning electron microscopy.* Ultramicroscopy, 1991. **37**: p. 216.
92. Ding, Z., and Tang, X., *Monte Carlo study of secondary electron emission.* J. Appl. Phys, 2001. **89**: p. 718.

93. N. silvis-Cividjian, C.W.H., and P. Kruit and M.A.J.v.d.S.a.H.B. Groen, *Direct fabrication of nanowires in an electron microscope.* Appl. Phys. Lett., 2003. **82**: p. 3514.
94. Shimizu, R., and Murata, K., *Monte Carlo calculations of electron sample interactions in the scanning electron microscope.* J. Appl. Phys, 1971. **42**: p. 387.
95. Joseph I. Goldstein, D.E., Newbury, Patrick Echlin, David C. Joy, A. D. Romig, Jr., Charles E. Lyman, Charles Fiori, and Eric Lifshin, *Scanning Electron Microscopy and X-ray Microanalysis*. second edition ed. 1992.
96. H.W.P. Koops, C.S., A. Kaya and M. Weber, *Conductive dots, wire, and supertips for field electron emitters produced by electron-beam induced deposition on samples having increased temperature.* J. Vac. Sci. Technol., 1996. **B 14(6)**: p. 4105.
97. Hudson, J.B., *Surface Science: An Introduction*. 1992: Butterworth-Heinemann.
98. S. J. Randolph, J.D.F., and P. D. Rack, *Effects of heat generation during electron-beam-induced deposition on nanostructures.* J. Appl. Phys, 2005. **97**(124312).
99. Kohlmann-von Platen, K., and Buchmann, L., *Electron beam induced tungsten deposition: growth rate enhancement and applications.* J. Vac. Sci. Technol., 1992. **B10**: p. 2690-2694.
100. Sawaragi, H., and Mimura, R., *Performance of a combined focused ion and electron beam system.* J. Vac. Sci. Technol., 1990. **B8**: p. 1848.
101. Dominique Drouin, et al., *Monte Carlo Simulation of electron trajectory in solids*. 2000: University de Sherbrooke, Sherbrooke, Quebec, CANADA.
102. Jianhua Wang, et al., *Etching charateristics of chromium thin films by an electron beam induced surface reaction.* Semicond. Sci. Technol., 2003. **18**: p. 199.
103. H. Fujioka, et al., *Measurements of the energy dependence of electron beam assisted etching of, and deposition on, silica.* J. Phys D: Appl. Phys., 1990. **23**: p. 266-268.
104. V. Boegli, e.a., *Electron-beam induced processes and their applicability to mask repair.* Proc. SPIE, 2002. **4889**: p. 283.
105. T. Liang and A. Stiver, *Damage-free mask repair using electron beam induced chemical reactions.* Prceedings of SPIE, 2002. **4688**: p. 375.
106. K. Edinger, et al., *Application of electron-beam induced processes to mask repair.* Prceedings of SPIE, 2003. **5130**: p. 383.

VITA

Young Ryong Choi was born in Jinju, Korea on January 31, 1970. He graduated from Dae-A high school in Jinju, Korea in 1989, in the same year he entered the Physics department at the Kyeng Sang National University, in Jinju, from which he received his bachelor degree in 1996. He served Korean army from 1990 to 1992 in the Construction Division.

In summer of 1998 he was admitted to the Ph.D. Program in Physics Department at the University of Tennessee, Knoxville. He worked for Hi-Tc super conductivity material with Dr. J. Thompson in 2000 and 2001. He joined Dr. David C. Joy's research team in 2002. Since then he has been involving in the field of the Electron Beam Induced Deposition (EBID) research for mask repair using scanning electron microscope for semiconductor industry. He will be awarded the doctoral degree in Materials Science and Engineering in December 2006.